Experimental study of the pygmy dipole resonance in the $(\mathrm{p},\mathrm{p}'\gamma)$ reaction on $^{124}\mathrm{Sn}$ and its evolution in the Sn isotopic chain

by

Maria Markova

Thesis
for the degree of
Master of Science

Faculty of Mathematics and Natural Sciences
University of Oslo

March 2020

Abstract

The present thesis makes a specific focus on the experimental study of the pygmy dipole resonance (PDR) in ^{124}Sn and its evolution with increasing number of neutrons for the $^{116-119,121,122}$Sn and ^{124}Sn isotopes studied at the Oslo Cyclotron Laboratory. Proton-γ coincidences data were measured in the (p,p$'\gamma$) reaction exploiting the primary beam of 16 MeV protons. The Oslo method was applied in order to extract the average characteristics of ^{124}Sn, such as the γ-ray strength function and the level density. The external data from neutron resonance experiments were utilized for collecting the systematics on the level density and the average radiative width at the neutron separation energy. These systematics were subsequently used to constrain the slope and normalization of both extracted characteristics.

Several approaches to the normalization procedure were tested, and all the γ-ray strengths extracted were found to be in good agreement within the estimated systematic and statistical uncertainties with the external data, obtained with different experimental techniques. A peak-like structure was observed in the strength at ≈ 6.5 MeV, and this was found to be in agreement with other experimental data. The total dipole response of a nucleus was reconstructed from $E_\gamma \approx 1.6$ MeV up to ≈ 18 MeV in order to extract the bulk characteristics of the PDR mode, such as the energy centroid and integrated strength. Moreover, the present work contributes with the fraction of the Thomas-Reiche-Kuhn sum rule (TRK) exhausted by the PDR in the ^{124}Sn isotope to the systematics, previously obtained at the Oslo Cyclotron Laboratory for the lighter tin isotopes. The fraction of the TRK sum rule, extracted for the γ-ray strength function obtained with the approach similar to that used for the lighter Sn isotopes, points at an almost constant fraction of the total dipole strength, attributed to the PDR. Furthermore, the alternative normalization of the γ-ray strength function, proposed in the present work, results in the largest fraction ($\approx 2\%$) for ^{124}Sn among all Sn isotopes studied. In addition, the distinguished components of the PDR were found to be shifted towards lower γ-energies as compared to the lighter Sn isotopes.

In addition, the qualitative test of the generalized Brink-Axel hypothesis was carried out by studying the extracted strengths as functions of various initial and final excitation energies. The strength was found to be independent of the initial excitation energy with the correction for observed Porter-Thomas fluctuations. The γ-ray strength functions feeding the ground and the first excited states were found to deviate strongly from an average strength, especially for the low γ-energies. Such deviation was assumed to stem from numerous reasons, and one of the reasons implies that the Brink-Axel hypothesis does not hold for these states.

To my infinitely supporting family.

Acknowledgements

While working on this thesis and studying at the University of Oslo I have received an exceptional amount of support from incredible, inspiring and encouraging members of the Oslo group who became my second family.

First of all, I would love to thank my supervisers Ann-Cecilie Larsen and Frank Leonel Bello Garrote. Thank you both for an exceptional encouragement and support I have been receiving every day at the university. You have showed me what the experimental nuclear physics could be like, that it is not a lonely solo work in an office corner, as it used to be for me before. It is rather a harmonious work of dedicated people, sharing the same idea of looking far beyond our current knowledge, inspiring each other for daring ideas and actions. Ann-Cecilie, your have always supported me with your professional knowledge and infinite optimism, you encouraged my eagerness to learn more, to dare to explore the new fields I used to be a complete stranger in. Even though this thesis was written in a huge rush, I promise you to proceed working unless we extract everything we could extract from this fantastic pygmy story. Frank, I would love to thank you for tolerating my numerous questions on how the things work. I hope that at some point I would finally understand this and share my knowledge with others.

Secondly, I would love to thank the whole Oslo group for every single day I spent with you. You let me become a part of you, and everything I know about the experiment is owing to what you have shared with me. Thanks to Magne Sveen Guttormsen for every conversation about the mysteries of the Oslo method and being the one of the creators of this elegant methodology. Sunniva Siem, thank you for expanding my professional networks, all the conferences and summer schools you allowed me to be a part of. You have showed me that nuclear physics is a collaboration of fantastic devoted people around the world. Especially, I would love to thank Andreas Görgen for being the best lecturer I have ever had. I wish I could become such a dedicated scientist as you.

I am infinitely grateful to my parents for everything you have done for me: for reading Astrid Lindgren and Tove Jansson in my childhood, for showing me the whole world, for those summer bike trips, sitting under our three birches and talking about the life, for that trip to Norway in 2014, which has completely changed my life. And, finally, for insistent pushing me away, to the places where I could find happiness.

I tillegg vil jeg takke for alle de fine vennskapene jeg har fått her i Norge. Dere har vært en enorm støtte for meg i løpet av disse to årene. Jeg kan med sikkerhet si at dere er de beste vennene jeg noen gang har hatt og som jeg alltid har drømt om. Jeg vill tanke dere for deres forståelse, for at dere har gjort det slik at jeg ble akseptert i Norge så raskt og klarte å finne et nytt hjem her i landet. Jeg kommer aldri til å glemme alle timer og dager vi har brukt sammen, alle nye opplevelser, ideer og tanker dere har delt med meg. Dere har forandret min levemåte og hjulpet meg til å bli den personen jeg alltid har hatt lyst til å være. Dere kan ikke forestille dere hvor mye dere betyr for meg.

Til stutt, Vala, jeg husker at jeg har lovet deg at vi skal lage et dataspill sammen en gang og det løffet har jeg tenkt til å holde.

Maria L. Markova

March 2, 2020

Contents

Chapter 1

Introduction: resonances in atomic nuclei

An atomic nucleus is a complex composite system of bound constituents, namely protons and neutrons, and its properties and behavior are still an infinite source of theoretical and experimental questions and problems to be solved. Despite a rapid development of experimental techniques and elaborate theories, more and more questions on how nuclear constituents interact with each other and which forces underlie this interaction emerge as new facts are revealed. Luckily, this process makes up the stable *Perpetuum Mobile* for the further development of nuclear physics in upcoming years.

One natural way to study such a microscopic system is to subject it to various external perturbations and test how the system would respond. Different perturbation mechanisms tested with advanced experimental techniques enable a thorough study of different properties of an atomic nucleus, *e.g.* its charge and mass distribution, compression modulus, saturation density [1] and neutron skin thickness [2]. Experimentally, such a perturbation can be introduced by means of photon absorption and reemission, particle scattering (proton, neutron, α-particle, electron, *etc.*) or numerous transfer reactions, where a nucleon is being stripped or added to a target nucleus. The corresponding cross-sections, or probabilities, of these processes, observed as a function of energy and momentum transfer, might serve as a bulk representation of all the processes involved at different energies. One could split the whole observed energy range into several regions: a region below particle threshold (or particle separation energy), an intermediate region, and the region above the meson production threshold (≈ 135 MeV). The former would be the core range of study in the present work; it will be studied alongside the intermediate region in order to demonstrate how the reaction channel changes around the binding energy limit. The first region is characterized by an excitation energy insufficient for individual nucleons or nucleonic systems to be knocked out, and, thus, reflects excitations of separate, relatively low-lying nuclear levels, followed by deexcitations via γ-emission. This diapason is also referred to as the region of Nuclear Resonance Fluorescence (NRF). Further increase of the excitation energy would result in so-called photodissociation processes, namely emission of separate nucleons, light systems of bound nucleons (deuteron, α-particle), or even photofission. An appearance of broad maxima in the observed cross-sections makes this region particularly interesting for numerous theoretical and experimental approaches; these maxima, or giant resonances, stem directly from the collective nuclear properties. Their properties could be inferred from systematic studies and theoretical attempts to predict how these resonances are formed. The majority of data concerns the absorption of electric dipole photons, resulting in the appearance of the giant dipole resonance in the observed cross-section. This feature has served as the major touchstone for various theories and the starting point for studies on other resonances. Further up to higher energies, above the meson threshold, it becomes possible to interact with individual nucleons rather than the nucleus as a whole, and nucleon resonances, *e.g.* Δ_{33} around 300 MeV, might be observed in the nuclear response [1]. The latter was found to be quite complex and requiring dedicated, thorough studies in separate energy regions.

The long history of resonances begins in 1937 with the first observation of an enhanced photo-dissociation cross-section, measured for some nuclei by W. Bothe and W. Gentner [3]. An electrostatic 600 keV van de Graaf generator was used to produce photons with energies of 14 and 17 MeV in the ^{7}Li(p,γ) reaction, directed subsequently at a target. The measured cross-section of the photodissociation reaction on a ^{65}Cu target for 17 MeV photons was found to be sufficiently large ($\approx$50 mb), and the following discussion led to the assumption on a resonance origin of the enhancement observed. A year after this experiment, the further discussion and study of resonance structures was noticeably encouraged by N. Bohr, who predicted that the experiments with variable radiation frequency would cast light upon a collective nature of resonance effects [4].

This observation required a further theoretical interpretation, proposed later by A. Migdal in his seminal work in 1944 [5]. In fact, it was the first theoretical prediction of the giant dipole resonance (GDR, or from now on the IVGDR for isovector giant dipole resonance), which was identified as a broad (5-10 MeV) maximum in the γ-absorption cross-section, centered at 14-16 MeV for heavy nuclei and shifted to 20-25 MeV for lighter nuclei. It was also deduced that the energy of this maximum is tightly related to the symmetry energy term in the Bethe-Weizsäcker formula as well as the average kinetic energy of nucleons. Migdal's interpretation of the IVGDR was performed in terms of quantum collective modes of excitations, and this conceptual approach was subsequently shown to be quite successful. It underwent further development and modifications in order to provide the deeper understanding of this resonance phenomenon (see *e.g.* [6]).

Right after the theoretical prediction by Migdal, the IVGDR was directly observed by G. C. Baldwin and G. S. Klaiber in 1946 in photofission cross-sections for several heavy nuclei [7]. This experiment broke new ground in nuclear experiments due to the exploitation of a betatron, recently put into operation and able to produce beams of electrons with energies high enough to perform photofission experiments. In Baldwin's experiment, a beam of bremsstrahlung photons was incident on uranium, thorium, and other heavy element targets, and the subsequent analysis of the photofission reaction yields revealed a prominent maximuma at $\approx$ 16 MeV with $\approx$ 3 MeV full width at half maximum for the photofission cross-sections studied as functions of photon energy. Only one year later, Baldwin and Klaiber confirmed the appearance of resonance structures for lighter nuclei such as ^{12}C and ^{63}Cu (with maxima at $\approx$ 30 and 22 MeV respectively) in (γ,n) reactions with photons of energies up to 100 MeV [8].

The following years were marked by extensive theoretical and experimental attempts to investigate the IVGDR. The contemporary level of understanding of resonances was formed after the appearance of two essentially different approaches. The first approach was elaborated by M. Goldhaber and E. Teller [6], who considered the IVGDR as engendered by the oscillations of incompressible, interpenetrative proton and neutron liquids within a nucleus. On the other hand, it was attempted to apply the shell model for the description of the resonance structures, as it was shown to be successful for the treatment of other nuclear phenomena. This was performed by D. H. Wilkinson, who approached the IVGDR in the mean field framework as a group of dipole excitations from a filled shell to an empty one [9]. Several attempts were carried out in order to combine both the macroscopic and microscopic approaches, but numerous contradictions are still to be considered and resolved. Certain success was achieved after considering the role of the residual interaction, which resulted in various Random Phase Approximation-based calculations for resonances in atomic nuclei across the whole nuclear chart [10].

The resonance phenomenon, discussed above, could be treated as a nuclear response to a time dependent external field, able to affect spacial, spin, and isospin coordinates of nucleons within a nucleus. This field could transfer a certain angular momentum **L**, spin **S**, and isospin **T** to a nucleus it interacts with. In case of the mentioned experiments, the resonance could be interpreted as a response to an electric field with $\mathbf{L} = \mathbf{1}$, or electric dipole field; the spin of a nucleus remains unaffected, while the isospin changes by a unit (if the initial isospin is $T_i = 0$). The different coordinates, or such fundamental properties as the spin S, isospin T, and multipolarity L, affected during the interaction imply that the isovector giant dipole resonance ($\Delta L = 1$, $\Delta S = 0$, $\Delta T = 1$) is not the only resonance to be observed experimentally. All the giant resonances can be classified with respect to the angular momentum, spin, and isospin change.

Initially, the classification was related to multipolarity and parity of an absorbed photon, where parity is defined for electric (EL) and magnetic (ML) types of radiation as following:

$$\begin{aligned} P(EL) &= (-1)^L, \\ P(ML) &= (-1)^{L+1}. \end{aligned} \tag{1.1}$$

Absorption or emission of radiation is, therefore, directly related to the type (defined by L: dipole, octupole, etc) of the system of charges or currents excited within a nucleus.

According to the quantum numbers of spin, isospin, and multipolarity, and their change in the excitation process, one can distinguish two categories of resonances with the fundamental difference hidden in the magnetization of a nucleus, related directly to the spins of nucleons [1]:

1. **Electric resonances**: $\Delta S = 0$. This type of resonance implies no spin change. In other words, the corresponding excitation operator, which acts on the ground state of a target nucleus, does not contain spin-dependent terms.

2. **Magnetic resonances**: $\Delta S = 1$. In the microscopic picture, these resonances are represented by coherent transitions of particles from one shell to another, accompanied by an additional spin-flip.

For the electric resonances one might consider the case of $\Delta S = 0$, $\Delta T = 0$, $\Delta L = 0, 2, ...$ etc, which corresponds to the **electric isoscalar resonances**. Here, it is convenient to introduce such macroscopic terms as proton and neutron components, which are simply the bulk "clouds"of protons and neutrons, considered separately. Therefore, the isoscalar resonances are engendered by a synchronized, or in-phase, motion of the proton and neutron components of a nucleus, governed by a certain multipolarity. $\Delta L = 1$ would correspond to a translational motion of a nucleus and can not be considered as a nuclear excitation. One can also emphasize an electric isoscalar monopole mode, which is realized as periodic expansions and contractions of a nucleus while the nuclear shape remains unchanged. This mode can be also called the breathing mode, and it serves as the main source of information on the compressibility of a nucleus. The $\Delta S = 0$, $\Delta T = 1$, collective excitations ($\Delta L = 0, 1, 2, ...$ *etc.*) are known as the **electric isovector resonances**. In this case the proton and neutron components are oscillating out of phase, and the IVGDR is observed.

Introduction of the spin-flip (or spin change) $\Delta S = 1$ provides us with a new degree of freedom. Such resonances might be easier to represent if four different components (which might be also referred as "nuclear liquids") are distinguished within a nucleus: protons with spin ↑ and ↓, and neutrons with spin ↑ and ↓. The case of $\Delta S = 1$, $\Delta T = 0$ (the **magnetic isoscalar resonances** with $\Delta L = 0, 1, 2, 3$, etc.) could be described by the oscillation of the proton-neutron component with spin ↑ against the ↓ component. On the other hand, the **magnetic isovector resonances** with $\Delta S = 1$, $\Delta T = 1$, are characterized by the proton components with spin ↑(↓), oscillating against the neutron ↓(↑) components correspondingly (see Figure 1.1).

This descriptive macroscopic interpretation of various resonances could complement our understanding of resonances if considered alongside the microscopic framework. A giant resonance can be interpreted as a coherent superposition of particle-hole excitations. An interaction of an EL or ML photon with a nucleus results in a transition of a nucleon in a certain subshell to an

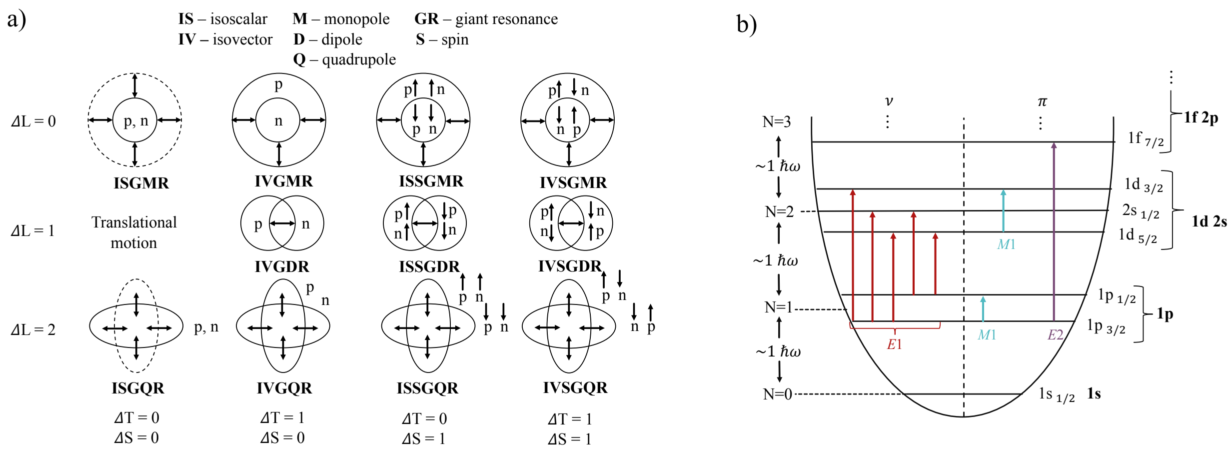

Figure 1.1: **a)** Macroscopic interpretation of different resonance modes; L stands for the multipolarity, S for spin, and T for isospin of the nucleus. **b)** Microscopic interpretation of several transitions for the simplest shell-model with a harmonic oscillator potential.

energetically higher-lying empty subshell. This results in a particle-hole state of a given spin and parity, defined by the multipolarity L and parity of the photon (1.1), the spin and parity of the nuclear ground state.

However, the single-particle approach with independent nucleons tends to underestimate the observed energies of transitions and forms a very simplified picture of the giant resonances. Introducing the residual interactions of nucleons affects the energies of induced transitions and, thus, the energy and the width of the resonance itself. In addition to the energy attributed to a 1p-1h excitation, certain amount of the energy can be distributed over more complicated 2p-2h, 3p-3h, etc. states, and this fact must also be taken into account. Involving of numerous interacting nucleons in the excitation process reflects directly its collective nature. The superposition of excitations forming a resonance can be described by an action of a corresponding one-body operator on the ground state wave function [1]:

$$\left|\Psi_{GR}^{L,S,T}\right\rangle = \mathbf{O}^{L,S,T}\left|\Psi_{g.s.}\right\rangle . \tag{1.2}$$

Since the IVGDR was the resonance predominantly observed with photon probes, it soon became evident that probes of different nature should be used to reveal other resonances. A large variety of probes, such as (e,e$'$),(p,p$'$),(p,n),(α,α'),(π^+,π^0), and (μ,ν_μ), were proposed and used to observe new resonance responses [11]. For example, inelastic electron scattering experiments revealed the isoscalar giant quadrupole (ISGQR) resonance [12], whilst the α-probes allowed to observe the isoscalar giant monopole (ISGMR) resonance [13]. The complementary probes allowed to distinguish resonances of different origin in the excitation energy ranges where they are overlapping. Alongside the later observations of spin-flip resonances, the experiments discussed form an experimental base for the deeper insight into the nuclear response under different conditions and, thus, the underlying nuclear structure.

A rapidly growing interest in the new resonance phenomena expanded not only on the observation of electric and magnetic resonances of different multipolarities, but on how a given strength ($E1$, $E2$, $M1$, *etc.*) is distributed and fragmented over a wide excitation energy range for different isotopes. Particularly, the study of progressively heavier isotopes, further away from the valley of stability could potentially reveal new excitation modes and resonances. The energy range in the vicinity of the IVGDR resonance was rather well studied in numerous experiments starting from 1960s, but the lower-lying region still needed to be addressed to. Indeed, thermal

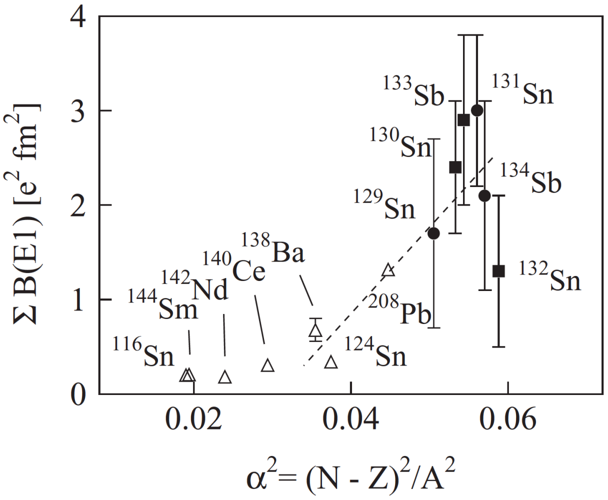

Figure 1.2: Pygmy dipole strength for unstable isotopes $^{129-132}$Sn, ^{133,134}Sb, and several stable isotopes as a function of the squared asymmetry parameter $(N-Z)^2/A^2$. Figure is taken from Ref.[14].

neutron capture experiments performed by G. A. Bartholomew and collaborators in the early 1960s revealed a new feature in the electric dipole response: an additional enhancement in the strength distribution in the vicinity of $E_\gamma \approx$ 5-6 MeV was observed for several nuclei [15]. This resonance structure was subsequently called the pygmy dipole resonance (PDR) in the work of J. S. Brzosko [16], who compared the experimental (n,γ) cross-sections with the predictions of the compound nucleus model in the presence of the PDR. It was found that an agreement with the experimental data was significantly harder to achieve if the PDR was disregarded. Therefore, more realistic calculations require the PDR to be treated together with the IVGDR.

The definition of the PDR and the question of whether a fragmented low-lying$E1$ strength could be considered a resonance structure are less evident than for the neighboring IVGDR mode. The earliest experiments related the appearance of the PDR with the presence of excess neutrons forming a diffuse neutron distribution with respect to the nuclear radius. These neutrons were found to form either a neutron skin [17] or a halo structure [18]. Moreover, there are also some theoretical indications of the PDR in proton rich nuclei [19]. While the giant resonances are identified as arising from a coherent superposition of excitations to certain states, it is still debated whether these neutrons are involved in collective oscillations with respect to the remaining proton-neutron core or result in a non-collective strength distribution.

Another important branch of the PDR studies touches upon the evolution of the low-lying strength along different isotopic lines (number of protons Z is fixed) and aims at revealing particular trends for a varying number of neutrons N. For example, Figure 1.2 demonstrates the electric dipole strength attributed to the PDR for several even-even and odd isotopes of Sn, Sb, Pb, Ba, Ce, Sm, and Nd. The strength reveals a certain trend with respect to the squared asymmetry parameter $\alpha^2 = (N-Z)^2/A^2$. As the neutron excess increases, in general, the strength increases as well. At a certain value of α, the strength might be expected to stabilize locally due to partial counteraction between the Coulomb force and the force due to the asymmetry energy, favoring formation of a neutron skin. Another important remark concerns the way these strengths were extracted: different experimental techniques might cover different energy regions, and part of the strength might be missing in some experiments.

In this relation, a consistent comparison of experimental findings on, for example, the same isotopic line is of particular importance. This master thesis is chiefly inspired with the series of studies on several Sn isotopes performed at the Oslo Cyclotron Laboratory. This complex research involved $^{116-119,121,122}$Sn studied in (^{3}He,$\alpha\gamma$) and (^{3}He,^{3}He$'\gamma$) reactions. The nuclear response was treated in terms of the γ-ray strength functions, describing the average decay properties of a nucleus. This quantity will be discussed in detail in Chapter 3. In all cases, the nuclear response reflected an enhancement in the vicinity of the neutron separation energies, which could be interpreted as the pygmy dipole resonance. An interesting observation was derived from the obtained systematics: the PDR strength does not change significantly with neutron number, although the centroid of the resonance shifts towards higher energies. Moreover, the presence of the PDR in the nuclear response was shown to affect radiative neutron capture (n,γ) cross-sections. Good agreement with experimental cross-sections was achieved, while the standard models with no PDR included underestimate the experimental cross-sections. This finding provides inspiration for the further discussions of the role the PDR might play in astrophysical neutron capture processes and, thus, the formation of the elements heavier than iron (see Section 2.3.3).

The present thesis is focused on a (p,p$'\gamma$) experiment performed on ^{124}Sn. This isotope is the heaviest even-even isotope studied at the Oslo Cyclotron Laboratory, and the extraction of the nuclear response for this isotope enables study of average nuclear properties, such as the nuclear level density and γ-ray strength function. Together with the known experimental γ-ray strength functions for the lighter Sn isotopes and external data, extracted with different experimental techniques, a more complete picture of the PDR evolution could obtained. As ^{124}Sn is the heaviest Sn isotope, it might give a clue on how the parameters characterizing the PDR change as one approaches the edge of the valley of stability. The present thesis will hopefully serve as a tiny step towards the better and more complete understanding of the PDR, its relation to the underlying nuclear structure, and its implication for astrophysical phenomena. Particularly, the lighter ^{123}Sn isotope could potentially be classified as a branching point in the slow neutron-capture process [20]. The estimation of neutron capture rate involves knowledge on statistical decay properties of the compound nucleus, in this case ^{123}Sn+n$\rightarrow$ ^{124}Sn. As the presence of the PDR in the nuclear response was shown to enhance the neutron absorption cross-sections of lighter Sn isotopes [21], this might be also expected for the ^{123}Sn neutron capture cross-section, calculated on the base of the level density and γ-ray strength function for ^{124}Sn.

The thesis is organized in the following way: the next chapter covers the most relevant questions, theoretical and experimental findings on the PDR, its nature, structure and its relation to the neutron skin thickness, equation of state, and neutron capture rates. It also contains a section devoted particularly to the Oslo Cyclotron Laboratory experiments on Sn isotopes and the major experimental information on the low-lying dipole strength distribution in ^{124}Sn. Chapter 3 contains a discussion of the γ-ray strength function and level density exploited for the description of the PDR in the present work. Chapter 4 contains all relevant experimental details, particularly, an overview of all detecting systems, experimental conditions, and the primary data selection and analysis. The so-called Oslo method used to extract the nuclear level density and γ-ray strength function for ^{124}Sn is described in detail in Chapter 5. The obtained experimental results are presented and discussed in Chapters 6 and 7. Finally, the summary and outlook will be provided in Chapter 8.

Chapter 2

The pygmy dipole resonance

2.1 The PDR in terms of the energy weighted sum rule

Historically, the resonance features appearing in the nuclear response were initially studied from the perspective of giant resonances, especially the IVGDRs: broad pronounced maxima observed in the cross-sections due to collective excitiations of protons and neutrons. It was found that these collective phenomena are present for nuclei throughout the whole nuclear chart, from the lightest ^{4}He [22], to the heaviest Th and U isotopes [23], and the bulk properties of these resonances are smoothly varying functions of the mass number A for the majority of nuclei. However, both the criterion for being a giant resonance and the degree of collectivity had to be quantified.

The microscopic picture of resonance structures provides an opportunity to approach their collective nature in terms of underlying transitions and the corresponding transition operators. The giant resonances could then be defined as exhausting the large fractions of the so-called energy weighted sum rules (EWSR), defined by the corresponding multipole electromagnetic transition operators. In order to introduce the EWSR, one should first introduce the reduced transition rate, or the transition strength, $B(\sigma\lambda, I_i \to J_f)$ in its general form [1]:

$$\begin{aligned} B(\sigma L, J_i \to J_f) = \sum_{\mu, M_f} |\langle \Psi_f | \mathscr{M}(\sigma L, \mu) | \Psi_i \rangle|^2 = \sum_{\mu, M_f} (J_i M_i L \mu | J_f M_f)^2 |\langle \Psi_f || \mathscr{M}(\sigma L) || \Psi_i \rangle|^2 = \\ = \frac{2J_f + 1}{2J_i + 1} B(\sigma L, J_f \to J_i), \end{aligned} \tag{2.1}$$

where J_i and J_f are the angular momenta of the initial and final states with the corresponding projections M_i and M_f, $\langle \Psi_f || \mathscr{M}(\sigma L) || \Psi_i \rangle$ denotes the reduced matrix element of the transition operator for a transition of type σ and multipolarity L with the corresponding projection μ, $(J_i M_i L \mu | J_f M_f)$ is the Clebsh-Gordan coefficient. In case of the electric dipole transitions $\sigma = E$ and $L = 1$ correspondingly. In the literature, the $\mathscr{M}(\sigma L)$ operator refers often to the electromagnetic radiative transitions due to absorption or emission of real photons (see *e.g* [24]). However, an excitation due to either inelastic hadron or electron interaction might also take place. In this case, transitions could be described by quite similar transition operators, taking spins and isospins of interacting particles into account alongside the interaction between incident particles and the nucleons. The energy weighted sum rule could then be introduced as the sum over all possible strengths for the excitations from the ground state to a certain final state n, weighted with the corresponding excitation energies [1]:

$$S_{\sigma L} = \sum_{n} (E_n - E_0) B(\sigma L, g.s \rightarrow n). \tag{2.2}$$

In the case of electric dipole transitions, it can be shown, that the energy weighted sum rule could be written in the following form [1]:

$$S_{E1} = \sum_{n} (E_n - E_0) B(E1, g.s \rightarrow n) = 14.8 \frac{NZ}{A} (1 + \kappa)\ e^2 \mathrm{fm}^2 \mathrm{MeV}, \tag{2.3}$$

with an additional charge-exchange correction κ, which might be estimated experimentally. The classical description of the IVGDR form is usually performed in a slightly modified form of the classical Thomas-Reiche-Kuhn sum (TRK), expressed in terms of the integrated photon absorption cross-section [26, 27]:

$$\int_{0}^{\infty} \sigma(E) dE = \frac{2\pi^2 e^2 \hbar}{mc} \frac{NZ}{A}\ \mathrm{MeV} \cdot \mathrm{mb}, \tag{2.4}$$

here, m is the electron mass, Z and A are the charge and mass number of a considered nucleus, $N = A - Z$ is the number of neutrons. This more practical (in the experimental sense) relation takes into account direct proportionality between S_{E1} and $\int_0^\infty \sigma(E) dE = const \cdot S_{E1}$. As a general rule, the resonance structure falls into the giant resonance category if the transition strengths, forming this resonance, exhaust at least 50% of the EWSR for the corresponding multipolarity of these transitions. That is the particular case of the IVGDR: it exhausts up to $\approx$ 100% of the TRK sum rule, implying that the electric dipole response is predominantly concentrated in the IVGDR energy region. However, the experimental cross-section integrated over the IVGDR region might still be underestimating the sum by several percents, even if

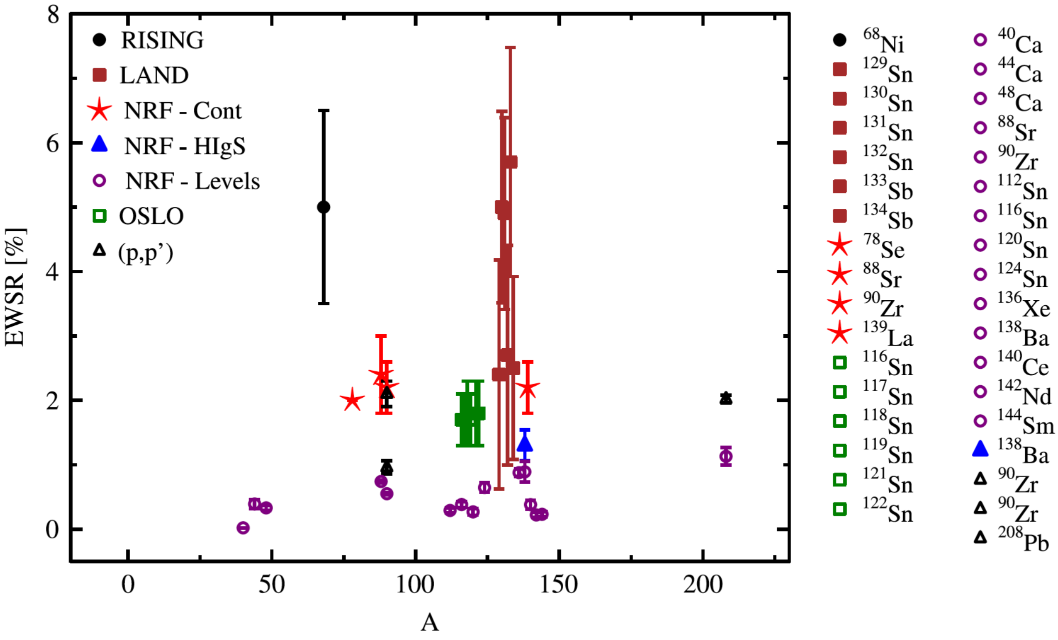

Figure 2.1: The fraction of the $E1$ EWSR for numerous nuclei, attributed to the PDR. Figure is taken from Ref. [25].

the additional corrections to the TRK sum are included. This “missing strength”was revealed before the observation of the PDR and served as an additional stimulus for further studies on the electric dipole strength distribution.

The PDR was shown to exhaust from a few percent of the TRK sum rule up to a considerable fraction of 9-10%, observed experimentally [28]. One of the open questions here is how the fraction of the TRK sum attributed to the PDR evolves for different isotopes, *e.g.* with the mass number over the nuclear chart, or for nuclei within the same isotopic line. Unfortunately, there is still no clear consistency between the ways the TRK sum fraction was extracted in different experimental methods or theory. Figure 2.1 demonstrates the fractions extracted from data sets for different isotopes as a function of the mass number A (here, the previous data on Sn isotopes from the Oslo group are listed as well). Neither a general trend nor a local trend for the same Z or A could be extracted, if one takes into account that different methods have different sensitivity to the strength observed, or could simply be limited by the neutron separation energy. In addition, the question on how the PDR should be separated from the IVGDR, in the area where they are partially overlapping, is still present. Besides, as a general rule, the extraction of the TRK sum rule fraction is model dependent. Among the data presented, the fraction of the TRK sum is either calculated for the PDR-attributed resonance peak with the IVGDR tail subtracted, or simply for a certain energy range, assumed to be dominated by the PDR response. This problem was explicitly demonstrated by D. Savran *et al*, who compared the NRF with bremsstrahlung and tagged photons with the data from the Coulomb excitation in the (p,p$'$) reaction on ^{90}Zr in forward angles (see [25] and references therein). The fraction of the TRK sum rule tends to vary from 0.55(2)% obtained with the tagged-photon method to 2.2(4)% in the (p,p$'$) reaction for the same nucleus.

2.2 A brief overview of the PDR

The low-lying electric dipole response observed in 1960s (see introduction in Chapter 1) immediately posed new questions on its macroscopic and microscopic nature. Since it is a part of the total electric dipole response, contributing to the total EWSR, it was quite natural to approach it with a similar macroscopic framework as the one applied to the IVGDR before. In order to describe both the PDR and the IVGDR, R. Mohan introduced the three-fluid hydrodynamical model of nuclei in 1970 [29]. This model is essentially based on the improved Steinwedel and Jensen (Danos) two-fluid model, treating protons and neutrons as two compressible fluids, oscillating with respect to each other with a restoring force dependent on the symmetry energy in an incompressible nucleus [30, 31]. While treating protons and neutrons in the same orbitals, Mohan distinguished a separate fluid of remaining neutrons, thus, splitting neutrons into the “blocked”and excessive neutrons. Assuming all three fluids to be compressible and contained in a spherical nucleus of a constant volume, he made an attempt to describe the strength distribution in ^{208}Pb. The IVGDR could be interpreted in both the two- and three-fluid model stemming from the oscillations of all protons with respect to all neutrons (mode centered at ≈ 13 MeV), however, the three-fluid model yields also the oscillation of excess neutrons with respect to a core of protons plus blocked neutrons (low-lying mode at $\approx 4.3 - 4.8$ MeV). The integrated cross-section of the latter mode was estimated to be $\approx$400-600 smaller than the one for the IVGDR.

The connection of the PDR to oscillations of excess neutrons presents a purely macroscopic picture of the low-lying strength, and further experiments were crucial for either verifying or rejecting this picture. Radiative neutron capture experiments performed by G. A. Bartholomew *et al.*, which led to the first observations of the PDR, were continued in the years after the collective interpretation was introduced. Resonance-like structures in the γ-ray strength functions were confirmed to be situated around 5-7 MeV for Pb, Bi, Tl, and Hg isotopes (see e.g.

[32]). These experiments inspired subsequently R. M. Laszewski and P. Axel to perform tagged bremsstrahlung photon experiments on the same targets in the energy range from 4.5 MeV up to the neutron threshold [33]. The superconducting MUSL-1 microtron was used to produce an electron beam, hitting an aluminum foil to produce bremsstrahlung photons interacting with a target of interest. Photons with a certain energy were tagged by collecting and detecting electrons, producing these photons, with a magnetic spectrometer and a counting detector array. These experiments confirmed the appearance of some well-localized dipole strength, exhausting ≈ 0.64% of the EWSR in ^{208}Pb and other isotopes; the strength was found to become more evenly distributed while moving from ^{208}Pb to Hg and Tl, having proton and neutron holes below the closed shells Z=82 and N=126. These observations were followed by experiments on the lighter Sn, Ce, and Ba isotopes revealing similar results.

The next breakthrough in our understanding of the low-lying dipole strength was marked by exploiting high-energy heavy-ion beams on various targets, performed first by I. Tanihata *et al.* [34]. Nuclear radii were measured for various He isotopes, produced by fragmentation of a primary ^{11}B beam with energy of 800 MeV/nucleon incident on Al, C, and Be targets. A similar experiment performed by T. Kobayashi *et al* [35] with a beam of ^{11}Li incident on a ^{208}Pb target revealed a strongly enhanced $E1$ strength distribution in a low-energy region.

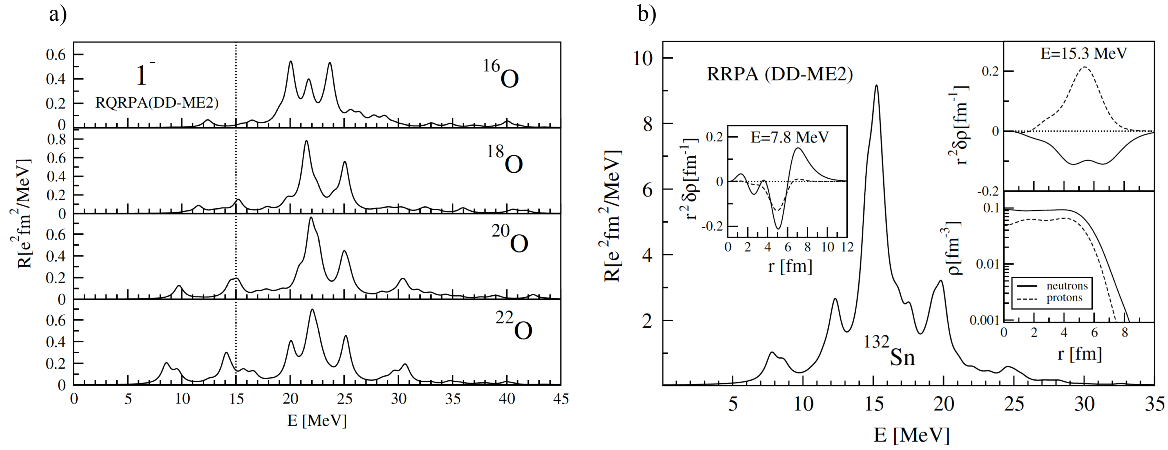

Figure 2.2: **a)** The isovector dipole strength distribution in ^{16,18,20,22}O, calculated with the RHB + RQRPA model using the DD-ME2 effective interaction. **b)** The dipole strength distribution in ^{132}Sn, calculated with the DD-ME2 effective interaction. Upper and left panel: proton and neutron transition densities for the peaks at 7.8 and 15.3 MeV excitation energies. Bottom panel: the ground-state proton and neutron densities. All figures are taken from Ref. [10].

The experimental findings on the low-lying strengths in very light nuclei and relatively heavy nuclei were attempted to be reconciled within different theoretical approaches. Numerous methods, such as the Hartree-Fock-Bogoliubov approach with effective nuclear forces, the relativistic Hartree-Bogoliubov, the quasi-particle phonon model (QPM), the Landau-Vlasov equations, relativistic implementations of RPA and QRPA, and many other approaches (see [10] and [36] for more details) were successfully applied to reproduce the the low-lying dipole strength. It was soon realized, that the strength observed for ^{11}Li and ^{11}Be could be rather attributed to a halo-like neutron structure. The tails of the wave function of one loosely bound neutron in ^{11}Be and two neutrons in ^{11}Li expand far beyond the rest of the nucleons. For the one-neutron halo systems, the low-lying $E1$ strength is tightly related to the single-particle structure of the halo neutron and is of non-resonant character; it could not be classified as the PDR within its macroscopic interpretation. Similar phenomena were observed for other light nuclei, which do not reveal a clear halo-structure. For example, a series of electromagnetic excitation experiments were carried out for several oxygen isotopes, particularly, for neutron rich $^{18-22}$O [37, 38], revealing a distributed low-lying $E1$ strength for each isotope. Subsequently, a more detailed analysis with the QRPA plus Relativistic Hartree-Bogolubov (RHB) models [39] suggested a non-resonant nature of the observed response, which could rather be interpreted as a group of independent single-particle excitations (see Figure 2.2 a)). All these findings cast serious doubts on the degree of collectivity of the PDR.

Nevertheless, as the mass number increases and one moves towards medium- and heavy mass nuclei, the structure of the low-lying $E1$ response changes; relativistic RPA calculations suggest it to be driven by bulk oscillations of excess neutrons with respect to the core [41]. For example, the RRPA calculations on the ^{132}Sn suggest a resonant nature of the low-lying $E1$ strength driven by the in-phase oscillations of protons and neutrons in the core and major contributions from excess neutrons on the surface (see [10] and Figure 2.2 b)). This picture differs from the statistical $E1$ excitations in the low-energy region for ^{16,18,20,22}O isotopes.

The discussion on the degree of collectivity of the PDR is still ongoing. While numerous RPA-based calculations (*e.g.* RQRPA for ^{132}Sn discussed above) confirm the picture of the PDR as a collective excitation mode, other self-consistent approaches do not provide such a solid evidence for the PDR being collective. This discussion is especially relevant for the light-mass nuclei. The majority of works on middle- and heavy-mass nuclei are quite consistent in providing a collective picture of the PDR, driven by the neutron skin, but the impact of the neutron skin in light nuclei on the collectivity itself is highly debated [42]. Moreover, light exotic nuclei pose an additional question: even if the low-lying strength of non-resonant nature is explained by the single-particle nature of loosely bound neutrons, are these neutrons attributed to the skin structure or the neutron halo? The vague borderline between halo and skin contributions to the resonant *vs.* non-resonant groups of low-lying states is one of the burning questions and problems to be solved.

The first observations of the PDR with neutron absorption experiments formed the base for general study on how the PDR evolves in various isotopic lines with increasing number of neutrons. Such systematic studies were largely boosted with the development of high-resolution Nuclear Resonance Fluorescence experiments (NRF). The first studies of the PDR using this technique were performed by K. Govaert *et al.* [43] on ^{116}Sn and ^{124}Sn for energies up to the

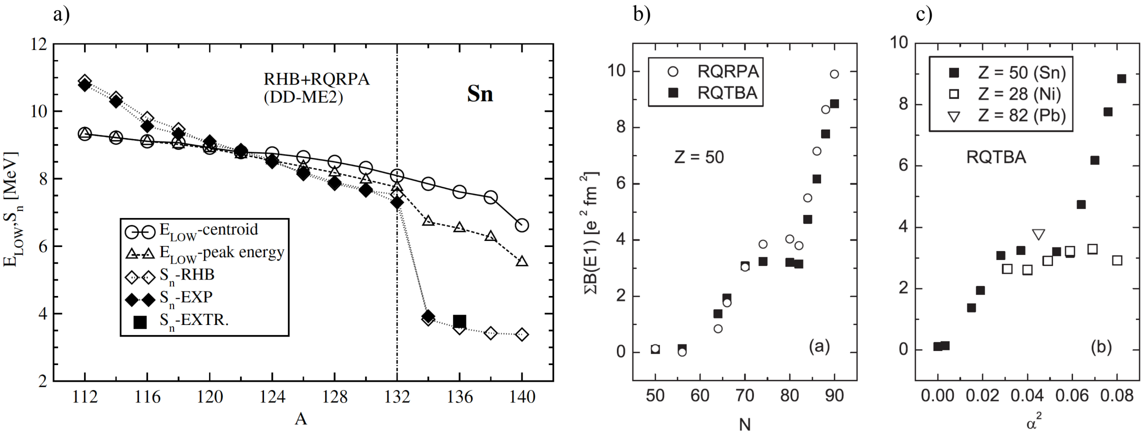

Figure 2.3: a) Peak and centroid energires of the PDRs for Sn isotopes, calculated with RHB + RQRPA, and neutron separation energies (experimental values, RHB calculations and extrapolated values). Figure is taken from Ref. [10]. **b-c)** Integrated dipole strength for the PDR region calculated within the RQTBA as a function of neutron number for Sn and squared asymmetry parameter $\alpha^2 = (N - Z)^2/A^2$ for Sn, Ni, and Pb. Figure is taken from Ref. [40].

neutron separation energy around ≈ 9 MeV. This experiment was complementary to the previous tagged photon bremsstrahlung studies on ^{Nat}Sn [44]. Due to superior resolution, individual states were identified and both the fragmentation and fine structure of the $E1$ strength distribution were determined in a model-independent way. Both isotopes revealed a clear concentration of $E1$ strength around 6.5 MeV, and the integrated $B(E1)$ value was found to be larger for ^{124}Sn. Followed by other NRF experiments for the Sn isotopic chain and other elements, both the experimental findings and theoretical predictions pointed to an increase of the low-lying strength with increasing mass number. For example, thorough studies of the Sn line within the quasiparticle time blocking approximation RQTBA and RQRPA [10, 40] demonstrate a smooth shift of the PDR centroid towards lower energies. In addition, both the centroid and the peak energy were found to exceed the neutron separation energy for heavier isotopes (see Figure 2.3 a)). Similarly, the integrated dipole strength for the PDR was found to be an almost monotonous function of N, with a fast increase after the $N = 82$ shell closure, and the squared asymmetry parameter $\alpha = (N - Z)/A$ for Sn isotopes. For Ni isotopes the latter feature is less prominent, implying that the asymmetry dependence of the PDR strength is less apparent (see Figure 2.3 b)). On the other hand, the RHB + RQRPA calculations [10] demonstrate a pronounced maximum of the total low-lying dipole strength with a local minimum for the magic ^{132}Sn isotope, followed by a fast increase as shown in Figure 2.4 a). This feature of the strength evolution might be due to the impact of the shell effects and reduced pairing correlations in the vicinity of the $N = 82$ shell closure.

Theoretical studies of the PDR evolution were accompanied by pioneering experiments on the unstable nuclei ^{130}Sn and magic ^{132}Sn performed at GSI [45]. A secondary beam, containing both isotopes, was formed after in-flight fission of the primary ^{238}U beam incident on a Be target. Beams of interest were selected with the magnetic separator and directed to a ^{208}Pb target. Momenta and energies of neutrons, photons and recoil fragments were measured. This experiment provided a certain evidence for both the PDR and the GDR in both isotopes and confirmed to a large extent the theoretical predictions (see Figure 2.4 b)). However, there was a limitation present: the strength was measured only for energies above the neutron threshold. Even though the centroid of the PDR is shifted above this value in ^{130,132}Sn, there is no available

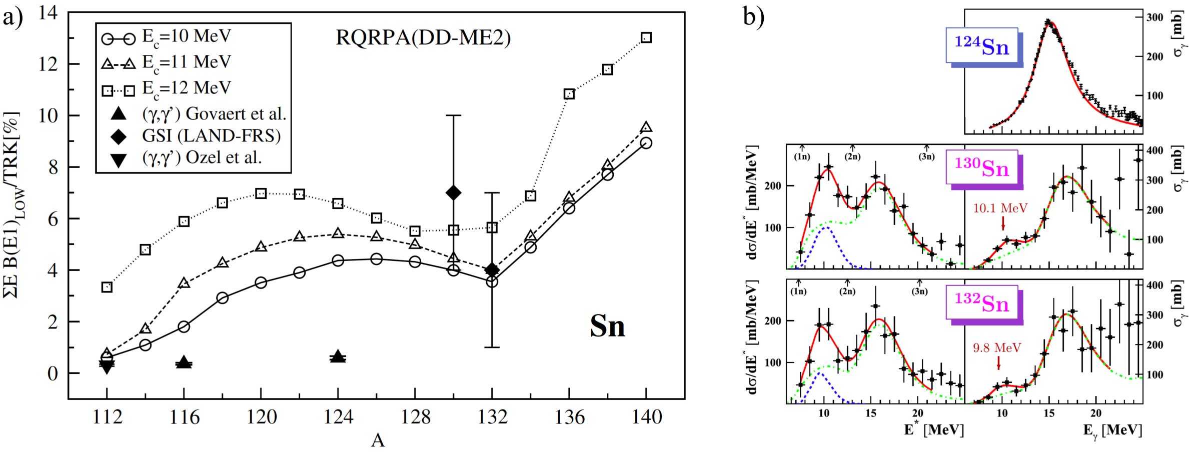

Figure 2.4: **a)** The RHB + RQRPA energy-weighted dipole strength in percent of the TRK sum rule, calculated for the different energy ranges up to E_C and experimental results. Figure is taken from Ref. [10]. **b)** Left panel: differential electromagnetic dissociation cross-sections measured in ^{130}Sn and ^{132}Sn. Right panel: deduced photoneutron cross-sections; blue dashed line denotes the fitted Gaussian distribution, green dash-dotted line denotes the Lorentzian distribution, red solid line marks the total fit . Upper panel: photoneutron cross-section in the stable ^{124}Sn from a real-photon absorption experiment. Figure is taken from Ref. [45].

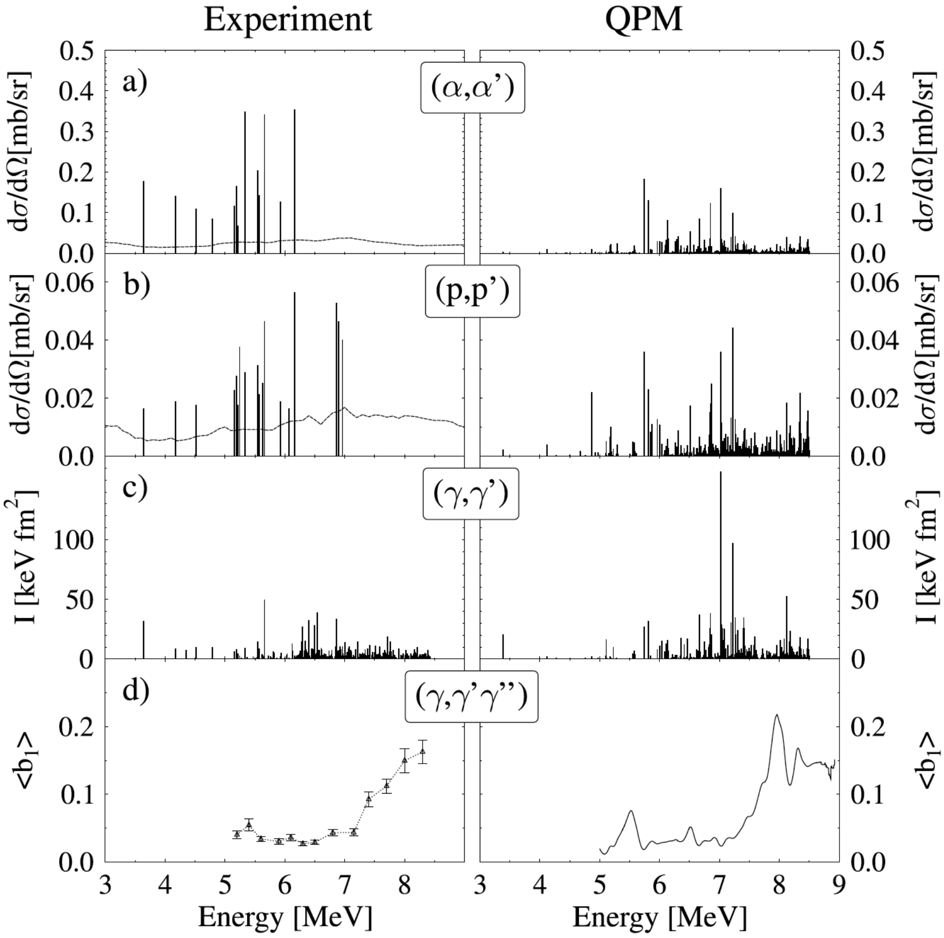

Figure 2.5: Left panel: experimental differential cross-section values for ^{140}Ce, a) results for the (p,p$'$) experiment, b) for the (α, α') experiment, c) for the NRF study, d) measured averaged branching ratio to the first excited state from $(\gamma, \gamma'\gamma'')$ data. Right panel: QPM prediction for the same probes. Figure is taken from Ref. [46].

information on the low-energy PDR tail. On the other hand, the NRF studies are limited by the neutron separation energy from the low-energy side, and the information on the upper tail of the PDR is absent. Therefore, any studies with complementary experimental techniques, covering the whole PDR range, are crucial for deducing the full $E1$ strength for both stable and exotic nuclei.

Another interesting aspect to be studied is the underlying nature of the PDR, namely the origin of oscillations forming the PDR in its macroscopic interpretation. The isovector structure (out of phase oscillations of protons and neutrons) of the neighboring IVGDR is well studied, while the region of the PDR and its connection to the IVGDR are still highly debated. From an experimental point of view, a study of the same phenomenon performed by means of complementary probes inducing the interaction of different nature could hopefully provide good clues to the nature of the phenomenon itself. As already mentioned, the large database on the PDR obtained from NRF studies is available. Photoabsorption is governed by the well known electromagnetic mechanism of interaction with a nucleus as a whole. The electric dipole transitions, induced by this mechanism, are known to be of isovector nature. On the other hand, the isoscalar (in phase) component of a response could be studied with the isoscalar hadron probes. The best experimental tool to induce isoscalar resonances (or the corresponding component of a resonance) is the inelastic (α, α') scattering due to the zero isospin and ability to induce predominantly

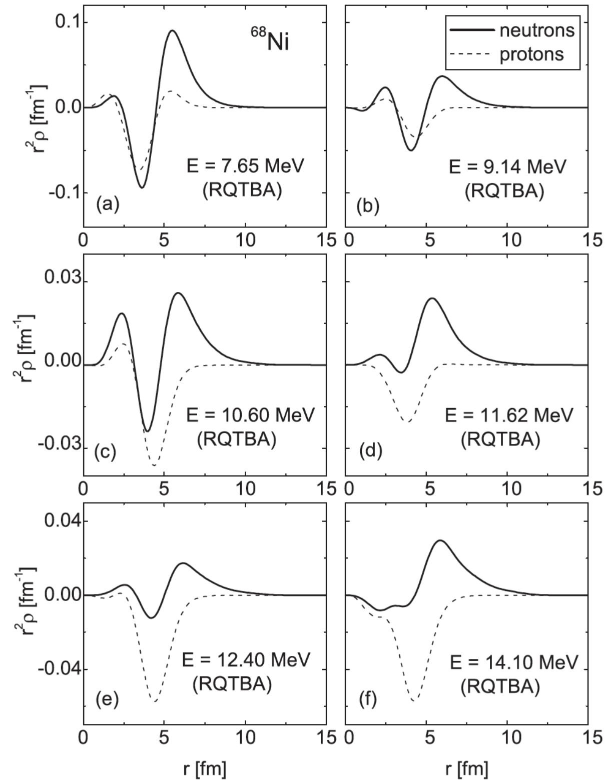

Figure 2.6: RQTBA transition densities for the low-lying dipole states in ^{68}Ni. The dashed curves denote the proton, and the solid curves denote the neutron transition densities. The figures are taken from Ref. [40].

surface excitations [1]. A comparison of these two probes has been performed for the semi-magic ^{140}Ce nucleus. Recently, this study was completed with an additional (p,p$'\gamma$) experiment with 80 MeV protons at the KVI facility in Groningen [46]. It provided a unique comparison of the total experimental cross-sections for three complementary probes with theoretical QPM predictions (see Figure 2.5). Both hadron probes interact with the nucleus via both the electromagnetic and the strong nucleon-nucleon (N-N) interaction of predominantly isovector and isoscalar nature respectively. The decomposition of the experimental cross-sections into these components revealed a major isoscalar (strong N-N) nature of the PDR transitions with a small isovector (Coulomb) admixture, excited with both hadron probes. This decomposition implies that the comparatively large cross-sections observed for the low-lying 1^- states below 6 MeV for the (α, α') reaction are mostly due to an oscillation of excess surface neutrons with respect to the core. This mode corresponds to in-phase oscillation of protons and neutrons forming the core, in contrast to the out-of-phase mode of the IVGDR. The (p,p$'\gamma$) reaction was found to be less sensitive to the isoscalar component of the response. Moreover, the cross-sections for the observed transitions were significantly smaller than that for the α-probe. Both probes, however, reveal almost no response above 6 MeV. Therefore, one might assume a predominantly isovector nature of transitions above this energy. Indeed, a large amount of transitions could be observed in the NRF study. This part of the nuclear response is naturally attributed to the low-energy tail of the IVGDR, while isoscalar transitions are often considered to be the true PDR.

It is sometimes convenient to interpret the underlying nature of low-lying states in terms of transition densities. In the RPA approach, they are written in terms energy-dependent amplitudes $X_{ph}(\omega)$ and $Y_{ph}(\omega)$, describing the wave function of a selected excited state in terms of particle-hole and hole-particle excitations [47]:

$$\rho(EL,\omega,r) \sim \sum_{ph}[X_{ph}(\omega) + Y_{ph}(\omega)]R_p(r)R_h(r), \tag{2.5}$$

where L is the transition multipolarity, $R_{p,h}(r)$ are the radial parts of the single-particle and hole wave functions. Transition densities could be used for the descriptive interpretation of how protons and neutrons are distributed for a certain excited state of a nucleus. For example, transition densities for protons and neutrons were estimated in the framework of the RQTBA for several low-lying dipole states in the calculated spectrum for ^{68}Ni (see [40] and Figure 2.6). The lower-lying peaks at 7.65 and 9.14 MeV demonstrate rather in-phase oscillations of protons and neutrons in the range up to 5 fm in the nucleus. Further, towards the nuclear surface, the neutron transition density dominates over the fast dropping proton density. Three higher-lying states are of essentially mixed isoscalar-isovector nature, as proton densities become more dissynchronized with the neutron densities. Finally, the highest peak at $\approx$ 14 MeV is almost purely off the isovector structure, as one should expect for the energy range of the IVGDR.

2.3 Implications of the PDR: experimental findings and theoretical predictions

2.3.1 Neutron skin thickness

Even though the degree of collectivity, attributed to the PDR, is still highly questioned, numerous phenomenological, microscopic nonrelativistic and transport models interpret the PDR as arising from the collective motion of excess neutrons, or neutron skin, with respect to the proton-neutron saturated core. Given this relation, the following question could be posed: how is the pygmy dipole strength related to the neutron skin thickness and what are the consequences of this relation?

The neutron skin thickness could be simply defined by the difference of neutron and proton root-mean-square radii in a nucleus. While the proton radius could be extracted from electromagnetic-interaction experiments (*e.g* elastic electron scattering), the experimental data on neutron radii are quite scarce: they require strongly interacting probes implying a convoluted model-dependent interaction mechanism. These experiments involve antiprotonic atoms and elastic proton scattering (see [2] and references therein). On the other hand, the electroweak interaction could also be exploited. For example, an elaborate parity-violating electron scattering technique was applied in The Lead Radius Experiment (PREX) in order to determine the neutron root-mean-square radius of ^{208}Pb [48]. It was shown that the parity-violating asymmetry [1] is linearly correlated with the neutron skin thickness [49], and the value $r_{skin} = 0.33^{+0.16}_{-0.18}$ fm was obtained. The values extracted in these experiments still need to be compared with other benchmarks, and the PDR strength could possibly be a good candidate for it.

The relation between the pygmy dipole strength and the neutron skin thickness has induced long standing debates. Firstly, a linear trend was traced by J. Piekarewicz between the fraction of EWSR for the PDR region (5-10 MeV) with respect to the GDR region (10-25 MeV) and the neutron skin thickness in a series of Sn isotopes [50]. These calculations were performed with the mean-field relativistic RPA model. Despite the strong linear increase (similar could be seen in Figure 2.7), a certain downward trend was revealed for the heaviest Sn isotopes, starting from ^{120}Sn. This feature was explained by the presence of the large angular momentum neutron orbital $1h_{11/2}$, which participates weakly in low-momentum and low-energy transitions, but still

---

[1] The difference of the elastic electron-nucleus differential cross-sections for incident electrons with positive and negative helicities divided by their sum

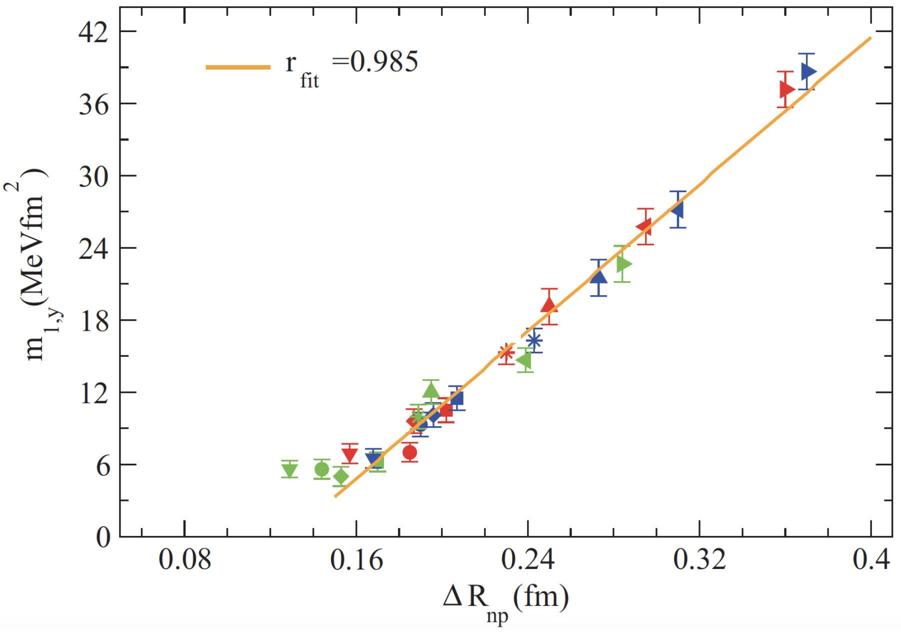

Figure 2.7: The EWSR exhausted by the PDR as a function of neutron skin for ^{108}Sn (empty up-triangles), ^{106}Sn (down-triangles), ^{124}Sn (stars), ^{132}Sn (left triangles), ^{140}Sn (right triangles), ^{48}Ca (circles), ^{68}Ni (squares), ^{86}Kr (diamonds), ^{208}Pb (full up-triangles). Calculations are performed with the Landau-Vlasov kinetic equations in the mean-field approach. Figure is taken from Ref. [53].

contributes to the neutron skin. Later, a large study was carried out by P.-G. Reinhard and W. Nazarewicz, who proposed several observables and studied their correlation with the neutron skin in a correlation analysis. It was found a rather weak correlation between the low-energy E1 strength and the neutron skin. On the contrary, another strongly correlating parameter was found: the dipole polarizability [51], which could be obtained from the inverse EWSR as [52]:

$$\alpha_D = \frac{\hbar c}{2\pi^2}\int_0^\infty \frac{\sigma_{abs}(E)}{E^2}dE = \frac{8\pi}{9}e^2\int_0^\infty \frac{R_{E1}(E)}{E}dE, \tag{2.6}$$

where $\sigma_{abs}(E)$ is the photoabsorption cross-section, and $R_{E1}(E)$ is the $E1$ response. The dipole polarization, due to its proportionality to the inverse EWSR, tends to weigh the PDR contribution more that the higher lying IVGDR. Thus, even if the contribution to the dipole EWSR from the PDR could be quite modest (5-8%), the corresponding contribution to α_D would be significantly larger (20-25%). However, the electric dipole response in the energy range including both the PDR and IVGDR is still required.

These contradicting results have been recently revised again by J. Piekarewicz *et al.* in [2, 54], who studied ^{56,68,78}Ni isotopes in the mean field RPA approach and came to the conclusion that both the low-lying strength and dipole polarizability are strongly correlated with the neutron skin thickness in ^{208}Pb. Therefore, both values could serve as constraints for $R_n - R_p$. Even though the correlation between α_D and $R_n - R_p$ was found to be weaker than for the low-lying $E1$ strength, extracting the neutron skin thickness in this case does not require the challenging separation of the PDR and the lower tail of the IVGDR.

The burning discussion of the ^{208}Pb case and the estimate of its neutron skin thickness was primarily inspired by the relation between its neutron radius and several properties of neutron stars, emphasized in numerous works, *e.g.* [48, 55]. Heavy nuclei have a neutron skin of a certain thickness. Depending on what pressure of neutron-rich mater is established, one could judge on a value of this thickness: the higher the pressure, the thicker this neutron skin would be. This pressure could be naturally linked to the neutron-rich matter pressure in neutrons stars, which counteracts gravitational collapse. The models, describing such matter, often rely on the information on neutron skin thickness in heavy nuclei, and the thicker the skins used, the larger neutron star radii will be obtained. On the other hand, this pressure also defines the transition between the uniform liquid mantle in a neutron star and the non-uniform solid crust above it. As mentioned, a high pressure would yield thick neutron skins in heavy nuclei, but in the case of neutron stars, a high pressure would indicate a low transition density from the crust to the mantle, meaning a thinner crust in the star. This exciting and far-reaching application of the neutron skin thickness allows us to extent the range of studies exploiting the data on the PDR from understanding of the nuclear structure and nuclear properties to description of features of astrophysical objects, such as neutron stars. However, the latter discussion should also involve the so-called equation of state, described in the following subsection.

2.3.2 The equation of state and the symmetry energy

The potentially strong correlation between the PDR and the neutron skin radius links the neutron skin thickness to the symmetry energy of the equation of state (EoS). The latter represents the energy per nucleon in asymmetric matter. It is often convenient to consider its Taylor expansion with respect to the asymmetry parameter $\alpha = \frac{N-Z}{A}$ [56]:

$$E(\rho, \alpha) = E(\rho, 0) + S_2(\rho)\alpha^2 + S_4(\rho)\alpha^4 + ..., \tag{2.7}$$

where $E(\rho, 0)$ is the density-dependent energy per nucleon for symmetric matter. Considering the PDR strength, the most interesting term of the expansion is presented by the symmetry energy $S_2(\rho)$, defined by the properties of the nuclear forces. It could be parametrized in the following way:

$$S_2(\rho) = a_4 + \frac{{p_0}^2}{\rho_0}(\rho - \rho_0) + \frac{\Delta K_0}{18\rho_0^2}(\rho - \rho_0)^2 + ... \tag{2.8}$$

The parameters in this equation are the saturation (equilibrium) density ρ_0, the symmetry energy in pure neutron matter a_4, the symmetry energy pressure p_0, and, finally, the correction for incompressibility, ΔK_0.

The EoS is pivotal for the description of dense neutron matter, and, particularly, neutron stars. As all the input parameters of the EoS are identified, the Tolman-Oppenheimer-Volkoff equations could be used to extract the neutron star radius, moment of inertia, surface red shift and binding energy [57]. Therefore, any experimental and theoretical nuclear constraints on the parameters included into the EoS are strongly required to extend it to sufficiently higher energies. Studies of the PDR strength and the way it evolves and correlates with the neutron skin thickness could allow us to judge on how the EoS parameters correlate with neutron skin and, hence, the strength of the PDR.

Indeed, as shown in [56], the neutron skin thickness plotted as a function of a_4 for different mean field models with a good fit to experimental constraints for ^{208}Pb (binding energies, proton radii, *etc.*) demonstrates a clear linear trend. The deviating slopes have a purely model-based reason to occur: as one of the parameters (a_4) is varied, the fit to known experimental data will be inevitably deteriorated and other parameters have to be changed as well. That makes the whole study of neutron skin thickness as a function of a_4 solely quite challenging. A similar trend was observed for the symmetry-energy pressure and the incompressibility correction ΔK, implying that all the mentioned parameters are strongly correlated to each other (see Figure 2.8). This linear correlation between $R_n - R_p$ and a_4 was lately supported for ^{130,132}Sn on the

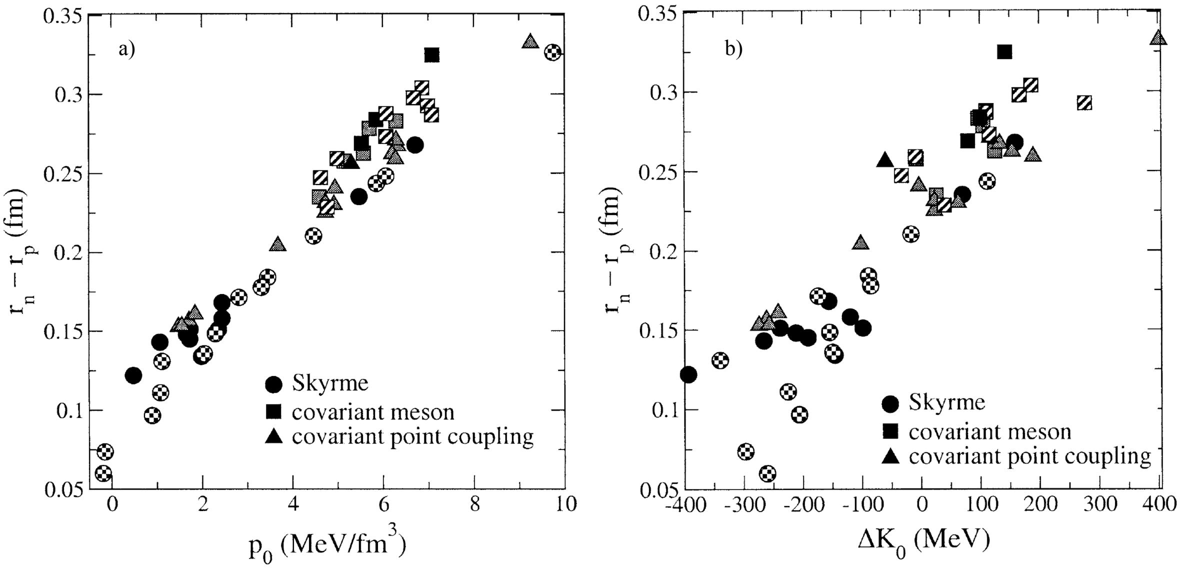

Figure 2.8: **a)** Neutron skin thickness in ^{208}Pb plotted vs. the symmetry energy pressure p_0 for several mean-field models. **b)** Neutron skin thickness in ^{208}Pb plotted vs. the incompressibility parameter p_0 for several mean-field models. Figure is taken from Ref.[56].

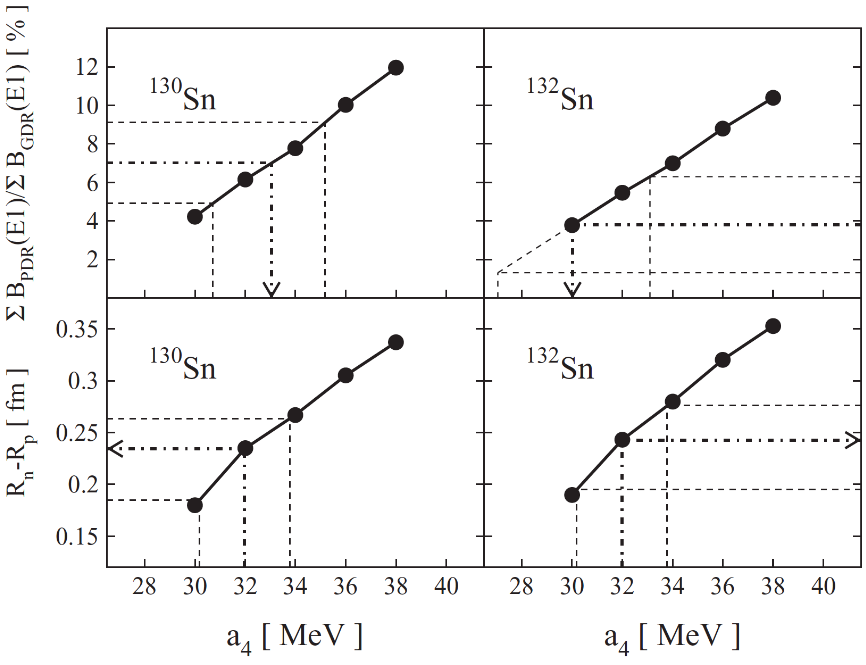

Figure 2.9: Upper panels: ratio of the PDR to IVGDR strength for ^{130,132}Sn as a function of the symmetry-energy parameter a_4. The dot-dashed and dashed lines denote the experimental ratio of the strengths for the PDR to the IVGDR with the corresponding errors. Bottom panels: neutron skin thickness as a function of a_4. Figure is taken from Ref. [14].

basis of the RQRPA calculations [14]. The trend was deduced for the relative fraction of the total PDR strength with respect to the total IVGDR strength (see Figure 2.9). A comparison of the experimentally measured strengths and theoretical RQRPA predictions yielded an average value of $\bar{a_4} = 32.0 \pm 1.8$ MeV. Furthermore, the correlation between a_4 and p_0 was established, and the corresponding value $\bar{p_0} = 32.0 \pm 0.8$ MeV·fm^{-3} was obtained. The neutron skin thicknesses for both nuclei for a given average value of a_4 were deduced to be 0.23 ± 0.04 fm for ^{130}Sn and 0.24 ± 0.04 fm for ^{132}Sn.

It should be noticed that this combined theoretical-experimental procedure yields the absolute values of crucial EoS parameters within a certain theoretical framework, if both the pygmy and giant dipole strengths are measured experimentally. One of the debated applications of this technique is tightly related to constraining a peculiar cooling mechanism of neutron stars. C. J. Horowitz and J. Piekarewicz described the so-called direct URCA cooling process in neutron stars and its relation to the neutron skin thickness in ^{208}Pb [58]. This cooling process implies a neutrino born in the decay of a baryon or its interaction with a lepton, which carries a certain energy away from the neutron star, thus, cooling it. A high fraction of protons present in a neutron star is required for this process to take place. This fraction could be determined from the EoS, which is on its own turn constrained by the neutron skin thickness, particularly that for ^{208}Pb. It was shown that the direct URCA process is possible for $R_n - R_p > 0.25$ fm, otherwise other cooling mechanisms should be involved. Accurate constraints on the ^{208}Pb neutron skin could, therefore, shed some light on how a neutron star evolves.

2.3.3 Effect on the astrophysical neutron capture rates

An exceptionally good agreement in quantitative conclusions on how the PDR affects radiative neutron capture rates has been demonstrated in numerous recent works [59, 60]. It has been shown that the presence of the PDR in the nuclear response would yield an increased (n,γ) reaction cross-section as compared to predictions where the PDR is disregarded.

The impact of the low-lying dipole strength on (n,γ) cross-sections can be of particular interest and importance for astrophysical applications. Light and medium mass nuclei up to nuclei in the iron group (nuclei in the vicinity of ^{56}Fe, ^{56}Ni, including Zn) are formed either during the burning stages of stellar evolution or in explosive environments. On the other hand, heavier neutron-rich nuclei could are produced in one of the following neutron capture processes: the slow neutron capture (s-process) or rapid neutron capture (r-process) [2] [61]. The former process requires so-called seed nuclei (*e.g.* ^{56}Fe), and, therefore, is dependent on the products of the preceding stellar and explosive nucleosynthesis. The s-process is driven by neutron densities of $\gtrsim 10^8$ cm^{-3} and lasts from approximately 1 million to 100 million years, depending on the mass of the star it takes place in. In this case, the neutron capture rate is exceeded by the β-decay rate of newly formed unstable nuclei. On the contrary, the r-process is indeed worthy its name: it takes about 1-2 s to form heavy neutron rich-nuclei far away from the valley of stability. This extremely short time requires a considerably higher neutron density of $\approx 10^{22}$ cm^{-3}, which make the neutron capture rates higher than those for the β-decay. As the neutron flux ceases, the unstable nuclei produced would decay back toward the stability valley, forming heavy nuclei up to actinides (*e.g.* U and Th isotopes).

As it was shown by F. Giacoppo *et al.* [62], the γ-strength functions obtained with the Oslo method (see Chapter 5) for ^{195,196}Pt revealed a double-humped structure within the 4-8 MeV exitation energy region. The most prominent resonance was assumed to be attributed to the PDR. Neutron capture cross-sections were calculated on base of the statistical Hauser-Feshbach model [63], which exploits the γ-ray strength function as one of the main components. The calculations with the reaction code TALYS [64] clearly demonstrate an increase of $\sigma(\mathrm{n},\gamma)$ (see Figure 2.10) as compared to the calculations without the experimental low-energy enhancements included, The obtained cross-section was found to be ≈ 2 times larger than the one without the PDR, thus, being able to reproduce the experimental values better. A similar increase in the cross-section was observed in [60], where the Relativistic Quasiparticle Time Blocking Approximation (RQTBA) was tested alongside different γ-strength function models (see Ref.

---

[2] It is sometimes convenient to distinguish the intermediate neutron capture process (i-process), which is generally similar to the s-process, but requires significantly higher neutron densities and fluxes [61].

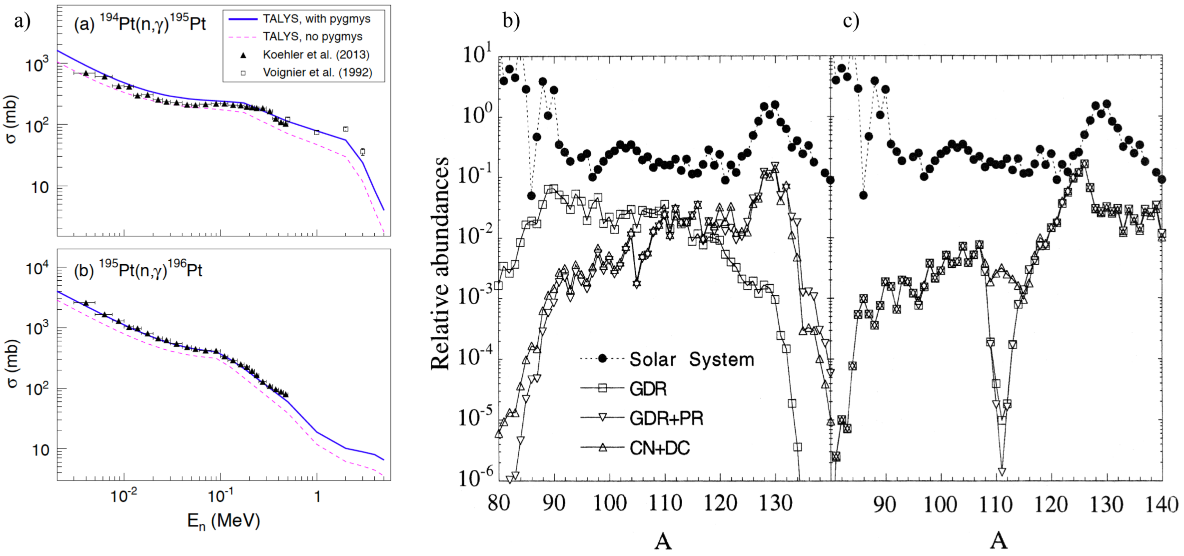

Figure 2.10: **a)** Neutron capture cross-sections for ^{194,195}Pt. The blue solid and dashed magenta lines denote the calculated cross-section including the PDR and without the PDR. Figure is taken from Ref. [62]. **b)** r-abundance distributions for a temperature of $T = 10^9$ K, neutron density $n_n = 10^{20}$ cm^{-3}, and irradiation time 2.4 s. Three different contributions are included: the standard IVGDR component, the IVGDR and the PDR strength, and the damped compound-nucleus model with direct capture included. **c)** The same calculations for $T = 1.5 \cdot 10^9$ K, neutron density $n_n = 10^{28}$ cm^{-3}, and irradiation time 0.3 s. Figure is taken from Ref. [59]

therein). The calculations were performed for the neutron deficient ^{106}Sn, stable ^{116}Sn, and neutron rich ^{132,140}Sn isotopes. All the models revealed no noticeable enhancement in the vicinity of the neutron separation energy for ^{106}Sn, while both ^{132}Sn and ^{140}Sn displayed a prominent $E1$ response only in the RQTBA approach. The radiative neutron capture cross-sections calculated with the RQTBA $E1$ strength were found to be larger than the estimates based on the γ-ray strength functions from other models with no PDR included. This effect on the cross-section could result in a change in estimated abundances of nuclei produced in the r-process. As it was demonstrated by S. Goriely [59], the contribution due to the PDR allows to reach a better agreement between the estimated and the Solar System abundances for elements with $A > 120$. It was demonstrated that the IVGDR would generally enable production of elements with $A \sim 90-110$, as the PDR would contribute to the overall increase of neutron capture rates and, thus, the abundances of heavier elements (with $A \sim 130$) would also increase. It is important to notice that these simplified simulations do not necessary represent realistic astrophysical conditions, *e.g.* such as for a neutron star merger scenario.

2.4 The PDR in tin isotopes

Theoretical predictions on the evolution of the PDR with increasing number of neutrons as well as the mixed isoscalar-isovector nature of the low-lying dipole strength have to be either verified or refuted in a series of consistent experiments. The chain of Sn isotopes is quite unique in this respect: there are numerous theoretical estimates with various models available, the experimental base is rich and extended up to the very neutron rich magic ^{132}Sn. In particular, the latter makes possible to study behavior of the low-lying strength, as a nucleus approaches the $N = 82$ shell closure.

One of these systematic studies was performed at the Oslo Cyclotron Laboratory on the

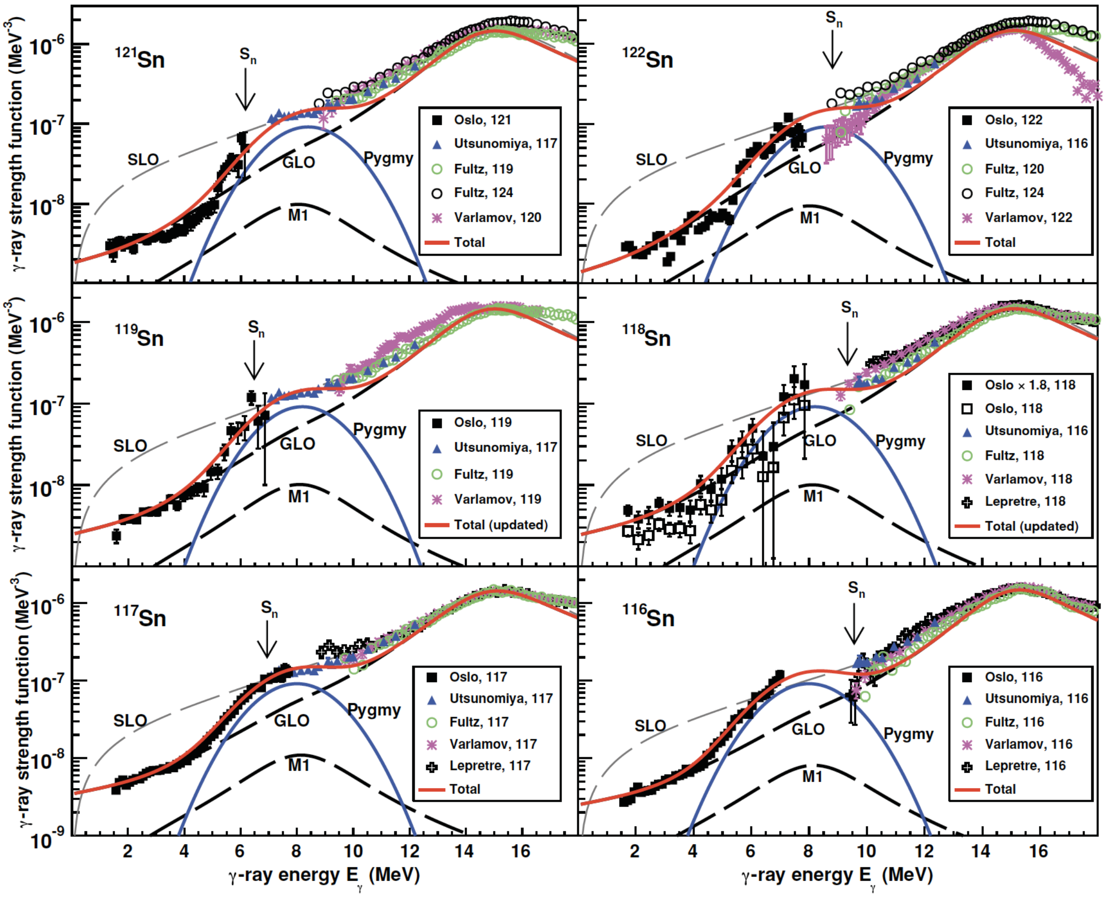

Figure 2.11: Comparison of the OCL γ-ray strength functions and the strengths obtained in various (γ,n) experiments for the $^{116-119,121,122}$Sn isotopes. "GLO"denotes the Generalized Lorentzian function, "SLO "denotes the Standard Lorentzian function. Taken from ref. [21], for the (γ,n) experiments see references therein.

$^{116-119,121,122}$Sn isotopes; results were reported in references [65–67] and summarized by H. K. Toft in [21]. The experiments involved extraction of the γ-ray strength functions and level densities (described in details it the next chapter) from (^{3}He,$\alpha\gamma$) and (^{3}He,^{3}He$'\gamma$) reactions by means of the Oslo method (see Chapter 5). All the strengths extracted are presented in Figure 2.11. All studied isotopes revealed indications of the PDRs appearing in the vicinity of the neutron separation energies. This study demonstrated several intriguing results. Firstly, the integrated dipole strength, attributed to the PDR, and the corresponding fraction of the TRK sum rule were found to be almost constant as one moves from the lightest ^{116}Sn to the heaviest ^{122}Sn isotope. Several contradictory theoretical predictions for the strength evolution were considered in an attempt to explain these results. In a large number of studies (*e.g* macroscopic calculations with the Goldhaber-Teller model by P. Van Isacker *et al.* [68]), a monotonous increase of the strength is expected to be observed. In contrary, as already mentioned, the RHB+RQRPA calculations presented by N. Paar *et al.* [10] demonstrate a local maximum for the strength for ^{124}Sn, a monotonous decrease while approaching the $N = 82$ shell closure, followed by a strong increase of the strength again. Other studies might confirm the trend seen in the Oslo experiments, *i.e.* the strength remains almost constant for the mass region in the vicinity of $A = 120 - 126$ (see [21] and Ref. therein). In addition to the integrated strength, the PDR was observed to be shifted towards higher energies, demonstrating a clear linear trend of the PDR centroid with respect to the mass number A. This result is unexpected as numerous

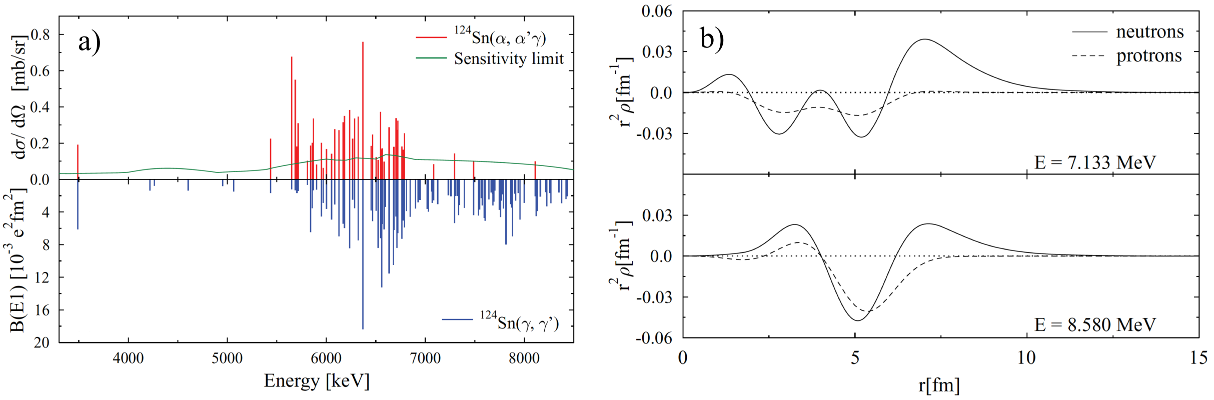

Figure 2.12: **a)** Upper panel: differential cross-sections for the excitation of states with $J^{\pi} = 1^{-}$ in the $(\alpha, \alpha'\gamma)$ experiment on ^{124}Sn. Lower panel: Distribution of the $B \uparrow (E1)$ strength in the (γ, γ') experiment on ^{124}Sn. **b)** RQTBA transition densities in ^{124}Sn for the excited state at 7.133 MeV and the excited state at 8.580 MeV. Protons and neutrons are denoted by dashed land solid lines correspondingly. Both figures are taken from Ref. [70].

calculations, such as RHB+RQRPA [10], HFB and QPM [69], predict a monotonous decrease of the PDR energy. In the perspective of clarifying both these trends, the present study of the heavier ^{124}Sn might be especially relevant. It presents the heaviest Sn isotope studied so far at the OCL. The question on the PDR evolution will be discussed in detail in Chapter 7.

The ^{124}Sn isotope has already been considered in several experimental studies with probes of different nature. The NRF experiment on ^{124}Sn, performed by K. Govaert *et al.* [43] was already mentioned in Section 2.2. The comparison of the measured strength distribution, performed by means of this isovector (γ, γ') probe, and the later experiment with the isoscalar $(\alpha, \alpha'\gamma)$ probe revealed an important feature of the PDR [70]. An abruptly dropping differential cross-section around $E_x \approx 6 - 8$ MeV could be clearly observed in the $(\alpha, \alpha'\gamma)$ data. In contrary, the NRF yields a strength distribution up to the neutron separation energy (see Figure 2.12). This observation is similar to that in other $N = 82$ isotopes, such as ^{140}Ce (discussed in Section 2.2) [46] and ^{138}Ba [71]. Subsequent RQTBA calculations of the transition densities for two states in this energy region confirmed a transition between the PDR and the IVGDR regions. In-phase oscillations of protons against neutrons with the dominant neutron oscillations on the surface were revealed for the lower-lying 7.133 MeV state (see Figure 2.12). In contrary, the slight shift in phases between proton and neutron transition densities for the 8.580 MeV state above the neutron separation energy indicates that the state could be attributed to the tail region of the IVGDR rather than the PDR.

A similar disappearance of the low-lying strength was subsequently observed for the (^{17}O, ^{17}O$'\gamma$) probe [72]. The differential cross-section attributed to the ground state decay spectrum demonstrated a splitting of a low-lying strength into a low-energy isoscalar component and a higher lying group of states with predominantly isovector nature. Comparing all the probes, the integrated strengths below 7 MeV and above it appear to be quite similar for the NRF experiment. For the $(\alpha, \alpha'\gamma)$ and (^{17}O,^{17}O$'\gamma$) the majority of strength observed is concentrated in the lower-lying excitation energy region, while excitations in the higher region are significantly suppressed.

Finally, a recent (p, p$'$) experiment performed at the Research Center for Nuclear Physics (RCNP) in Osaka, revealed an $E1$ strength distribution similar to that from the NRF experiment [73] for the even-even isotopes ^{112,114,116,118,120,124}Sn. It displayed a same peak-like structure in the vicinity of 6.5 MeV for all isotopes, previously unobserved in the OCL experiments. These data cover the E_γ range above 6 MeV, and the strength obtained in the present (p,p$'\gamma$) experiment will provide an extension of the nuclear response towards lower energies.

Chapter 3

Nuclear properties in the quasi-continuum energy range

3.1 The nuclear level density

One of the fundamental nuclear properties to be extracted, analyzed and discussed in the presented work is the nuclear level density. This value was shown to be of particular interest in various nuclear aspects, especially nuclear structure and reaction models applied to nuclear astrophysics. This poses new relevant questions and problems, namely what experimental techniques could be used to extract the level densities in a most efficient way and how they could be approached theoretically. The former would allow us to estimate the way level densities evolves for the nuclei along the stability line or even for the adjacent β-unstable nuclei. On the other hand, advanced theoretical approaches would complement experimental data and enable extrapolation of our knowledge to the very short-lived exotic nuclei, where experimental information is mostly absent.

The nuclear level density is defined as the number of excited levels ΔN with a given spin and parity J^π per energy bin ΔE, or $\rho(E, J, \pi) = \Delta N(E, J, \pi)/\Delta E$. The total level density should not be confused with the state density $\rho_{st}(E)$, taking into account all available magnetic substates for the spins J as [74]:

$$\rho_{st}(E) = \sum_J (2J+1)\rho(E, J). \tag{3.1}$$

The inverse of the level density corresponds to the level spacing parameter $D = 1/\rho$, or the average distance between the states within ΔE; it could serve as a good scale in a given energy region. Indeed, one could compare it with the γ-decay widths Γ of the states. Furthermore, the relation between the lifetime of a state with its width $\tau = \hbar/\Gamma$ links all these terms together so that the whole excitation energy region could be split into three approximate regions. The lowest distinct levels could well characterized by the level spacing parameter being significantly larger than the widths observed, $D \gg \Gamma$. This corresponds to the discrete levels, easily distinguishable in spectroscopic experiments. Further up, towards higher excitation energies, levels would lie closer to each other, and the average distance between them decreases so that $D \geq \Gamma$. This energy region, or so-called quasi-continuum, lies beyond the energies where different levels could be distinguished experimentally, but the levels are still separated. If, thus, one considers the level density extracted from a direct counting of observed levels (conventional low-energy spectroscopy), it would underestimate the true level density, which is rather expected to increase exponentially with excitation energy [75]. For even higher energies, the states begin to overlap

($D \leq \Gamma$), and the continuum region begins. In the present work a relatively wide range of energies up to the neutron separation energy would be studied.

3.1.1 Theoretical approaches to the nuclear level density.

Despite the relative simplicity of the definition, an accurate description of the level density, accounting for different relevant physical phenomena, could be quite challenging. Numerous theoretical approaches were introduced in the attempt to describe the level densities in various nuclei. A seminal work was presented by Bethe in 1936 [76]; he approached the level density calculation statistically by adopting the Fermi gas nuclear model. All A nucleons were assumed to be non-interacting and contained in a box volume defined by a radius R. The level density obtained originally in this approach was written as a function of excitation energy E (with respect to the ground state) [76]:

$$\rho_{FG}(E) = \frac{\sqrt{\pi}2^{1/4}e^{\tilde{a}\sqrt{2E}}}{12\sqrt{\tilde{a}}E^{5/4}} = \frac{\sqrt{\pi}e^{2\sqrt{aE}}}{12a^{1/4}E^{5/4}}, \tag{3.2}$$

where $\tilde{a} = \pi\sqrt{A/2\langle E_f\rangle}$ and $\langle E_f\rangle = (3^{4/3}\pi^{2/3}/8)(\hbar^2 A^{2/3}/MR^2)$ is the average Fermi energy for protons and neutrons. Due to the independence of nucleons in the Fermi gas level density expression, it is impossible to explain systematic deviations in level densities for adjacent odd-odd, odd and even-even nuclei. This effect is primarily due the pairing force between nucleons resulting in the formation of Cooper pairs of nucleons. As all nucleons would be coupled for even-even nuclei, they would form more bound nuclear configurations. The Bardeen-Cooper-Schrieffer theory predicts the excitation energy of the states with two decoupled nucleons to be defined by pairing gaps 2Δ [77]. This value could be formally considered to be an average energy needed to decouple two nucleons in a pair. To account for these pairing effects, it was proposed to shift the excitation energy by pairing energies for protons and neutrons Δ_{pair} defined by $\Delta_p + \Delta_n$ in even-even, $\Delta_{p,n}$ in odd, and 0 in odd-odd nuclei [78, 79]. This gave rise to the conventional shifted Fermi gas (FG) model , where the excitation energy is substituted with:

$$U = E - \Delta_{pair}. \tag{3.3}$$

This shift was subsequently revised, and it was suggested to back-shift the excitation energy [80], introducing $U = E - E_1$ with the energy back-shift parameter E_1 and treat both $\tilde{a}$ and E_1 as free parameters, adjustable to available experimental data. This form of the level density formula is considered in the present work in the following form (BSFG)[81]:

$$\rho_{BSFG}(E) = \frac{e^{2\sqrt{aU}}}{12\sqrt{2}\sigma a^{1/4}U^{5/4}}. \tag{3.4}$$

Here, a is the level density parameter and σ is the model-dependent spin-cutoff parameter. In the BSFG approach, provided by [82], the spin-cutoff parameter is related to the sum of single-particle level spacings for protons and neutrons, denoted by g, and the mean-square magnetic quantum number (angular momentum projections) for these single-particle states $\langle m^2\rangle$:

$$\sigma = g\langle m^2\rangle T. \tag{3.5}$$

This formula involves an explicit thermodynamic parameter: the temperature of the nucleus, T. Equation 3.5 could be further modified by relating the mean-square angular momentum projections $\langle m^2\rangle$ and the moment of inertia $\Theta = g\langle m^2\rangle$:

$$\sigma = \Theta T. \tag{3.6}$$

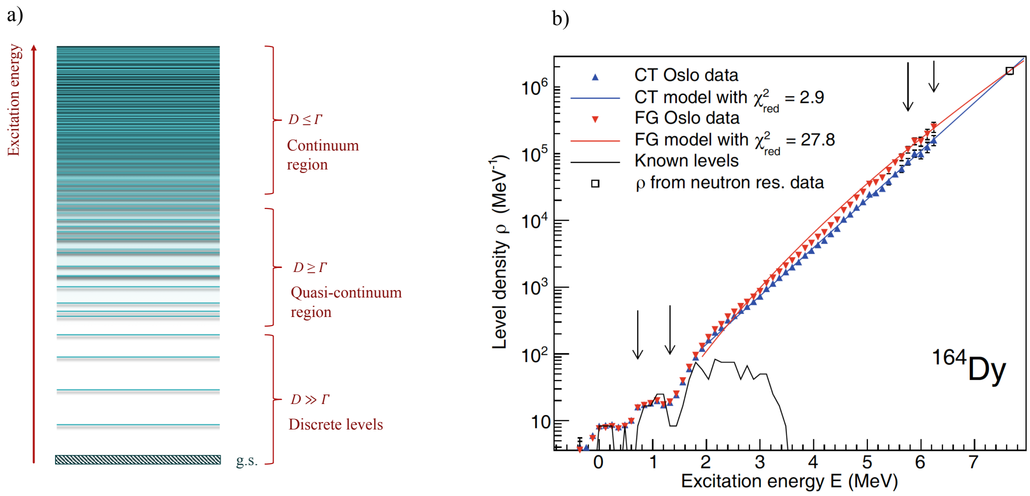

Figure 3.1: a). Schematic representation of a level scheme of an arbitrary nucleus, red arrow denotes the increasing excitation energy. Energy regions for the discrete levels, quasi-continuum, and continuum are marked by thedifferent relation between the width Γ and level spacing D. **b)**. Experimental level densities of ^{164}Dy compared with the constant-temperature (denoted by CT) and the Fermi gas (denoted by FG) level density models. For both cases the reduced least-χ^2 fit is presented.The best fit is achieved for the CT model. Figures are taken from Ref. [75].

This form of the spin-cutoff parameter allows to account for the enhancements of the level density due to collective states, which were disregarded by the conventional FG model. Furthermore, the level density parameter a could incorporate shell effects, while effects due to nucleon pairing and collective effects, missing in the conventional FG model, are often introduced in the E_1 parameter.

The earliest analyses of experimental data provided a strong indication that the cumulative number of levels for excitation energies up to 10 MeV tends to behave as $N(E) = e^{\frac{E-E_0}{T}}$.The level density would be then characterized by the constant temperature formula as [83]:

$$\rho_{CT}(E) = \frac{N(E)}{T} = \frac{e^{\frac{E-E_0}{T}}}{T}. \tag{3.7}$$

This forms the core of the constant temperature model (CT) proposed by T. Ericson in 1959 [83] and used by A. Gilbert and A.G.W. Cameron in 1965 [82]. Here, both the energy shift E_0 and temperature should also be treated as adjustable parameters. It was emphasized in [82] that this model could serve as a good substitution for the BSFG approach for the lower energy region (see Figure 3.1). More precisely, the constant temperature region could be assumed to cover the energies above $\approx 2\Delta$ and up to the neutron separation energy S_n. This statement has a descriptive thermodynamic explanation behind [83]: as in a phase transition, where the temperature holds constant as a medium transforms into another phase, the nuclear temperature could be assumed to be constant when the pair breaking takes place. If excitation energy exceeds 2Δ a first pair could be broken. Practically, the pair breaking process could continue up to even higher energies, so that the constant temperature formula for the level density could be applied for higher excitation energies. Further, as the energy increases and all pairs are broken, the temperature would inevitably begin to increase, the constant temperature formula could no longer be applicable, and the BSFG model could be again introduced.

Further development of the theory behind the expressions for the level density was directed towards the microscopic interpretation of the energy shift and shell effects incorporated in the level density parameter. Ideally, it should combine both the shell-driven behavior of single-particle states and the collective motion of nucleons. The latter were effectively accounted for by introducing the more realistic super-conductive pairing correlations using the BCS framework in the Generalized Superfluid Model (GSM) [84]. Here, a critical temperature is introduced: it indicates a transition between a super-fluid and normal state of a nucleus. Right above the critical temperature, the BSFG model is used with an energy shift, dependent on the correlation function. The region below the critical temperature could be described with more convoluted expressions (see [85] and references therein). Similarly to other semi-phenomenological models, such as the CT and the BSFG, the GSM implies again a large set of parameters to be adjusted to achieve a better fit to experimental systematics.

An alternative way of approaching the nuclear level density implies calculations on the single-particle levels using realistic effective potentials, providing the statistical microscopic description of the level density. This picture should ideally enable an accurate and reliable calculation of the level density up to the high excitation energies and for exotic nuclei where no experimental information is present. Such calculations have been performed with the statistical approach based on the Hartree-Fock-BCS (HFBCS) ground state properties, including a proper treatment of both the single-particle level scheme and the pairing force [86]. On the other hand, the combinatorial approach [87] was also developed to partially eliminate the drawbacks of the HFBCS: the parity dependence of the level density could be obtained, and the non-statistical limit for the level density itself could be evaluated. This approach could be further combined with the mean field Hartree-Fock-Bogolubov model [88]. In addition, numerous applications of the shell model Monte Carlo approach were shown to be in a good agreement with experimental data [89].

Despite the large variety of microscopic models available, the simplicity of the BSFG and CT models makes them considerably more attractive, especially for the interpretation of experimental data close the the valley of stability, where these semi-empirical models are quite reliable and could be based on the parameters, extracted from a global fit to available experimental data. In the present work, the analysis is performed with a specific focus on these two models.

3.1.2 Experimental extraction of the level density.

The phenomenological BSFG and CT approaches require a relevant fit to experimental data, and there are several experimental techniques yielding this information. It has already been mentioned that the level density could be extracted in spectroscopic studies, allowing to obtain the levels with assigned spins and parities [90]. The major drawback of this technique is the low energy region limitation: the unique spin-parity attribution can not be obtained for the higher energies, and the decreasing level spacing prevents levels to be resolved experimentally. This technique often implies various probes (*e.g.* (p,p′),(e,e′), (α',α'), (^{3}He,^{3}He′), (t,p) for ^{124}Sn) with the recoil particles studied in the small angles with respect to the beam line.

Neutron resonance counting is another technique the majority of data compilations (*e.g.* [91]) are based on. If the neutron energies are low, their angular momentum is $l = 0$, and so-called s-wave capture takes place. The spin window excited in these reactions is rather narrow and limited by the levels with $I_t \pm 1/2$ and the same parity as the ground state of a target nucleus with spin I_t. This allows several levels to be observed in a form of resonances in the vicinity of the neutron binding energy, where nuclear levels are strongly overlapped. Despite that this does not yield the total level density, it could be further extracted on the base of a known parity ratio and a spin distribution, if these quantities are known. As the neutron energy increases, the p-wave resonances could also be populated providing information of the parity ratio [74].

Nuclear level densities have also been obtained in particle evaporation experiments (e.g. [92])

with protons, neutrons or α particles measured in backward angles to suppress the contribution from direct reactions. Another technique involves observation of so-called Ericson fluctuations in a compound nucleus cross-section. These fluctuations arise from the interference of overlapping states and could be used to extract information on the level densities in a region of several MeV above the binding energy [83]. As the level density increases, the fluctuations tend to decrease, making all the information extracted no longer reliable. In addition, the fluctuation analysis of high-resolution data on electric and magnetic resonances was shown to yield spin and parity defined level densities [93].

Another effective technique aiming at extracting the level densities is based on the Oslo method applied to particle-γ coincidence data measured at the Oslo Cyclotron Laboratory (see Chapter 5 for further details); it was shown to be applicable to a large variety of nuclei to extract not only the nuclear level densities, but the γ-ray strength functions. However, this methodology is model dependent. Simultaneous extraction of these characteristics involves numerous assumptions to be adopted. In addition, the discrete known levels and the level density at the binding energy are needed to estimate an absolute value of the level density and trend towards the neutron separation energy.

3.2 The γ-ray strength function

By analogy with the nuclear level density, introduced to avoid practically impossible consideration of separate nuclear levels, it is often useful to introduce the γ-ray strength function, another average property used to simplify treatment of individual transition probabilities. In order to understand the physics behind this function, one should first consider a γ-transition between an initial state i with spin J and its z-projection m on the symmetry axis and a final state f with spin J' and the corresponding projection m'. The transition probability is directly related to the corresponding matrix element of the electromagnetic perturbation operator $\hat{H}$ coupling the wave functions of the initial ψ_i and final state ψ_f. If the transition is via a photon carrying L units of angular momentum with a projection M, the transition probability could be expressed in terms of the partial radiative amplitude, or width [94]:

$$\Gamma_{\gamma LM}^{i\to f} = \frac{8\pi k_\gamma^{2L+1}(L+1)}{L((2L+1)!!)^2} |\langle \psi_{fJ'm'}|\hat{H}_{TM}^{L}|\psi_{iJm}\rangle|^2, \tag{3.8}$$

where $k_\gamma = \omega_\gamma/c = E_\gamma/\hbar c$. Further averaging of the radiative width with respect to all J projections $m = -J, -J+1, ..., J$ and summing over all J' projections yields:

$$\Gamma_{\gamma L}^{i\to f} = \frac{\sum_{Mmm'} \Gamma_{i(\gamma LM)}}{2J+1} = \frac{8\pi k_\gamma^{2L+1}(L+1)}{L(2J+1)((2L+1)!!)^2} |\langle \psi_{fJ'}||\hat{H}_{T}^{L}||\psi_{iJ}\rangle|^2. \tag{3.9}$$

It was emphasized by J. M. Blatt and V. F. Weisskopf in 1952 [95], that the squared transition matrix element, mentioned above, is proportional to the level spacing parameter D_i for the initial states with the same spin and parity. Hence, the squared matrix element is inversely proportional to the corresponding level density $\rho_i = 1/D_i$. One could combine the level density and radiative width to describe γ-transitions in the continuum region by the γ-ray strength function [96]:

$$f_{\sigma L}^{i\to f}(E_\gamma) = \frac{\langle \Gamma_{\gamma\sigma L}^{i\to f}\rangle}{E_\gamma^{2L+1}} \rho_i(E_i, J, \pi). \tag{3.10}$$

Here, the partial width is averaged over the initial states of a given spin and parity J^π within a chosen energy bin E_i, energy of a γ-transition E_γ is directly related to the initial E_i and final

E_f energy bins, and the indexes σL denote the multipole type - E for electric, M for magnetic transitions with multripolarity L. From now on the upper index $i \to f$ will be omitted.

Another useful characteristic of the γ-emission channel could be related to the γ-ray function definition: the γ-ray transmission coefficient $\mathscr{T}_{XL}(E_\gamma)$ [85]:

$$\mathscr{T}(E_\gamma) = 2\pi E_\gamma^{2L+1} f_{XL}(E_\gamma). \tag{3.11}$$

Both the level density and transmission coefficient (and, thus, the γ-strength function respectively) are two of the major outputs resulting from the Oslo method. In addition, they are two key ingredients of the Hauser-Feshbach theory applied to neutron capture cross-section calculations [97].The transmission coefficients could be used to infer information on the competition between γ-decay and particle emissions. The definition of the γ-strength function, introduced above, is originally referred to the γ-emission, i.e. γ-decay of an initial state (states within a given bin) to a set of final states. This is often denoted by the downward γ-strength function, or $f_{\sigma L}^{down}$. On the other hand, the upward γ-strength could be extracted in the opposite, absorption process as [85]:

$$f_{\sigma L}^{up}(E_\gamma) = \frac{\langle \sigma_{\sigma L}(E_\gamma) \rangle}{(2L+1)(\pi\hbar c)^2 E_\gamma^{(2L-1)}}, \tag{3.12}$$

where $\langle \sigma_{\sigma L}(E_\gamma) \rangle$ is the absorption cross-section, averaged over the initial states and summed over all possible final states. If the same initial and final states are involved both in γ-absorption and emission processes, the principle of detailed balance and the Fermi's Golden Rule (see section 5.3 for further details) predict that the upward and downward strengths should be essentially the same.

3.2.1 Theoretical description of the γ-strength function

A pioneering attempt to describe the γ-strength function was proposed by Blatt and Weisskopf simultaneously with introduction of the model independent definition, given by Equation 3.10 [95]. It was based on the single-particle approach and assumed that a nucleus is an exceptionally convoluted system, for which the reduced widths are distributed randomly. This assumption led to an energy independent γ-strength function. Later, this approach was shown to be oversimplified: a certain degree of randomness for widths could be taken into account for the limited energy ranges only. First observations of the IVGDR implied that the collectivity of a nucleon motion could not be omitted. Further attempts to reproduce the IVGDR and the Brink-Axel hypothesis, assuming independence of the detailed structure of the photoabsorption cross section on the properties of the initial state (see section 3.3), led to the Standard Lorentzian (SLO) form of the strength [85]:

$$f_{E1}(E_\gamma)^{SLO} = \frac{1}{3\pi^2\hbar^2c^2} \frac{\sigma_0 \Gamma_0^2 E_\gamma}{(E_\gamma^2 - E_0^2)^2 + \Gamma_0^2 E_\gamma^2}. \tag{3.13}$$

Here, σ_0 is the cross-section at maximum, Γ_0 and E_0 are the width and centroid of the resonance. It is a common practice to approximate the most prominent response feature with the SLO function, e.g. the PDR and the GMDR could be fitted with the SLO. This is still one of the simplest and widely used approaches to describe the strengths in vicinity of a resonance maximum for a wide variety of nuclei, except for the light ones. The major drawback is an overestimation of experimental data and a significant underestimation of the strength in the very-low energy region.

An alternative approach to deduce an expression for the strength is based on the theory of Fermi liquids; the width of the IVGDR is energy and temperature dependent and could be written for the final states as [85]:

$$\Gamma(E_\gamma, T_f)^{KMF} = \frac{\Gamma_0}{E_0^2}(E_\gamma^2 + 4\pi^2 T_f^2), \tag{3.14}$$

where the first term in the formula takes into account spreading of particle-hole configurations over more complicated ones, and the temperature-dependent term includes collisions of quasi-particles. This forms the core of the Kadmenskij, Markushev and Furman (KMF) model of the IVGDR strength [98]:

$$f_{E1}^{KMF}(E_\gamma, T_f) = \frac{1}{3\pi^2\hbar^2c^2}\frac{0.7\sigma_0\Gamma_0^2(E_\gamma^2 + 4\pi^2T_f^2)}{E_0(E_\gamma^2 - E_0^2)^2}. \tag{3.15}$$

Except for the divergence at $E_\gamma = E_0$, this model partially eliminates the disagreement between the model predictions and experimental cross-sections and widths. The idea of the temperature dependence introduced in this model was further exploited by J. Kopecky and R.E.Chrien to form the Generalized Lorentzian model (GLO), combining the SLO and KMF approaches [99]:

$$f_{E1}^{GLO}(E_\gamma, T_f) = \frac{\sigma_0\Gamma_0}{3\pi^2\hbar^2c^2}\left[E_\gamma\frac{\Gamma_{KMF}(E_\gamma, T_f)}{(E_\gamma^2 - E_0^2)^2 + E_\gamma^2\Gamma_{KMF}^2(E_\gamma, T_f)} + \frac{0.7\Gamma_{KMF}(E_\gamma, T_f)}{E_0^3}\right]. \tag{3.16}$$

The last term provides a non-zero limit for the strength at $E_\gamma \to 0$. This model was shown to give a reasonable description of capture cross-sections and emitted γ-spectra for spherical nuclei [100]. In order to account for the deformation, causing a splitting of the IVGDR into two components, the KMF width is modified in the following manner [85]:

$$\Gamma(E_\gamma, T_f)^{EGLO} = \left(\kappa + (1-\kappa)\frac{E_\gamma - \epsilon_0}{E_0 - \epsilon_0}\right)\frac{\Gamma_0}{E_0^2}(E_\gamma^2 + 4\pi^2T_f^2) \tag{3.17}$$

with a level-density dependent factor κ and constant energy shift ϵ_0; this extended form of the strength is often referred to as the Enhanced Generalized Lorentzian model.

The dominant electric dipole, electric quadrupole and magnetic dipole modes (E1, E2, M1) observed in the experiments could be well described by the simplest SLO form. Both the SLO and GLO are widely applicable (especially the SLO, which does not include the model dependent κ parameter). Further modifications of the width to take one-body effects (fragmentation) into account (*e.g.* see [101]) led to further improved forms of the SLO with an additional enhancement factor: the Modified Lorentzian (MLO) [102], and the specific quasi-particle interaction coefficients included in the Generalized Fermi Liquid (GFL) approach [103].

An alternative way of approaching the description of the γ-ray strength function could be carried out by microscopic calculations in the framework of the RPA. Such calculations are essential for understanding the underlying microscopic structure and the way collective effects could be described in terms of particle (quasi-particle) excitations; the ability of these model to deepen our understanding on the γ-strength function is of particular interest. Numerous HFB+QRPA calculations were performed with both the zero-range Skyrme [104] and finite-range Gogny forces [105]; these microscopic calculations were confirmed to give reasonable predictions as compared to the experimental photoabsorption cross-sections.

3.2.2 Experimental methods for extracting the γ-strength function

The majority of the experimental benchmarks for the theoretical approaches on the γ-ray strength functions, described above, were historically obtained in the study of photoabsorption cross-sections. In the energy range above the neutron separation energy, for medium and heavy mass nuclei, the proton decay (or α decay) of the IVGDR is still hindered up to high excitation energies. Therefore, if a nucleus absorbs a photon and deexcites via neutron emission, the photoneutron cross-section measured serves as a good estimate for the total photonuclear absorption cross-section. Such experiments could be performed with bremsstrahlung photons (e.g.[106], here the bremsstrahlung spectra should be taken into account) produced by stopping accelerated electrons in a high-Z material; the quasi-monoenergetic photon beams are also quite common for this type of experiments [107]. They could be produced with tagged bremsstrahlung, in-flight positron annihilation, or in the deexcitation process after a proton or neutron absorption. In addition, laser photons could be scattered from relativistic electrons; in this case the inverse Compton scattering takes place, and a beam of close-to monoenergetic photons could be obtained [108]. However, the mentioned experiments do not allow to investigate the strength below the neutron separation energy and are limited to long-lived states (ground states and some isomeric states) of the target nuclei.

Another widely used technique is presented by the NRF, which enables a study in the region below the neutron separation energy. In this case, the nucleus is first excited with a photon beam (resonant excitation), and the subsequent γ-rays emitted are registered by high-purity germanium or scintillator detectors. These experiments provide an efficient model-independent way to detect low-lying dipole excitations in the strength distribution (the PDR and scissors-mode [109]). However, the photon probe is highly selective, and some especially weak transitions can be missing while determining the γ-strength function. On the other hand, the analysis of the resulting angular distribution of γ-rays facilitates separation of different modes, E1, M1, and E2. A similar separation could be performed with radiative particle capture (usually proton or neutron). In this case, the γ-ray spectrum stemming from a compound nucleus decay is studied; this method is able to yield both the individual strengths and the average radiative widths [110]. However, it could be applicable only in a limited energy range below the neutron separation energy.

Alternatively, the γ-strength function could be extracted in different types of radiative neutron (or proton) capture experiments, where the two-step cascade, relating the states of a compound nucleus with a final state, is detected. Fitting the experimental spectrum would depend on the level density and γ-strength function of the final nucleus, so trial functions could be used to fit the experimental spectrum (e.g. see [111]). The main source of uncertainty in this case is the strong model dependence for the level density, which is impossible to avoid.

Finally, the Oslo method (for a detailed method description see Chapter 5) yields both the γ-strength function below the neutron separation energy and the level density of the studied nucleus. An overall good agreement with the results, obtained with completely different experimental techniques and analyses, might argue in favor of the Oslo method. However, it is based on several assumptions, discussed in Chapter 5 and requires additional experimental parameters, constrained in different experiments, in order to perform the normalization of the resulting γ-ray strength function.

3.3 A note on the Brink-Axel hypothesis

The Brink-Axel hypothesis, mentioned in the previous section, forms the core assumption for the procedure of simultaneous extraction of the nuclear level density and γ-ray strength function from a particle-γ coincidence spectrum in the Oslo method. Originally, this hypothesis was introduced by D. M. Brink in his doctoral thesis at the Oxford University in 1955 [112]; the primary idea of this hypothesis implied an independence of the photoabsorption cross-section in the IVGDR energy range on the detailed structure of the initial state, so that the IVGDR built on the ground state is approximately the same as the IVGDR built on an excited state. According to the original formulation, the photo-effect performed on an excited state yields the same Lorentzian energy dependence of the cross-section, as for the one performed on the ground state. This assumption was shown to hold in a relatively wide energy range within $\approx 10-20$ MeV [1, 113]. Moreover, it was extended by P. Axel to describe emission and absorption of photons between two resonant states in the framework of detailed balance [114]. The so-called generalized Brink-Axel hypothesis in the form it is applied in the Oslo method analysis includes also an independence from spins of initial and final states (with the exception of selection rules for the dipole transitions).

This hypothesis appears to be crucial for the statistical treatment of γ-transition probabilities in terms of the γ-ray strength function. Being combined with the statistical model, it might be exploited for the calculation of stellar reaction rates (*e.g.* for the slow and rapid neutron capture processes). Finally, the validity of this hypothesis might allow a significant simplification of calculations. For example, the Oslo method implies the Brink-Axel hypothesis to be valid in order to provide the decomposition of the processed coincidence matrix into the nuclear level density and γ-ray strength function.

The OCL experiments are majorly limited by the neutron separation energy, whilst the validity of the Brink-Axel hypothesis for this comparatively low energy range poses a complex question to be disclosed by various theoretical and experimental approaches. The detailed study of the γ-ray strength function for ^{238}Np, extracted in the ^{237}Np(d,pγ)^{238}Np reaction by means of the Oslo method, was performed for different initial and final excitation energies [115]. The results revealed a clear independence of the resulting γ-ray strength functions from these energies and spins of initial and final states, implying that the Brink-Axel hypothesis holds not only for a giant resonance structure, but for the strength below the neutron separation energy as well (see Figure 3.2). Subsequent tests for lighter isotopes, performed by the Oslo group, revealed different results: for example, the cases of ^{92}Zr [116] and ^{64,65}Ni [117] demonstrated certain fluctuations of the γ-ray strength functions for different initial states with respect to the functions obtained with the standard Oslo method. This effect is also especially strong for the strengths feeding the ground state and the first excited state in ^{64,65}Ni. The latter were principally explained by the Porter-Thomas fluctuations, or fluctuations of individual radiation widths due to particular properties of the states involved in the transitions to or from these states [118]. In addition, a certain admixture of quadrupole transitions could not be excluded completely

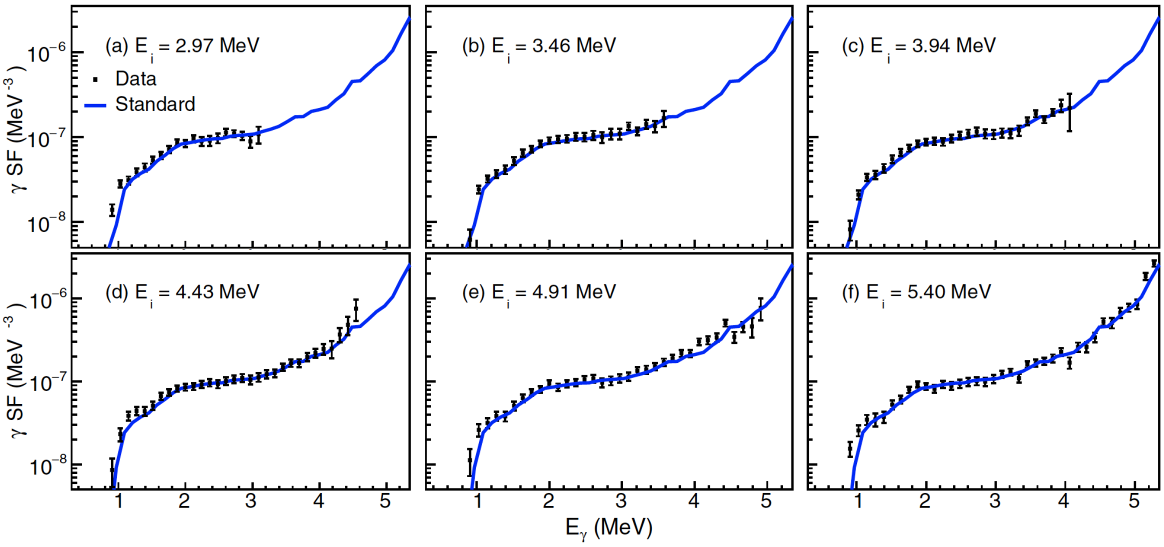

Figure 3.2: The γ-ray strength functions for different initial excitation energies. Blue line denotes the γ-ray strength function fron the standard Oslo method. Figure is taken from ref. [115].

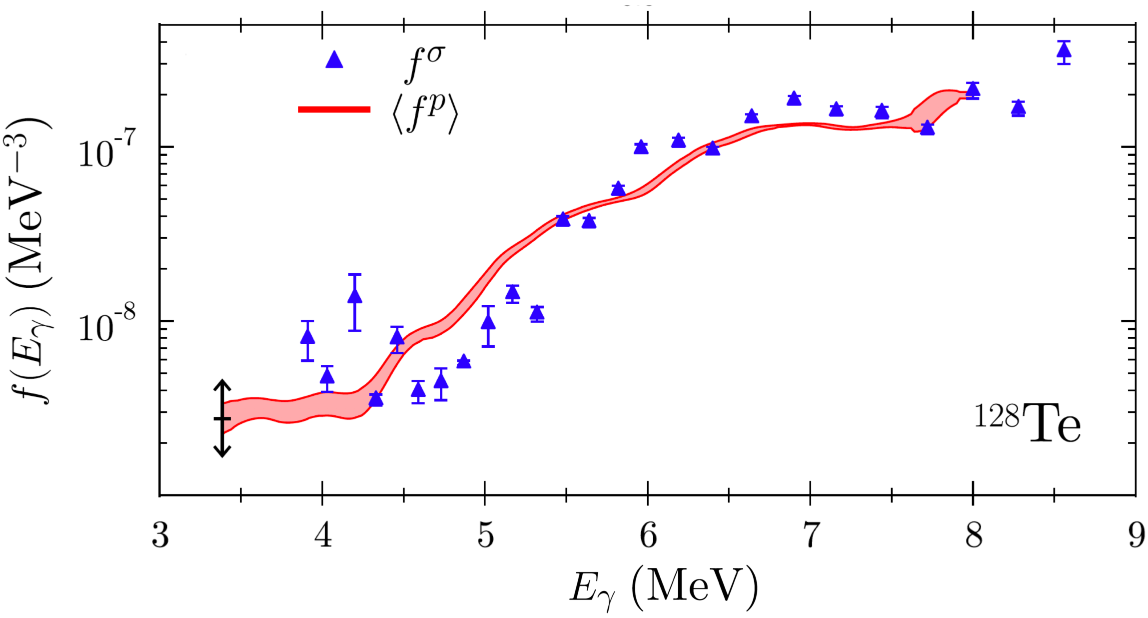

Figure 3.3: Comparison of the γ-ray strength functions, extracted from the photoabsorbtion cross-section f^{σ} (blue markers) and the strength, extracted from the observed primary transitions $\langle f^{p} \rangle$. Figure is taken from ref. [119].

from the analysis. Despite these deviations, the strengths obtained are still fluctuating with respect to a certain averaged strength, thus, supporting the Brink-Axel hypothesis. In contrary, the experimental technique presented by J.Isaak *et.al.* in [119], which does not primarily rely on the Brink-Axel hypothesis, demonstrated a significant discrepancy between the upward and downward γ-ray strength functions below the neutron separation energy in ^{128}Te (see Figure 3.3). The strength extracted from the photoabsorbtion cross-section for the incoming quasi-monochromatic photon beam, was found to be deviating from the strength function extracted from the average decay intensities for transitions between initial excited states to lower-lying states. Such large deviations could be explained by neither statistical uncertainties, nor Porter-Thomas fluctuations solely, indicating a breakdown of the hypothesis for the low-energy range in the studied nucleus.

All these controversial studies put a certain limitation on the validity of the results presented in this thesis. Since the Brink-Axel hypothesis is assumed to be valid for the Oslo method to be used to extract the γ-ray strength functions and level densities, it is crucial to perform an additional study of the strength as a function of initial and final energy to test this assumption. This test will be presented in Chapter 7 together with other obtained results.

Chapter 4

The experiment, data calibration and primary analysis

The present thesis is mainly devoted to the analysis of the ^{124}Sn(p,p$'\gamma$)^{124}Sn experiment carried out in February-March 2019 at the Oslo Cyclotron Laboratory. The following chapter presents the description of the experimental setup and relevant conditions this experiment was performed in. Sections 4.1.1 and 4.1.2 describe two detecting systems, the SiRi particle telescope and the OSCAR scintillator array. One of the first steps of the analysis involves calibration of all detectors in the setup, this process is outlined in Sections 4.2.1 and 4.2.3 in detail. Finally, the data selection and extraction of the raw proton-γ coincidence matrix will be presented in Sections 4.2.2, 4.2.4, and 4.2.5. This matrix serves as the main input for further steps of the analysis aiming at extraction of the γ-ray strength function and nuclear level density. These final steps and relevant details could be found in the next Chapter 5.

4.1 The experimental setup at the OCL

The experimental study presented in this thesis was performed at the OCL at the University of Oslo [120]. The technical core of the laboratory is presented by the MC-35 Scanditronix cyclotron, the first and one of a few research accelerators in Norway. The cyclotron is set to exploit pulsed ion beams (*e.g.* p, d, ^{3}He, ^{4}He) with energy ranging up to 35 MeV in the case of protons. The OCL has been involved in a wide range of research areas and applications of accelerated particle beams, such as nuclear physics, nuclear chemistry, hardness tests of electronics, and nuclear medicine. The latter application, namely the production of medical isotopes (e.g. ^{18}F, ^{211}At, ^{205}Bi) and proton irradiation of cancer cells, is chiefly driven by the intensively expanding role of nuclear medicine and urge for a basic research in this field. However, the major research at the OCL is still focused on the study of nuclear structure and dynamics, related to extracting and analyzing level densities and γ-ray strength functions. The results obtained are essential for better understanding of fundamental electromagnetic and thermodynamic properties of nuclei, estimation of various reaction rates, and behavior of nuclear matter in a stellar environment.

The OCL is separated into several principal compartments, such as the cyclotron vault, the experimental hall and the control room (the scheme is presented in Figure 4.1). The cyclotron accelerates light ions from a source, forming a pulsed beam shaped and focused by series of dipole (D$_1$,..., D$_3$) and quadrupole (Q$_1$) magnets as well as additional slits throughout the beam line from the cyclotron to the experimental hall. Being bent by the analyzing magnet by 90° with respect to the initial beam line, charged particles are directed to the experimental hall. After an additional shaping and focusing (Q$_2$, Q$_3$, D$_4$), particles enter a target chamber surrounded

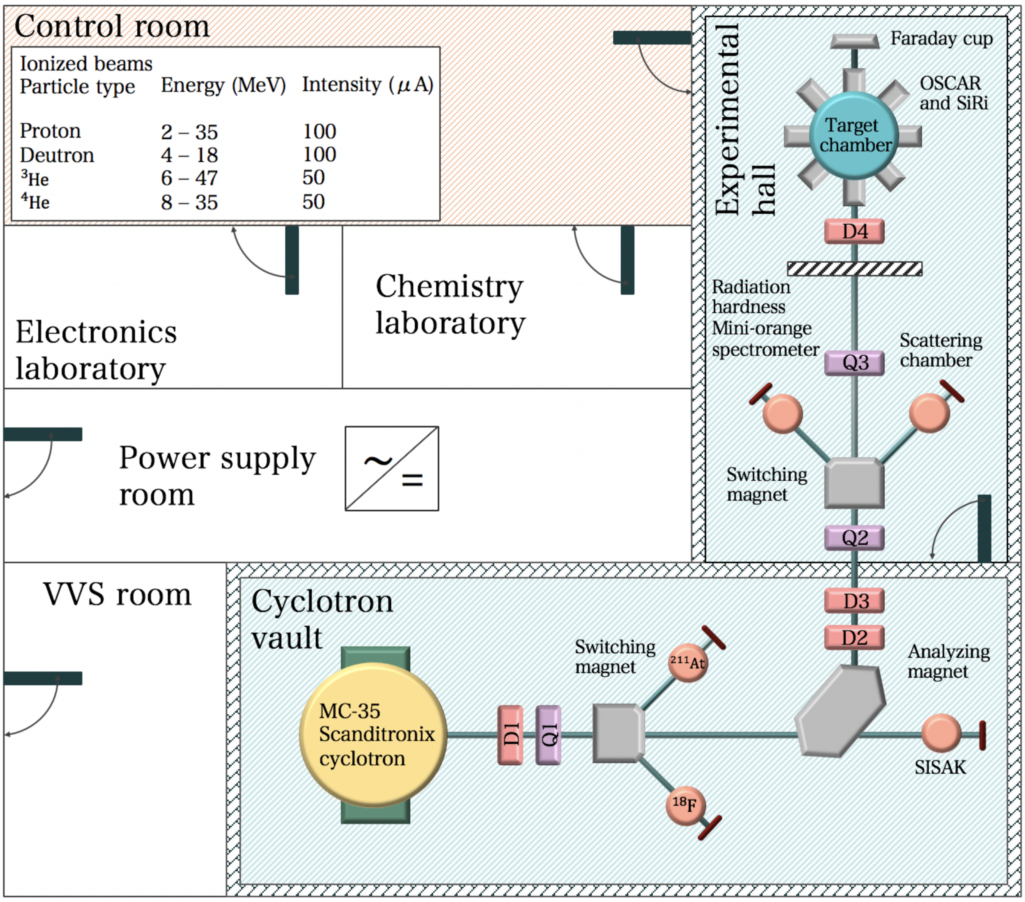

Ionized beams

Particle type	Energy (MeV)	Intensity (μA)
Proton	2 – 35	100
Deutron	4 – 18	100
^{3}He	6 – 47	50
^{4}He	8 – 35	50

Figure 4.1: Scheme of the Oslo Cyclotron Laboratory: the cyclotron vault, the experimental hall and the control room are marked with grey color. The beam types and typical energies used in the OCL experiments are listed in the upper right corner. The figure is inspired by [120].

by the LaBr$_3$:Ce OSCAR scintillator array and the silicon particle telescope SiRi placed in the forward or backward position (see Figure 4.1, upper right corner) and, finally, hit a target set in the center of the chamber. In addition, two sets of switching magnets are used to direct the initial beam to other compartments for different, medicine related experiments. All types of particles, corresponding maximum energies and beam intensities are listed in the upper left table in Figure 4.1.

4.1.1 The SiRi particle telescope

The facility at the OCL was mainly set for the implementation of the Oslo method, aiming at the simultaneous extraction of level densities and γ-ray strength functions from particle-γ coincidence events. Both the particle telescope and photon detection system are incorporated in the experimental setup. The SiRi particle telescope, mounted in the target chamber, exploits efficiently the $E - \Delta E$ type of detecting technique which allows different reaction channels to be discriminated. For each particle event the corresponding energies and arrival times are recorded. This information is subsequently used to reconstruct information on excitation energies recoil nuclei were produced with in a certain reaction.

SiRi comprises of two types of silicon detectors – the thin ΔE detectors with thickness of 130 μm and the 1550 μm thick E detector [121]. As typical semiconductors, they exploit the following principle: an ionizing radiation (in our case protons, deuterons, tritons, α, etc) hits the semiconductor area of a detector, causing series of atomic ionizations on its way. As a certain voltage is applied to this area, all liberated charge carriers could be collected [122]. If a particle is stopped within the detection area, the charge collected produces a signal proportional to energy of the particle entering the detector. The thicknesses of both E and ΔE flat silicon wafers are optimized for the beam energies achievable at the cyclotron and voltage supplies used. In addition, a 10.5 μm thick aluminum foil is placed in front of ΔE detectors to reduce the amount of δ-electrons produced during the passage of incident ions through the target matter. Since the silicon detectors require depletion for an efficient operation, high depletion voltage (< 300 V) is applied and moderated by 18 guard rings covering the edges of active areas in all detector segments.

An accurate measurement of excitation energy implies knowledge on both energetic characteristics (beam energy, Q-value of the reaction, energy of an outgoing light ion) and angular distribution of light ions. This determines the design of the detector; SiRi detectors are presented in form of modules (8 modules of E detectors mounted right behind 8 modules of ΔE detectors) of trapezoidal shape. All the modules are grouped in an approximate ring in the way that each module is located in 5 cm distance from a chosen target. In order to distinguish different scattering angles, the ΔE detectors are also segmented into 8 curved pads (see Figure 4.2 b)). The corresponding segmentation of E detectors was omitted to minimize misalignment of E and ΔE detectors [121]. Each pad corresponds to 2° of scattering angle and approximately 1.7 mm thickness. The total segment of scattering angles, covered by SiRi is optimized to reduce significant pile-up of events for small scattering angles in forward position and covers $\theta^{for} = 47^\circ \pm 7^\circ$ (with respect to the beam line) in forward angles and, therefore, $\theta^{back} = 133^\circ \pm 7^\circ$ in backward angles. The typical uncertainty for the angle estimation is $\pm 1^\circ$[121].

The $\Delta E - E$ technique implemented in SiRi is based on the energy loss mechanism for charged particles. Considering the energy loss per unit path length (stopping power) for ions moving with velocities and energies larger than typical velocities and energies of orbital electrons, the Bethe-Bloch formula can be applied [122–124]:

$$\frac{dE}{dx} = 2\pi N_a r_e^2 m_e c^2 \rho \frac{Z}{A}\frac{z^2}{\beta^2}\left[\ln\left(\frac{2m_e\gamma^2 v^2 W_{max}}{I^2}\right) - 2\beta + \delta - 2\frac{C}{Z}\right] \tag{4.1}$$

where the parameters could be written as [122]:

A – atomic weight of absorber
Z – atomic number of absorber
N_a – Avogadro's constant
m_e – electron mass
r_e – classical electron radius
I – mean excitation potential
W_{max} – maximum energy transfer per collision
ρ – density of absorber
z – charge of an incident particle
β – v/c
γ – Lorentz factor $1/\sqrt{1-\beta^2}$
δ – density correction
C – shell correction

For comparatively low energies of incident particles (the logarithmic rise is negligible) the stopping-power reveals the following dependency on particle's energy:

$$\Delta E = \left|-\frac{dE}{dx}\right| \sim \frac{z^2}{\beta^2} \sim \frac{mz^2}{E}, \tag{4.2}$$

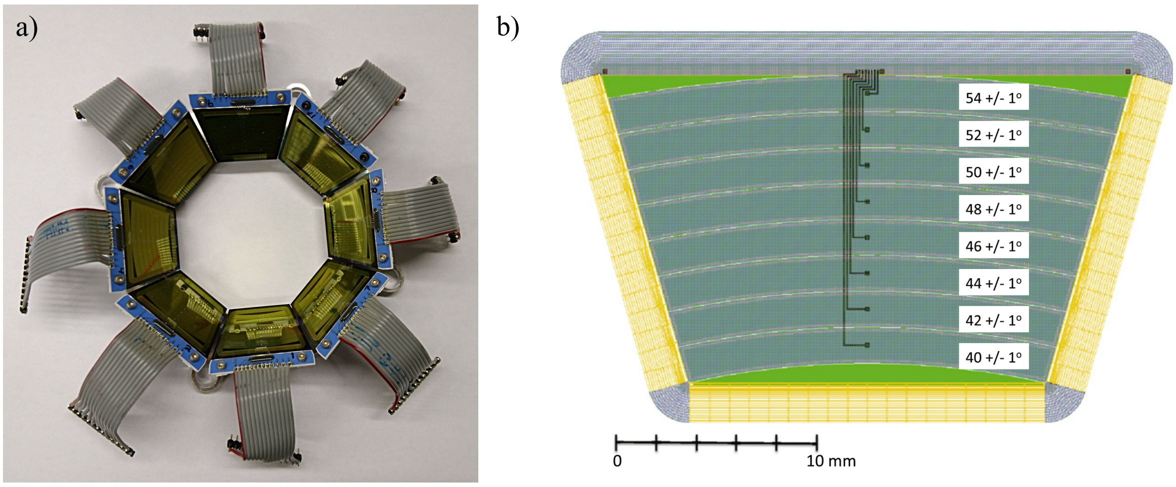

Figure 4.2: **a)** The SiRi particle telescope at the Oslo Cyclotron Laboratory for the energy measurement of charged particles, produced in kinematically allowed channels. **b)** Illustration of a frontal ΔE detector, segmented into 8 curved pads, covering different scattering angles (provided for the forward position. Figure is taken from M. Guttormsen *et al.* [121].

where m is the mass of a detected particle. This underlies the principal idea of operation implemented in $\Delta E - E$ telescopes, consisting of two detecting layers: this allows ions to lose a certain amount of energy and pass through a thin silicon detector and to be subsequently stopped in a thicker detector, providing information on the total energy deposited.

It is possible to measure both the energy loss in a thin frontal layer of absorbing material (implemented as ΔE detector) and the rest loss in a thicker E detector mounted behind. The relative dependence of these energy losses would be represented by separated reaction channels ("banana"-like channels, see Figure 4.5). If an incoming beam energy is high enough for particles to pass through the whole set of detectors without being stopped, the punch-through is observed and only a fraction of incident particle energy is measured. Therefore, the first step for planning an experiment implies the check of suitable kinematics, whether a given beam energy and a target composition and thickness would allow the total energy to be deposited in the detector and provide information on energy a light charged particle was scattered or produced with.

According to the Bethe-Bloch relation, the combination of energy deposited in ΔE and E detectors is characteristic for different light ions, produced in a reaction. This fact implies that separate reaction channels could be easily distinguished. The lightest particles (the lowest z and m) deliver the smallest fraction of energy in the first thin detectors and correspondingly the largest fraction in the backside E detector. For the lightest particle, a proton, detected by SiRi in the presented experiment, this is reflected by the lowest position of (p,p′) events in the $E - \Delta E$ plot. Indeed, according to Equation 4.2, for a given energy, deposited to a thick E detector, the lowest energy will be deposited to a ΔE detector by the registered ions with the smallest product mz^2. The successive heavier ions could be found shifted to the higher ΔE with respect to the p-channel. This method allows us to separate particles graphically by putting corresponding gating conditions on the energy spectrum for each combination of $E - \Delta E$ detectors.

4.1.2 OSCAR detector array

The detection of γ-rays and the corresponding energies in the present experiments was carried out by means of the Oslo SCintillator ARray (OSCAR), officially put into operation at the OCL in 2018 (see Figure 4.3 a)). The array consists of 30 large volume cylindrical BriLanCe^{TM} 380 LaBr$_3$:Ce scintillating crystals with a Ce dopant. The cylinders are of 3.5 inches in diameter and

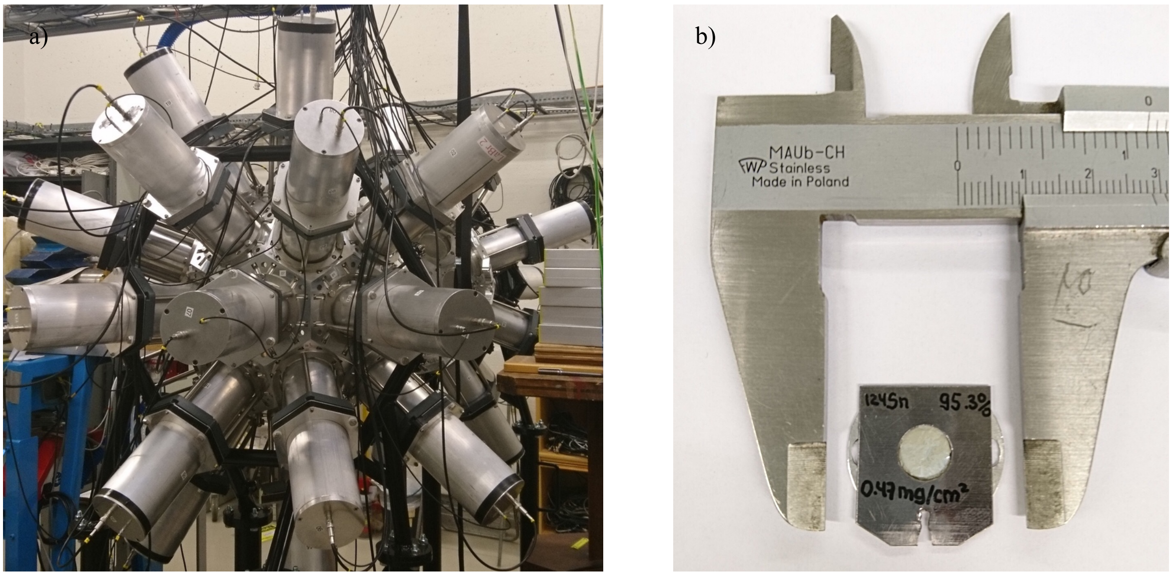

Figure 4.3: **a)** The OSCAR detector array at the Oslo Cyclotron Laboratory for the energy measurement of γ-quanta, produced in all proton-induced reactions. **b)** The ^{124}Sn target used in the ^{124}Sn(p,p'γ) experiment. Both photos were taken directly before the experiment.

8 inches in height each. As scintillator crystals they are able to convert γ-rays hitting the active volume of the detector into photons in the visible range of the spectrum [122]. Incident γ-rays excite atoms of a crystal deexciting subsequently with cascades of visible light photons. The latter are collected by a photocathode coupled to the crystal and undergo transformation into an electric signal for further amplification in a photomultiplier tube. Each crystal of the OSCAR is combined with active voltage dividers (LABRVD) and a specially manufactured Hamamatsu's R10233-100 photomultiplier tube in an aluminum housing [125]. All the detectors are mounted in the icosahedron-shaped frame with the distance from the center adjusted by the distance rods depending on conditions chosen of a current experiment. For the experiment presented in this thesis the distance was set to be 16 cm.

As compared to the CACTUS detecting array with NaI:Tl crystals operating at the OCL before 2018, the newest LaBr$_3$:Ce-based detectors introduced numerous advantages for all ongoing and future experiments. The energy resolution achievable with the new detectors is approximately two times higher than that for the older CACTUS detector: $\approx 2.7 - 4.3\%$ at 662 keV γ-rays measured with analogue electronics for LaBr$_3$:Ce as compared to $\approx 7\%$ for NaI:Tl crystals [126]. The light output achievable with these detectors is high enough ($\approx$63000 photons/MeV) to yield a relatively high counting rate. In addition, the light pulse decay time is comparatively short, thus, OSCAR reveals supreme timing properties (intrinsic time resolution < 1 ns *vs.* ≈ 15 ns in NaI:Tl [127]). The geometrical efficiency was also improved [125]. All these modifications enable large variety of new experiments to be performed at the OCL, and the current experiment is one among the first experiments exploiting the OSCAR detector array.

4.1.3 Electronics and data acquisition

All valuable events occurring within the active volumes of detectors should be read out and processed in a form of electric output. As a particle hits the SiRi detector, charge carriers are collected to form an electric pulse, similarly, visible light photons are transformed into multiplied electric signals from OSCAR. All these signals are passing through the digital pulse processors. At the OCL these digital electronics units have recently substituted older analogue systems, and the present experiment was one of a few first experiments carried out with the new signal processing systems as well.

All the detectors are connected to the Digital Gamma Finders (DGF) manufactured by XIA [128]. Each finder presents a 16-channel digital waveform acquisition and spectrometer 32-bit card of Pixie-16 type, able to combine spectroscopy with digitizing and pulse-shape analysis and supporting coincidence measurements. Each channel is attributed to a separate detector, meaning that there are 64 channels, accepting signals from 64 ΔE detectors, 8 channels corresponding to 8 E detectors, and 30 channels for 30 separate LaBr$_3$:Ce detectors in the OSCAR array. DGFs support different rates of event sampling, and the signals from all ΔE and E are sampled with frequency 250 MSPS (Mega Samples per Second, or MHz), as OSCAR signals are sampled at the increased rate of 500 MSPS. Signals pass through a net of optic cables to be stored on the computer disc in the control room. The time stamps exploited by the 500 MSPS and 250 MSPS cards are of 10 and 8 ns correspondingly.

Each event is stamped with a time it arrives at the system, corrected by the constant fraction discriminator. The trapezoidal filter was implemented while converting the pulse height information. In some cases, a light ion might be stopped by a ΔE detector and, therefore, is no longer able to deposit any energy in a E detector. Such events could not be used for the $E-\Delta E$ technique, and the preliminary in-beam data collection included rejection of all ΔE events not followed by firing of a corresponding backward E detector. As an overall time resolution is better for ΔE detectors than for E detectors, and an event in ΔE detector was chosen to be a reference event in the subsequent offline analysis. All the events in E detectors and OSCAR detectors arriving within a certain time (1 μs) with respect to a reference ΔE detector are grouped in a larger event. These combined signals present the raw data to be processed in the present work.

4.2 The ^{124}Sn(p,p$'\gamma$) experiment at the OCL

The experiment the present master thesis is devoted to was carried out on 26-27 February 2019 at the OCL at the University of Oslo as a part of the set of experiments on ^{117,120,124}Sn isotopes. The study of the PDR in ^{124}Sn isotope in the (p,p$'\gamma$) reaction was chosen to be performed with the proton beam energy of 16 MeV. The beam current was maintained at approximately 4.6 nA throughout the whole experiment. Due to the comparatively high cross-section for inelastic proton scattering for the chosen proton energy and target, the whole experiment was performed in less than one day, and this time was found to be sufficient to collect an adequate number of events ($\approx 6 \times 10^8$ in total) to provide decent statistics for the further processing.

In overall, two targets were exposed to the proton beam. The main self supported ^{124}Sn target has an isotopic enrichment of 95.3%, sufficient to ignore contributions from other stable Sn isotopes, and thickness of $\backsim$ 0.47 mg/cm^2. The second target exposed was ^{28}Si with thickness of $\backsim$ 9 mg/cm^2; this additional target was used for the scintillator detectors calibration. Both targets were placed in the holder in the central part of the vacuum target chamber. The SiRi particle telescope was placed in the backward position with respect to the target, thus, detecting all charged particles emitted with the azimuthal angle of $126^\circ \leq \theta \leq 140^\circ$. Figure 4.4 represents the relative positions of the target and detecting systems in the experiment. A proton follows the beam line and hits the target in the central position. The choice if the backward position for SiRi implies that the majority of light charged particles observed would be rather from the compound nucleus decay than direct reaction channels. Indeed, the direct reactions take place predominantly on the surface of a nucleus and yield a particle distribution peaked in the forward direction with respect to the beam line. A reaction via a compound nucleus involves redistribution of absorbed energy, and the particle angular distribution would be rather isotropic [129].

The kinematics analysis was carried out beforehand to verify that the combination of 16

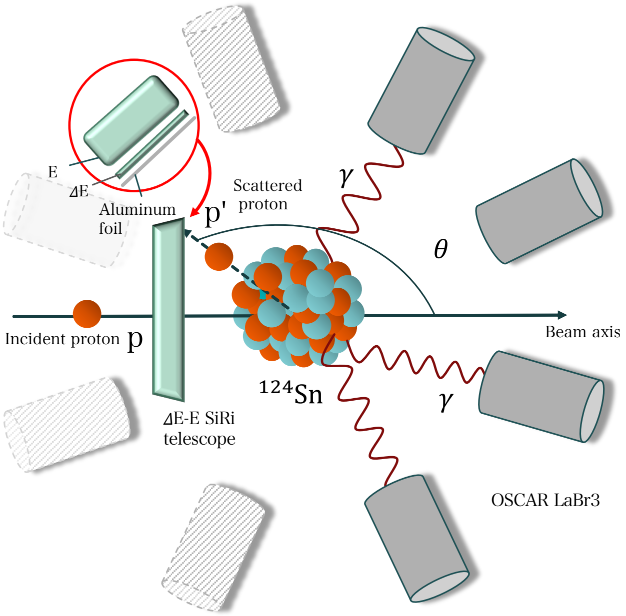

Figure 4.4: A principal scheme of the experiment on the ^{124}Sn isotope: a proton beam is incident on the ^{124}Sn target in the central position, scattered light ions are detected by the SiRi particle telescope, placed in the backward position (light blue color for both E and ΔE detectors). The target is surrounded by 30 LaBr$_3$:Ce scintillator detectors (grey color), registering photons produced in the deexcitation of target nuclei.

MeV protons and the backward position of the SiRi detector would lead to observation of events in the (p,p′γ) channel. This procedure was performed by means of the Qkinz application created to simulate different kinematic conditions for particles registered in 8 SiRi strips [130]. The application takes into account different target compositions and thicknesses as well. The calculation predicts 5 reaction channels to be kinematically allowed: elastic and inelastic proton scattering ^{124}Sn(p,p′)^{124}Sn, ^{124}Sn(p,d)^{123}Sn,^{124}Sn(p,t)^{122}Sn, and ^{124}Sn(p,α)In^{121}. The former two reaction channels are of particular interest for the present work. Geometry and the beam energy were conformed to be suitable to avoid punch-through for scattered particles, *i.e.* energy would be fully deposited in the E and ΔE detectors. In case of inelastically scattered protons, the recoil ^{124}Sn would be left in one of the excited states with subsequent deexcitation via emission of one or several γ-rays. If scattered in the solid angle covered by SiRi, proton is detected and information on its energy is written on the disc. This information enables calculation of the excitation energy E_x a target nucleus was left with. On the other hand, photons emitted are detected in 30 scintillator detectors surrounding the target chamber, their energies E_γ are recorded as well. If a particle and a photon are recorded in coincidence (within a time interval short enough to assume that a particle and a photon are emitted in the same event), one might reconstruct the matrix containing events characterized by uniquely attributed E_γ and E_x values.

4.2.1 Energy calibration of the SiRi particle telescope

As a charged particle ionizes an active volume of a silicon detector and charge carriers are collected, the total charge recorded would be proportional to the energy deposited in the detector.

In its turn, the total charge is proportional to the integral of a current pulse observed as an output of the detector. If the pulse shape does not change significantly [122], one could further set proportionality between the pulse integral and the pulse height. Thus, the pulse heights recorded are distributed over 32000 sequential channels and proportional to the energies of detected particles. However, they do not contain information on the absolute values of these energies. The overall aim of a detector calibration is to set correspondence between a channel number and a certain energy. If certain peaks in a spectrum are identified (*i.e.* the energy it appears with is known), one could set unique dependence of energy on a channel number.

In case of the SiRi particle telescope 64 combinations of $E-\Delta E$ detectors might be distinguished: 8 strips of each ΔE detector correspond to the same backward E detector, forming 8 different $E-\Delta E$ combinations for each of 8 E detector pads. All possible 64 $E-\Delta E$ combinations have their uniquely attributed energy-channel correspondences due to the different performances of separated detectors and attached electronics. For each of the $E-\Delta E$ combinations the simplest linear response is assumed:

$$E = a \cdot N_{ch} + b \tag{4.3}$$

where E is the true energy attributed to the channel number N_{ch}, a is the gain (1/keV) and b is the corresponding energy shift. Hence, only two channels identified to be related to certain energies are sufficient to set the linear calibration.

As it was already mentioned, the SiRi telescope exploits the $E-\Delta E$ technique, thus, the energy delivered in the E and ΔE (channel number) is recorded for each hit. As plotted for each combination of detectors, the $E-\Delta E$ spectrum is given in channel units and presents the so called banana-plot, mentioned in the previous section. According to the Bethe-Bloch formula 4.1, each banana would be characteristic for the different types of scattered particles

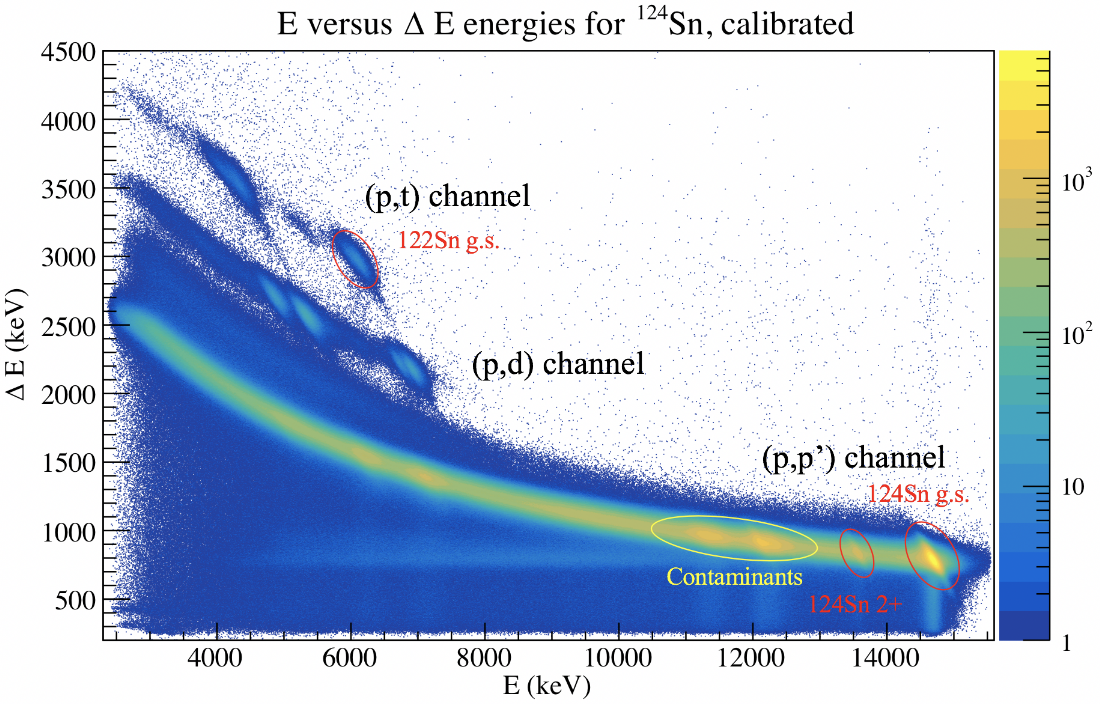

Figure 4.5: The $E-\Delta E$ spectrum measured in the ^{124}Sn(p,..) experiment. The x-axis denotes the energy deposited in the thick E detectors, the y-axis shows the energy deposited in the thin ΔE detectors. The spectrum is calibrated, and all 64 combinations of the $E-\Delta E$ detectors are added.

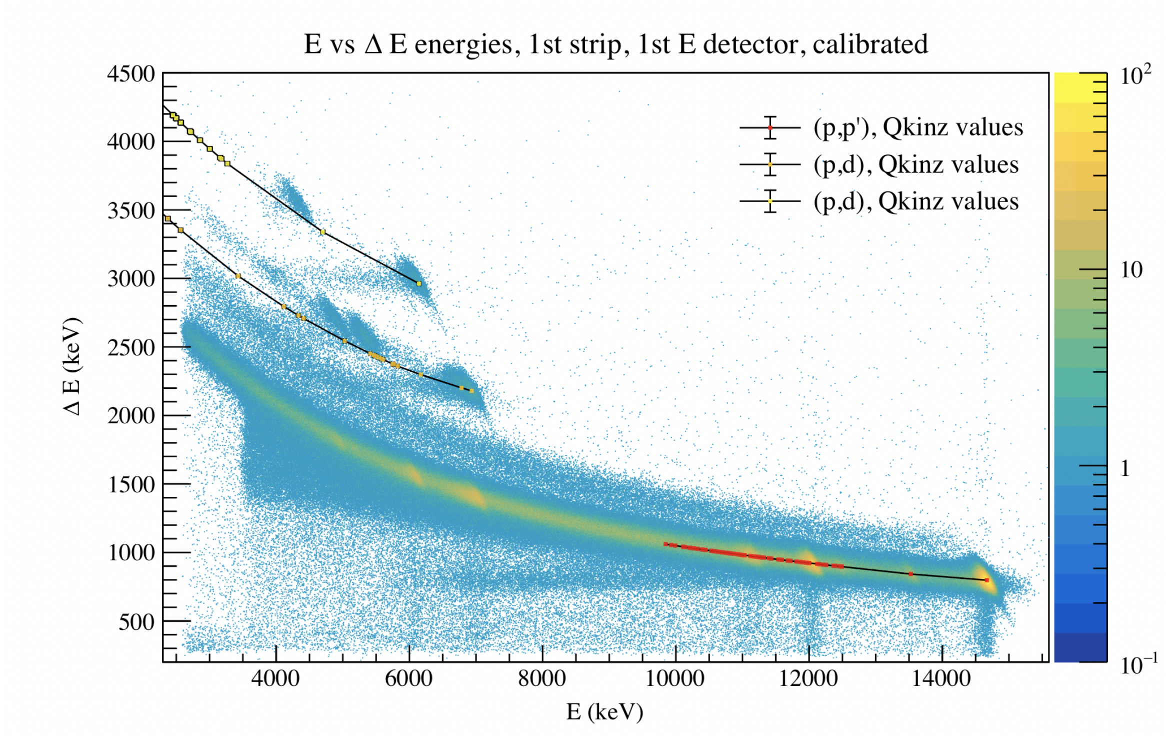

Figure 4.6: The $E - \Delta E$ spectrum measured in the ^{124}Sn(p,..) experiment for the first $E - \Delta E$ combination, calibrated. The theoretical Qkinz values for all three channels (p,p$'$), (p,d) and (p,t) are added.

and different reaction channels can be clearly distinguished. The lightest scattered particle, a proton with $Z = 1$, deposits the least energy while passing through the thin ΔE detector and, thus, all the proton-induced events can be found in the lowest banana (see Figure 4.5). The next reaction channel to be observed is the (p,d) events. And finally, a shade of the (p,t) banana could be observed in the upper part of the spectrum in Figure 4.5. As it was mentioned, the experiment took less than one day, and this time was not sufficient to gain appropriate statistics for the (p,t) channel or to observe events from the (p,α) channel.

The bright blobs in each channel allow us to indicate either the ground states of recoil nuclei or their excited states kinematically allowed in the reactions. The majority of the most high energy particles could be observed as the bright blobs on the right edge of each channel. The relative intensities of these regions are high enough to claim that the ground states of ^{124}Sn, ^{123}Sn, and ^{122}Sn are strongly populated as compared to the majority of higher-lying excited states. The prolonged blob of contaminant events (^{12}C and ^{16}O) could be easily seen in the proton banana. In addition, one could clearly distinguish the first excited state of ^{124}Sn next to the ground state. These observations imply that the centroids of these peaks (as projected on the E and ΔE axis) could be used for the calibration. However, the second and the third excited states of the ^{123}Sn isotope ($3/2^+$ at 24.6 keV and $1/2^+$ at 150.4 keV [90]) could hinder clear peak identification. Therefore, three states were identified and used for the linear calibration of SiRi: the ground state of ^{124}Sn, the first excited 2^+ state at 1131.7 keV in the same isotope, and the ground state of ^{122}Sn. The latter and the former, due to the sufficient difference between them on the ΔE axis, allow us to cover the suitable energy range for all ΔE detectors.

The Qkinz software package was used to estimate energies delivered by protons in the E and ΔE detectors for the cases of the recoil nucleus to be left in the ground and the first excited state. Similarly these values were estimated for tritons and the ground state of ^{122}Sn. It was taken into account that the energy delivered into the detectors vary slightly with the scattering

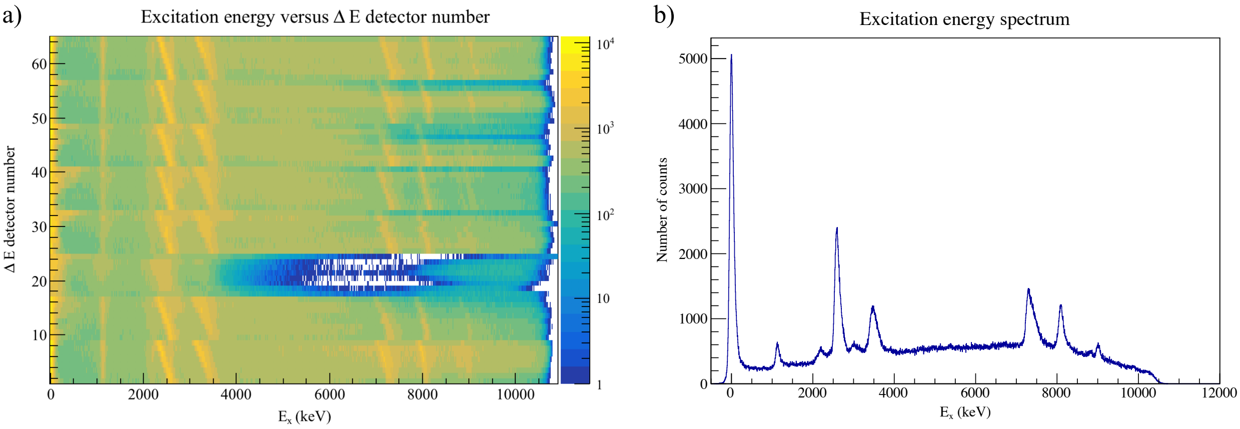

Figure 4.7: a) The excitation energy spectra aligned for all detector ID numbers. **b)** The excitation energy spectrum for the first combination of $E - \Delta E$ detectors, the ground state peak corresponds to the pronounced peak at 0 keV, the second peak corresponds to the first excited state of the ^{124}Sn isotope at 1131.739 keV [90]

angle from the innermost to the outermost strips in SiRi. The gains and shifts were calculated for all 64 combinations of E and ΔE detectors. The fit introduces small uncertainties and shifts in the vicinity of theoretically predicted values (Qkinz calculations), which are disregarded in the following analysis. In addition, the Qkinz values could deviate from the real energies deposited to the detectors due to a certain shift of the proton beam from the true symmetry axis while tuning. However all these uncertainties lie well within the experimental resolution of ≈ 100 keV, assumed for the next analysis steps, and will not contribute significantly to the bulk error of the final results.

One of the calibrated spectra obtained is presented in Figure.4.6, the theoretical Qkinz values are plotted above the experimental peaks. Some deviations of theoretically estimated points and experimental values could be seen for the (p,d) and (p,t) channels: the explanation might be hidden in some nonlinear effects, not accounted for by the linear calibration. However, a good agreement is observed for the region of the (p,p′) channel, essential for the present work. As all E and ΔE detectors are calibrated, the total energy could be estimated as $E + \Delta E$ and converted into the excitation energy of a nucleus. This procedure was again performed by means of the Qkinz software. The latter allows to estimate the dependence between the energy deposited to the E and ΔE detectors within one strip and excitation energy of a recoil nucleus, taking different scattering angles and,thus, different particle paths into account. The excitation energy spectra versus the detector number (ΔE detector) are presented in Figure 4.7. Here, the proton channel is selected by putting the corresponding energy gate on the lowest banana as well as the time gate described in the next subsection. In this figure one could clearly distinguish the ground state peak at 0 keV with the full width half maximum FWHM ≈ 99.45 keV. The next peak centered at at 1132.13 keV corresponds to the first excited state of ^{124}Sn isotope (2^+ state) [90]. The FWHM$\approx$ 159.11 keV for the corresponding peak could serve as the representative SiRi resolution at 1131.74 keV for the present experiment, given by $r = \frac{\text{FWHM}}{E} \approx 14\%$.

4.2.2 Event selection for the SiRi detector

In addition to the energy calibration one should also take the time alignment of the E detectors with respect to the different ΔE reference detectors into account. The time difference between the E and ΔE detectors for the events in vicinity of the ground state peak were aligned at 0 for all 64 detector combinations.

Since the primary aim of the preliminary analysis was to select the (p,p′) events, the

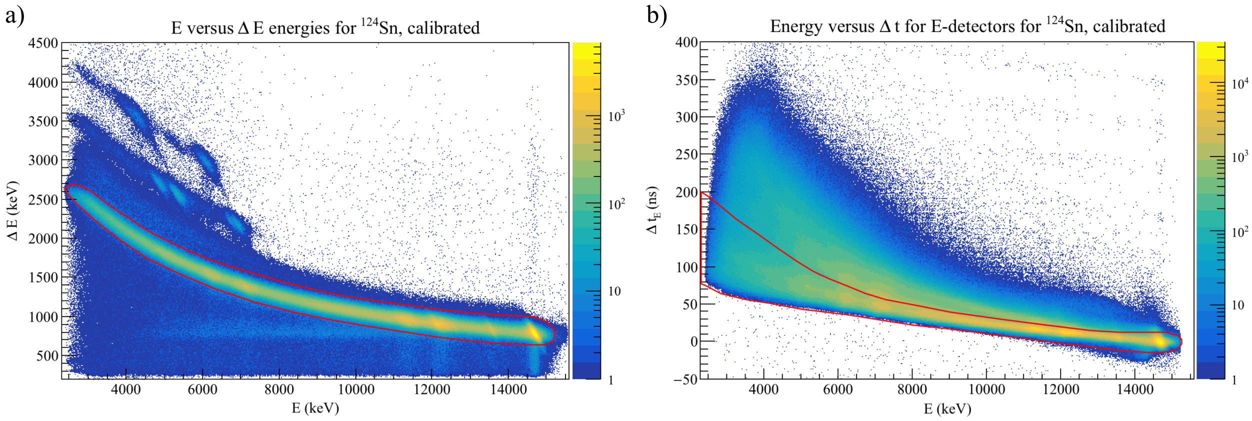

Figure 4.8: **a)** The $E - \Delta E$ spectrum with a graphical cut applied for the (p,p′) event selection. **b)** The time difference between the E and ΔE detectors vs the energy registered in the E detectors and the time cut applied.

^{124}Sn(p,p′)^{124}Sn events from the lowest (p,p′) gate have to be selected with one of various procedures. In case of the present experiment, the (p,p′) channel contains sufficient statistics and is well energetically separated from the (p,d) and (p,t) channels, located above. This implies that the (p,p′) events can be confined accurately enough in a graphical cut. These events were sorted out with a graphical gate represented by the red cut in Figure 4.8 a). In addition, the energy-dependent time gate was put on the time difference between the E and ΔE signals. This must be required for the selection of so called true coincidences between the E and ΔE firings. It takes certain time for a charged particle to penetrate the latter, hit the former and generate the time difference recorded. The structure of events implies that all the E signals within 1 μs with respect to a reference ΔE detector are recorded and all random signal coincidences, stemming from particles in different beam pulses, would be written down alongside the true coincidence events. The true event selection procedure was also performed with a graphical time gate put on the time-energy spectrum (see Figure.4.8 b)) for the E detectors. The gate extension towards higher energies takes into account that the signal arrival time in the E detector might be delayed by up to 200 ns for the slowest particles. There is an uncertainty in putting a gate in the low energy region that might lead to a certain loss of true events. However, the statistics gained in the experiment is large enough to consider that the time gate up to 200 ns will contain the majority of true events for the further analysis.

Applying the both graphical gates (see Figure 4.8 a) and b)), the events from elastic and inelastic scattering were selected so that each event is a combined signal from a certain ΔE detector and the corresponding E detector behind, arising from the same recoil particle born in the (p,p′) reaction.

4.2.3 The OSCAR energy calibration

Since each event recorded in the OSCAR detector array has an attributed energy information written in arbitrary channel units, the similar energy calibration procedure must be applied to each LaBr$_3$:Ce detector. For this purpose an additional run on the ^{28}Si isotope was performed with the same beam settings as in the main experiment. This isotope was chosen to be the calibration target owing to a set of well distinguishable γ-rays covering a relatively wide energy range.

In contrast to the silicon particle detectors, the correlation between energy and a channel number can not be assumed to be linear for LaBr$_3$:Ce detectors: fast intense signals induced in an active volume of a detector would inevitably induce high peak currents in the adjacent

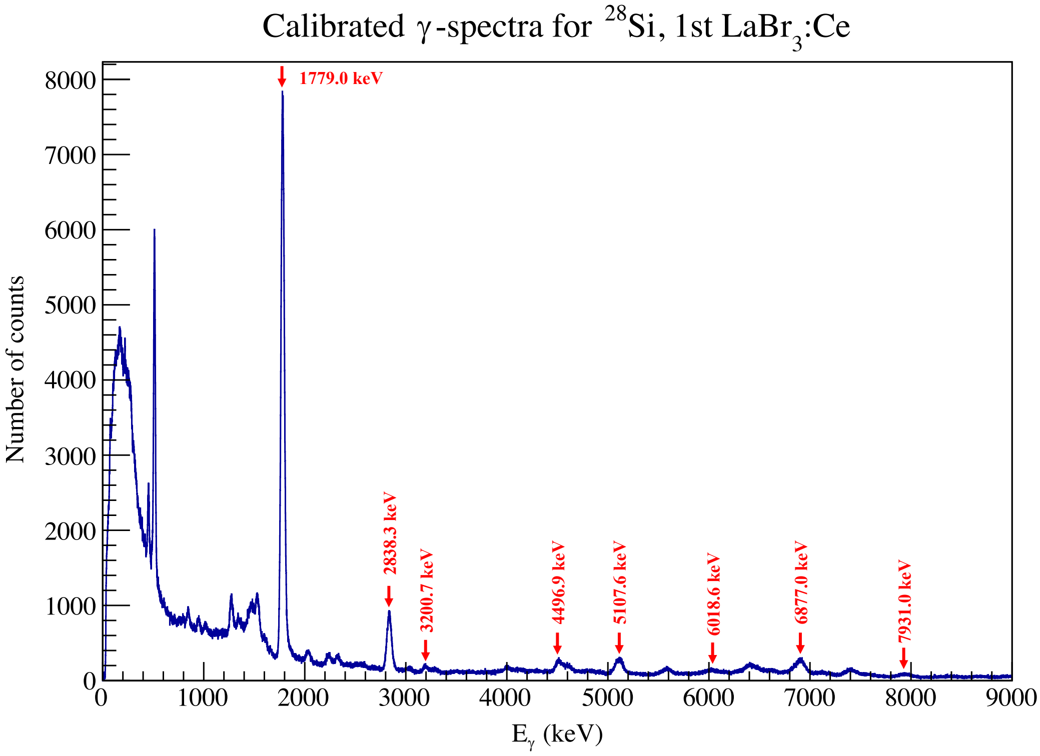

Figure 4.9: The calibrated γ-spectrum obtained for the ^{28}Si for the first LaBr$_3$:Ce detector, the (p,p′) gate is applied.

photomultiplier tubes, and the pulse height recorded will inherit the non-linear effects. The LaBr$_3$:Ce crystals similar to those used in the experiment were tested with other Hamamatsu types of PMTs [131]. It was shown that the deviation from the linear trend might cause a calibration error larger than 1% and a polynomial calibration was recommended. In the present work a quadratic calibration was chosen:

$$E = a_0 + a_1 \cdot N_{ch} + a_2 \cdot N_{ch}^2, \tag{4.4}$$

where E is the energy, N_{ch} is a channel number recorded, a_0, a_1, a_2 are the calibration fit coefficients. In order to distinguish these transitions from the bulk spectrum containing all possible γ-transitions, the ^{28}Si data from the particle telescope were calibrated with the gains and shifts described in the previous section and graphical energy gates were put on several excited states.

The quadratic fit implies that the number of peaks to be fitted should be large enough, and energies measured should, in principle, cover the whole range of interest. Therefore, 7 different gates on peaks and the corresponding γ-transitions were chosen in ^{28}Si. For example, the first gate covered the first excited state in ^{28}Si. The γ-spectrum obtained with this gate allows to reveal a peak at $\approx$ 1779 keV, corresponding to the γ-transition from the first 2^+ state to the ground 0^+ state. Other gates along the (p,p′) channel allow to distinguish γ-transitions up to $\approx$ 8000 keV. Since the γ-energies of interest in ^{124}Sn are expected to cover the range up to the neutron separation energy $S_n(^{124}\text{Sn})$ = 8489 keV [90], 8 transitions identified should be sufficient to enable a good γ-energy calibration.The level scheme for this nucleus, containing all the transitions identified, is presented in Figure.A.1. In addition, similar procedure was performed for the first excited state in ^{124}Sn providing a calibration point in vicinity of 1 MeV. The calibrated energy spectra are shown in Figure 4.9 and Figure 4.10, and comparison of the

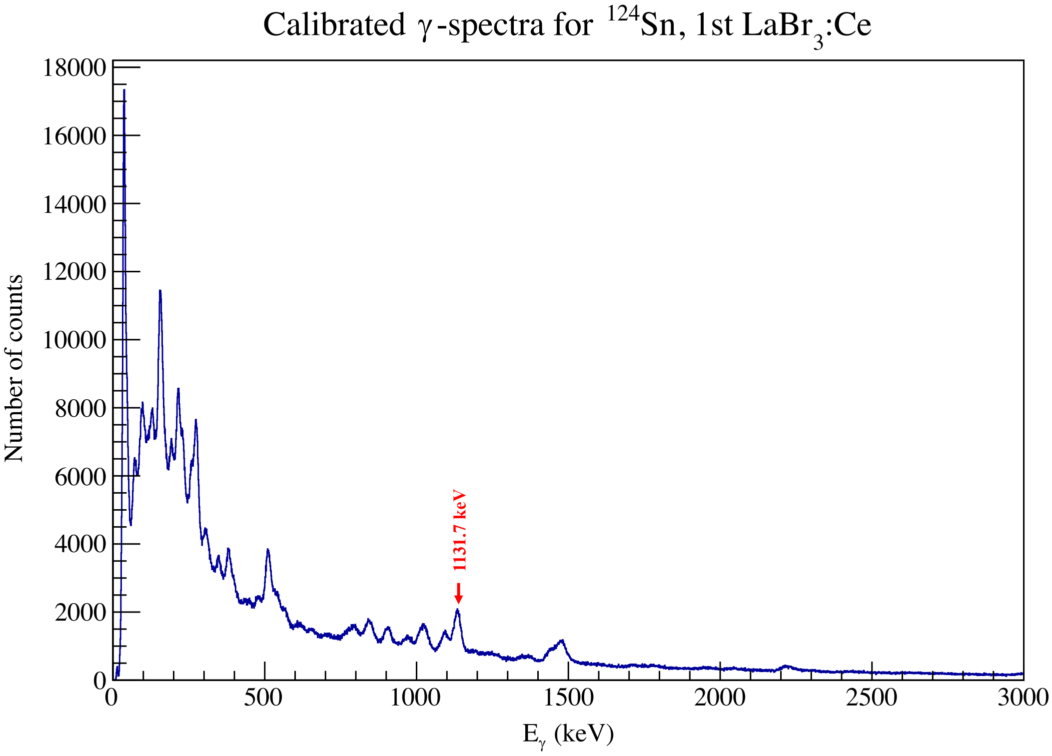

Figure 4.10: The calibrated γ-spectrum obtained for the ^{124}Sn for the first LaBr$_3$:Ce detector, the (p,p$'$) gate is applied.

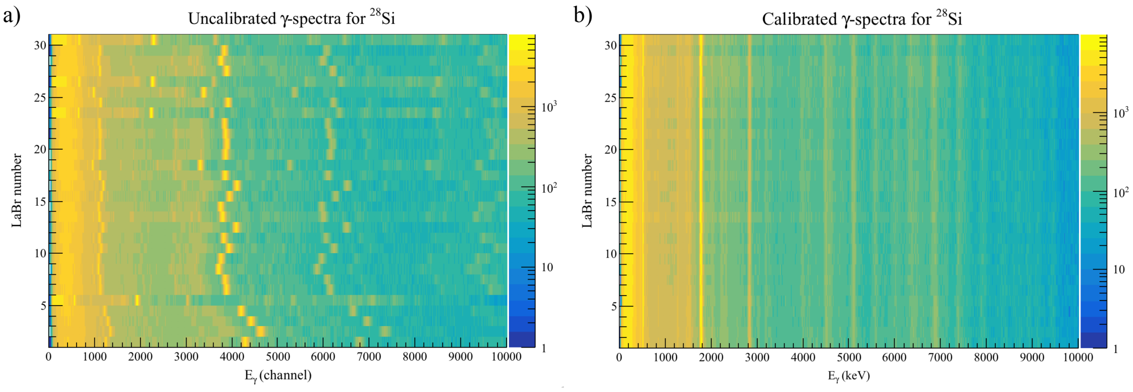

Figure 4.11: **a)** The raw γ-spectra obtained for the ^{28}Si vs detector number. **b)** The calibrated γ-spectra obtained for the ^{28}Si vs detector number.

spectra before and after the calibration is presented in Figure 4.11. The full width half maximum was estimated to be FWHM≈41.27 keV for the first excited 2^+ state in ^{124}Sn corresponding to $r = \frac{\text{FWHM}}{E} \approx 3.6\%$, the typical value expected for the LaBr$_3$:Ce detectors.

4.2.4 The time alignment of the OSCAR detectors and further event selection

As a charged particle hits one of the ΔE detectors and the corresponding E detector, a photon stemming from the same reaction might be incident on one the scintillator detectors. All of them should be treated equally in the sense of timing, *i.e.* the zero time reference for one

LaBr$_3$:Ce should coincide with the zero references for other detectors. Initially, a certain shift between them must be present due to different electronics performance (including the PMTs) and cable lengths, and, thus, the alignment procedure is required. As it was already mentioned, in Subsection 4.1.3, time resolution of the ΔE detectors is comparatively better than that for the E detectors, and if the time difference between signals in ΔE and LaBr$_3$:Ce is considered, the smaller inherited uncertainty in time can be achieved as compared to taking the E detectors as a reference. In order to make the zero references match each other, the time shifts between the prompt peak (stemming from the same pulse burst) for each combination of LaBr$_3$:Ce detector and ΔE detector (64×30) were taken into account to calibrate the prompt peaks at the 0 time value. The time spectra for all 30 LaBr$_3$:Ce detectors with respect to the first ΔE detector before and after the time alignment is presented in Figure.4.12.

The time gap for the sorted events is large enough to include up to several LaBr$_3$:Ce signals, which do not arise from the same reaction event, as a particle is registered in the reference ΔE detector. This fact is clearly demonstrated by the Figure 4.13, where the peaks originating from different beam pulses can be seen. An approximate time difference between beam pulses is of 58 ns, meaning that a significant amount of LaBr$_3$:Ce signals from the reactions induced by protons from the adjacent pulses will be written in the original event. In order to eliminate them a time gate on the prompt peak at 0 ns should be applied. The gate was chosen to be of 10 ns in width and was found to contain a sufficient number of true coincidence events. However, the random background coincidences are still present within this prompt gate. An additional gate with the

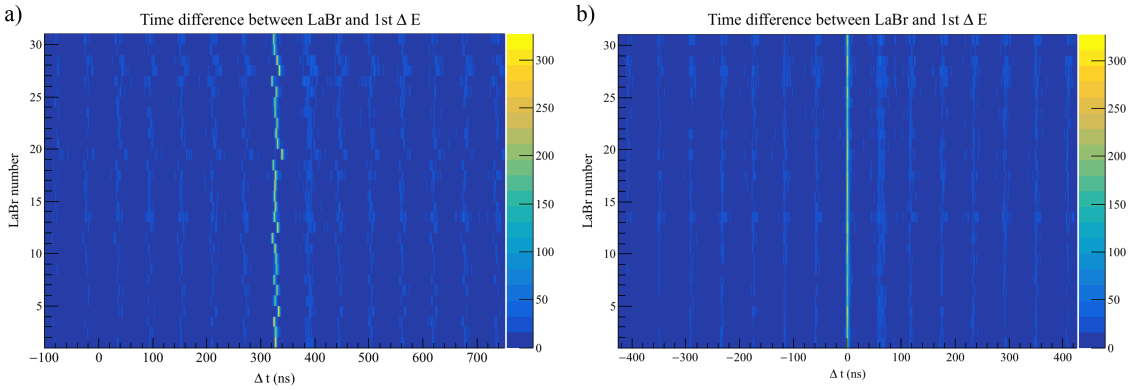

Figure 4.12: **a)** The recorded time difference between a chosen ΔE detector and 30 LaBr$_3$:Ce detectors before alignment. **b)** The aligned time difference between a chosen ΔE detector and 30 LaBr$_3$:Ce detectors.

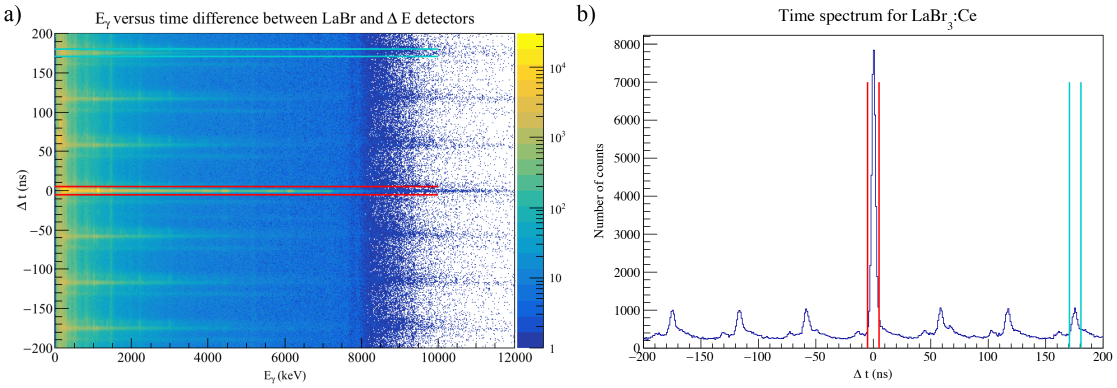

Figure 4.13: **a)** The time spectra ($\Delta E-$LaBr$_3$:Ce time,difference) vs E_γ energy, all calibrated LaBr$_3$:Ce detectors are included. **b)** Time spectrum, projection at E_γ = 1000 keV. The gates on the prompt (red color) and side (light blue color) peaks are included.

same width was set around one of the subsequent beam pulses (±5 ns). The events sorted with this gate can be considered to be attributed to the background; they were subtracted from the events within the prompt gate to minimize the random coincidences.

4.2.5 The raw coincidence matrix

Following the preliminary calibration procedures, the final, or so-called raw coincidence matrix was extracted. The matrix, resulting from the background subtraction, is presented in Figure 4.14. It contains the γ-energy spectra for each excitation energy, corresponding to sequential excitation energy bins. The calibration quality could be easily checked with a position of a diagonal line E_γ=E_x which follows the centroids of the outermost diagonal line of the matrix (see Figure 4.14, yellow line). Additional check is provided by the position of three bright blobs at 4438.9 keV (gamma transition from the first excited state 2^+ to the ground state in ^{12}C), 6048.2 keV and 7115.1 keV (transitions from 0^+ and 1^- to the ground state in ^{16}O). The neutron separation energy line was plotted as well at S_n(^{124}Sn)=8489.2 keV [90].

The previous data processing procedure included both energy and time gating on $E - \Delta E$ energy spectrum and E and LaBr$_3$:Ce time differences with the ΔE detectors. This implies that the presented matrix should contain events stemming from a detection of a scattered proton and a photon or photons, emitted in the same ^{124}Sn(p,p′γ)^{124}Sn reaction for the same nucleus. A negligible amount of false coincidence events would be still present due to a certain flexibility of all the gates applied. The harsher gates could be used, but one must be aware of a large number of valuable true events, which will be inevitably lost in this case.

The final matrix presents the distribution of counts over different excitation energies of

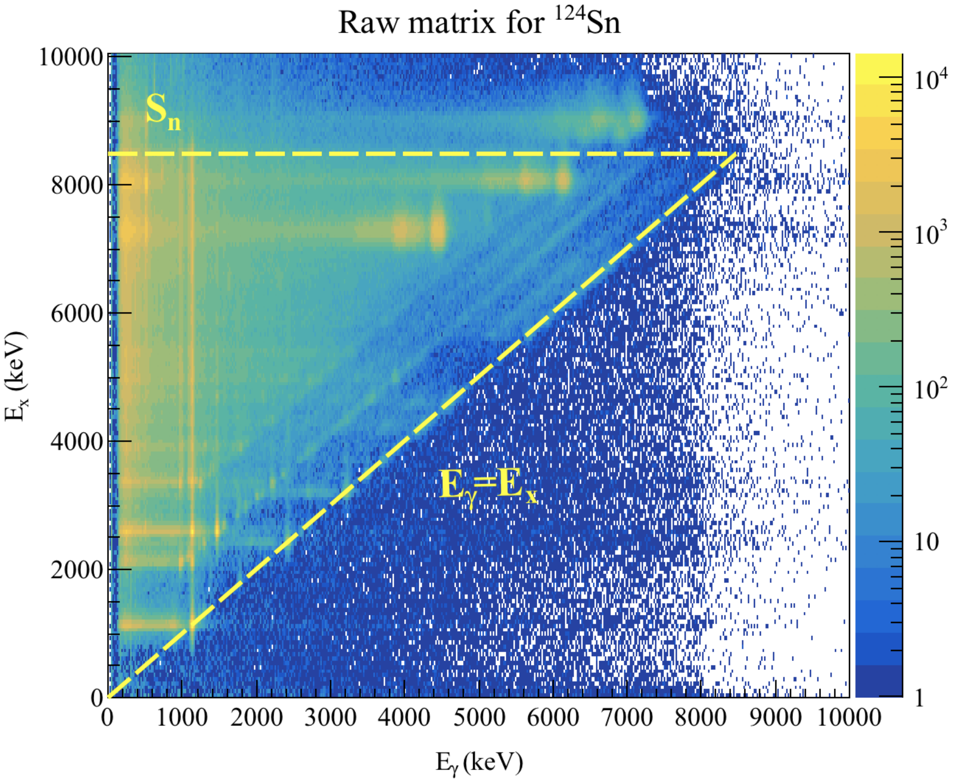

Figure 4.14: The raw γ-p coincidence matrix, yellow dashed lines denote the ground state transitions $E_\gamma = E_x$ diagonal and the neutron separation limit S_n.

target nuclei and γ-energies of photons emitted. The latter could not exceed the excitation energy of a nucleus due to the energy conservation law and, thus, only a few (dark blue field) remaining background counts are observed below the diagonal line $E_x = E_\gamma$. It can be also seen that the amount of counts above the neutron separation energy drops significantly; there are some data at $E_x > S_n(^{124}\mathrm{Sn})$ at the lowest E_γ. This is due to inability to distinguish the ^{124}Sn(p,p$'\gamma$)^{124}Sn reactions of interest from ^{124}Sn(p,p$'$nγ)^{123}Sn. However, both neutron emission events and the rest of background events will be discarded in the following analysis. Another complication observed is the three lines at high excitation energies stemming from ^{12}C and ^{16}O impurities.They are to be smoothed in the proceeding analysis. The coincidence matrix obtained in this section is the main input for the Oslo method; the next steps of the analysis would be described and explained in detail in the following chapter.

Chapter 5

The Oslo method: theory and application

It is almost 20 years since the Oslo method was first introduced for the analysis of various transfer and inelastic scattering reactions (*e.g.* (^{3}He,$\alpha\gamma$), (d,tγ), (p,p$'\gamma$), *etc.*) performed at the Oslo Cyclotron Laboratory. This method has evolved significantly during the last two decades to its present form. The primary goal of this method concerns the study on the statistical behavior of a nuclear matter via simultaneous extraction of the γ-ray strength function and nuclear level density from particle-γ coincidence events. The methodology involves several successive steps, namely the unfolding with the folding iteration method, described in Subsection 5.1.1, the Compton subtraction procedure and extraction of primary γ-rays, outlined in Subsection 5.1.2 and Section 5.2 correspondingly.

As the raw particle-γ coincidence matrix is transformed into the so-called first-generation matrix, containing the first γ-transitions only for each cascade observed, one could successfully extract the γ-ray strength function and nuclear level density applying the procedure described in Sections 5.3 and 5.4. The following chapter provides the recipe generalizing all the steps mentioned and applied for the analysis of (p,p$'\gamma$) reaction in the present work. As almost all convoluted multistage procedures, the Oslo method is based on several crucial assumptions, discussed in this chapter. The choice of all input parameters required for the extraction of the γ-ray strength function and level density and the results obtained will be provided and discussed in the next chapter.

5.1 Need for detector response correction

The proton-γ coincidence matrix, provided in Subsection 4.2.5, contains the spectra, required for the extraction of the nuclear level density and γ-ray strength function for γ-energies up to the neutron separation threshold. However, a reasonable physical interpretation of events and features, recorded in the matrix, is required to extract these nuclear properties.

The γ-spectra recorded in each bin of excitation energy in the raw coincidence matrix contain information on how a scintillator detector in the array responds to an incident γ-ray, rather than pure information on the original γ-ray energy. The detector response is a complex characteristic attributed to the whole detecting setup; it is sensitive to all the interaction types a particle of a certain energy is able to undergo in an active volume of a detector for a given geometry, design, type of the detecting system. Depending on the registration mechanism, different detector materials might be suitable for some radiation types and energy ranges, but insensitive to others. As it was already mentioned, the OSCAR scintillator detector is able to measure γ-rays in a relatively wide energy diapason, ranging beyond the neutron separation energy in ^{124}Sn.

As a photon enters an active volume of a LaBr$_3$:Ce detector in the OSCAR array, it might interact via one of the following main mechanisms: the coherent Rayleigh and Thomson scattering, the photoelectric effect, Compton effect and pair production. Practically, only the events contributing to energy loss would create specific features in a detector response. If a photon does not lose its energy in an interaction process, it could either escape or proceed moving in the same detector and undergo further interactions. The latter might performed via two mentioned processes: the Rayleigh scattering, implying a coherent re-emission of a photon with no energy transferred to an atom, and the Thomson scattering, involving an elastic scattering on the outermost orbital electrons considered as “free”electrons. Both processes, contributing to a photon propagation, take place for lowest photon energies (significantly beyond 1 MeV) and are of no practical interest for the detector response. In contrary, the latter three processes could result in a photon energy transferred partially and, thus, create specific features distorting the true photon spectrum registered by a detector. Besides the detector material, the relative input from these processes depends on a photon energy and the response function evolves as we shift from the lowest to the highest energy bin.

The photoelectric effect has a particularly high cross-section for the low energy photons (below ≈ 1 MeV) and results in energy transfer to an orbital electron. The initial photon energy E_γ is then redistributed over the binding energy (tens of keV) of an ejected electron and its kinetic energy. The momentum conservation law forbids the photoelectric effect on free electrons, and the cross-section peaks at a photon energy coinciding with the innermost K-electron binding energy [132]. The electron ejected from an atomic orbital could be subsequently detected and contribute to a so-called full energy peak, well approximated by the Gaussian function and centered at approximately E_γ (electron binding energy correction which is usually negligible).

For the comparatively higher photon energies ($1 \text{ MeV} \lesssim E_\gamma \lesssim 5$ MeV), the Compton scattering effect becomes dominant. In this case, only a fraction of energy is transferred to an orbital electron. The recoil photon is scattered at an angle θ with the lower energy E'_γ, dependent on this angle:

$$E'_\gamma = \frac{E_\gamma}{1 + \frac{E_\gamma}{m_e c^2}(1 - \cos\theta)}. \tag{5.1}$$

Hence, an electron recorded carries information on only a fraction of the incident photon energy, as a photon might escape from the detector volume and carry the rest of energy away. The bulk of the Compton electrons forms the pronounced Compton background below the full energy peak and could be easily seen in both experimental spectra, presented in the previous chapter (see Figure 4.9 and Figure 4.10).

If an incident photon energy exceeds two electron masses, $E_\gamma > 2m_e \approx 1.022$ MeV, the pair production might take place in the Coulomb field of an atomic nucleus. As a result, the produced electron can be detected and a positron would annihilate with one of the orbital/free electrons, present in the detector material. The latter process would subsequently result in two photons of 0.511 MeV energy with a relative angle of 180° between their initial trajectories. Their energy will not be sufficient to initiate another pair production, but they will still be able to undergo Compton scattering and photoelectric effect and be eventually registered delivering their energies. However, one of these 0.511-MeV photons might escape from the detector volume, and the additional peak, or so-called single escape peak, will be registered at $E_\gamma - 0.511$ MeV. If both annihilation photons escape, the double escape peak will be observed at $E_\gamma - 1.022$ MeV. These peaks might be especially prominent for small volume detectors. In addition, the detector array geometry might enable one of the detectors to capture one of the annihilation photons escaped from another detector. These photons would then result in the 0.511 MeV annihilation peak, which will be seen alongside the single and double escape peak built up on the Compton background (see Figure 5.1 a)).

The energy spectrum registered $r(E)$ could be mathematically related to the true photon

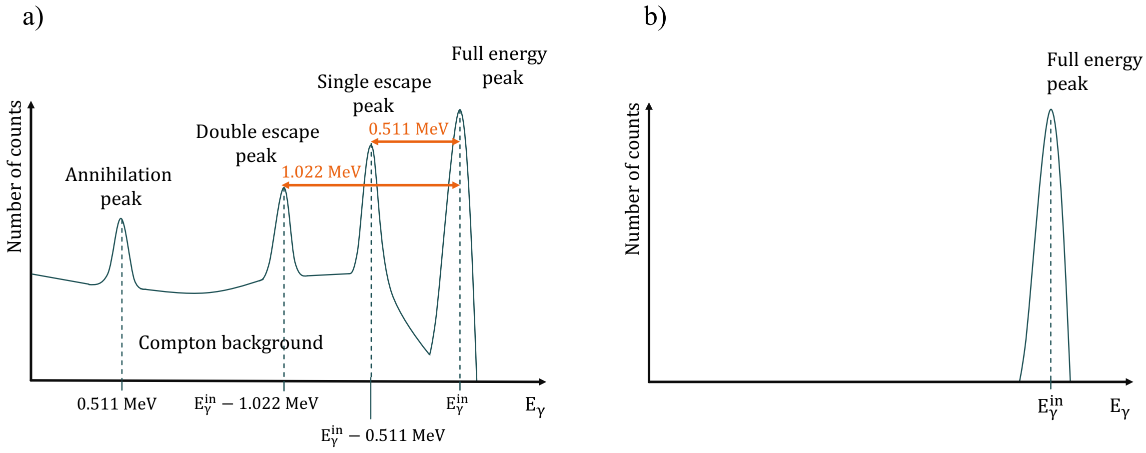

Figure 5.1: a) Schematic representation of a monoenergetic γ-spectrum for the incident energy E_γ recorded by a scintillator detector with the three main energy transfer mechanisms taken into account. **b)** The ideal monoenergetic γ-spectrum, corresponding to the primary goal of the unfolding procedure. In both figures the scaling is arbitrary.

energy spectrum $u^0(E)$ by the convolution transform [122]:

$$r(E) = \int F(E, E')u^0(E')dE, \tag{5.2}$$

where $F(E, E')$ is the detector response function. It can be measured in the experiments with monoenergetic photons or simulated with the Geant4 software [133]. The presented experiment exploits the newest version of the response function obtained in 2018 by means of Geant4 simulations and tested for several observed experimental spectra [134]. From now on, the relation between the true and observed spectra will be written in the matrix form as:

$$\mathbf{r} = \mathbf{F}\mathbf{u}^0 = \begin{pmatrix} r_1 \\ r_2 \\ \vdots \\ r_N \end{pmatrix} = \begin{pmatrix} F_{11} & \cdots & F_{1n} \\ F_{21} & \cdots & F_{2n} \\ \vdots & \ddots & \vdots \\ F_{n1} & \cdots & F_{nn} \end{pmatrix} \begin{pmatrix} u_1^0 \\ u_2^0 \\ \vdots \\ u_n^0 \end{pmatrix}. \tag{5.3}$$

Here, n is the index denoting the maximum number of bins in both the observed $\mathbf{r}$ and the true $\mathbf{u}^0$ spectra (shown in Figure 5.1 a) and b) correspondingly). The principal goal of the procedure described in the next subsection is to obtain the original, or incident, γ-spectrum with the raw, observed spectrum and modeled response function for the OSCAR array.

5.1.1 Unfolding with the folding iteration method

The convolution of the response function and the true γ-spectrum is often referred as the folding procedure, and the true γ-spectrum as the unfolded spectrum. However, the opposite process is of particular interest in this step of the data analysis: the unfolding of the folded spectrum $\mathbf{f}$ with the given response matrix $\mathbf{F}$. The most straightforward way to accomplish this is to invert the matrix equation (5.3):

$$\mathbf{u}^0 = \mathbf{F}^{-1}\mathbf{f}. \tag{5.4}$$

There are several serious drawbacks of this method: as the dimension n involved is large, a computed solution might be unstable as the response matrix might be ill-conditioned. In addition, it will introduce significant oscillations in the unfolded matrix. The present thesis exploits the folding iteration method, primarily based on the simplicity of the folding procedure. In contrast to matrix inversion, this procedure is relatively fast and less sensitive to particular defects of the raw matrix, *e.g.* driven by low statistics, which makes it ideal for OCL experiments. The procedure is performed in series of iterations aiming to approach the true, incident spectrum, and can be effectively split into several steps as outlined in [135]:

1. A trial function for the unfolded spectrum $\mathbf{u}^0$ is chosen. The Oslo method software ([134]) exploits the raw spectrum $\mathbf{r}$ as a starting point, but, as a general rule, the choice might be arbitrary:
$$\mathbf{u}^0 = \mathbf{r}. \tag{5.5}$$
2. The trial function $\mathbf{u}^0$ is folded with the response function:
$$\mathbf{f}^0 = \mathbf{F}\mathbf{u}^0. \tag{5.6}$$
3. The difference between the observed spectrum $\mathbf{r}$ and the folded spectrum $\mathbf{f}^0$ is estimated: the main goal now is to make the latter approach the former. In practice, this could not be done with one folding procedure only, and one needs to construct the next, improved, trial spectrum $\mathbf{u}^1$. It could be obtained by taking the difference between the observed and the first folded spectrum as:
$$\mathbf{u}^1 = \mathbf{u}^0 + (\mathbf{r} - \mathbf{f}^0). \tag{5.7}$$
4. The folding procedure is repeated; the new folded function $\mathbf{f}^1$ is obtained and the next approximation of the true unfolded spectrum is made as $\mathbf{u}^2 = \mathbf{u}^1 + (\mathbf{r} - \mathbf{f}^1)$.

The iterations are performed until the calculated difference between the observed spectrum and the folded spectrum is commensurable within the experimental uncertainties, *i.e.* when $\mathbf{r} \approx \mathbf{f}$ is achieved. Some works suggest that the amount of iterations should be large enough to adjust the current f^i to match the observed spectrum. However, the large number of iterations might result in severe oscillations in the spectra. In addition, the quality of the unfolding procedure is tightly related to the resolution applied while determining the response function. This resolution is taken as FWHM $\approx$ 0.1 FWHM^{exp} to eliminate undershooting of pronounced peaks in the unfolded spectrum as recommended in [136]. The recommended number of iterations for the OCL experiments is of 10-20 iterations [135].

The steps of the procedure, described above, were applied consecutively to the raw p-γ coincidence matrix for ^{124}Sn. The ^{12}C and ^{16}O impurities initially present in the raw matrix were still present after a smoothing procedure and 20 iterations were found to be insufficient to eliminate strong oscillations along the corresponding excitation energies. The upper limit of the number of iterations was set to be $i = 300$ in the present project; surprisingly, the larger number allowed to smooth the oscillations without creating significant additional oscillations of γ-ray spectra. Similar effects were also observed in the preliminary analyses of recent OCL experiments on other nuclei, for which strong contaminants in the spectra were also present.

5.1.2 The Compton subtraction method

A certain advantage of the unfolding procedure via the iterative folding method is its ability to reproduce a realistic shape of the unfolded spectrum. Nevertheless, this advantage is partially diminished by the strong, possibly artificial oscillations originating from the unfolding procedure itself. The straightforward smoothing of the unfolded spectrum will raise up some complications in distinguishing between real physical peaks and remaining smoothed oscillations. One probable solution to this problem was proposed in [135] in form of the so-called Compton subtraction method. This method is primarily based on the properties of the Compton background behaving as a slowly varying function of energy, which could be successfully subtracted from the unfolded spectrum while being strongly smoothed. If the Compton background is extracted from the original raw spectrum **r**, it would contain the same statistical fluctuations, and the following smoothing aims at eliminating them. This correction method is, thus, based on the physical principles rather than artificial mathematical procedures and could be described by the following steps:

1. Monoenergetic γ experiments are carried out in advance in order to construct a response function and estimate the probabilities for counts to belong to either the full energy peak *(f)*, single escape peak *(se)*, double escape peak *(de)*, annihilation peak *(a)* or the Compton background *(cb)* as a function of γ-energy. The total probability is then normalized as [135]:

   $$p_f + p_{se} + p_{de} + p_a + p_{cb} = 1. \tag{5.8}$$

   Such a separation allows us to estimate the relative contributions from the different processes, forming the features of the raw spectrum.

2. The final spectrum obtained in the iterative folding procedure is used as the main input for the Compton subtraction method. From now on it would be denoted by **u**. This spectrum is used to calculate the supplementary spectrum built up by the predicted contributions from the prominent peaks as:

   $$v(i) = p_f(i)u(i) + w(i), \tag{5.9}$$

   here i is the bin number and $w(i) = u_{se}+u_{de}+u_a$ is the sum of contributions from the single, double escape and annihilation. These contributions could be defined as $u_{se}(i - i_{0.511}) = p_{se}(i)u(i)$, $u_{de}(i - i_{1.022}) = p_{de}(i)u(i)$, and $u_a(i_{0.511}) = \sum_i p_a(i)u(i)$ with the bins $i_{0.511}$ and $i_{1.022}$, corresponding to 0.511 and 1.022 MeV energies.

3. Each peak is smoothed with the Gaussian distribution. The annihilation peak is smoothed with the experimental resolution r_{exp} =1 FWHM, whereas the single escape, double escape and full energy peaks have to be smoothed by both the experimental observed resolution r_{exp} and the response matrix resolution $r_{rm} = 0.1$ FWHM, providing an overall resolution of $\sqrt{1.0^2 - 0.1^2}$=0.99 FWHM.

4. The Compton background spectrum is obtained via subtraction of the predicted peak spectrum $v(i)$ from the observed spectrum $r(i)$:

   $$c(i) = r(i) - v(i). \tag{5.10}$$

   Since the initial raw spectrum **r** contains typical statistical fluctuations, the same fluctuations will remain in the Compton background spectrum $c(i)$. As it was already mentioned, this spectrum is assumed to be a slowly varying function of energy and, therefore, could be subject to the strong smoothing with the experimental resolution of 1 FWHM.

5. Subsequent subtraction of the smoothed peaks $w(i)$ (excluding the full energy peak) and the smoothed Compton background $c(i)$ from the raw spectrum would yield the new

spectrum, containing the full energy peaks only, and the artificial bias, inherited due to the unfolding procedure, will be, thus, suppressed. The true distribution of γ-rays could be obtained by correcting the obtained spectrum $r(i) - c(i) - w(i)$ for the full energy detection probability:

$$u_{corr} = \frac{1}{p_f(i)}(r(i) - c(i) - w(i)). \tag{5.11}$$

6. The final step involves the correction for the total γ-ray efficiency $\epsilon_{tot}(i)$ of the OSCAR detector array

   $$U(i) = u_{corr}(i)/\epsilon_{tot}(i), \tag{5.12}$$

   The final function $U(i)$ is the desired approximation to the true, incident γ-spectrum, corrected for all the artifacts stemming from the unfolding procedure; this is the starting point for the the first generation γ extraction, described in the next subsection.

The combination of the iterative folding procedure and the Compton subtraction method was shown to serve as the good framework for the unfolded spectrum subtraction in numerous OCL experiments (*e.g.* see [137]). As the presented experiment was carried out with the quite similar experimental conditions (with the exception of NaI:Tl detectors substituted with the LaBr$_3$:Ce detectors, a beam type and energy), it was reasonable to apply these steps of the Oslo method for the analysis.

5.2 The primary γ extraction procedure

The unfolded matrix contains a set of full energy peaks, corresponding to all possible γ-transitions in the chain of γ-decays from excited states E_i within an excitation energy bin i down to the ground state. Let us consider the simplified level scheme involving three excited states E_1, E_2, E_3 and the ground state E_0 (see Figure.5.2). One could build up a simplified matrix containing the corresponding γ-ray spectra for each excitation energy of a nucleus. Gating on the highest excitation energy E_3 would reveal 6 different full energy peaks from the γ-rays emitted in four possible decay chains from the excited state E_3 to the ground state. By gating on the lower-lying E_2 state, only three full energy peaks from two distinct decay paths will be observed. Finally, only one γ-transition would yield deexcitation from the lowest E_1 state to the ground state. The primary transitions from each state could be also denoted as the first-generation γ-rays. In the scope of the present project, the main goal is to extract the level density and the γ-strength function determined by the distribution of these first-generation γ-rays. Therefore, an additional step is to be performed to transform the obtained matrix $U(E_x, E_\gamma)$ into the first generation matrix $\mathscr{P}(E_x, E_\gamma)$.

This step is performed with the extraction procedure proposed by M. Guttormsen *et al.* in [138]. The major assumption to be fulfilled for this method to be applicable is that an excited state, populated in preceding γ-transitions, has the same decay properties as the same excited state, populated directly in a particle induced reaction. This assumption seems to hold for most of the range of excitation energy, except for the very low energies [139]. As seen from the example in Figure.5.2, the cascades towards the ground state originating from E_2 and E_1 contain the secondary and tertiary transitions from the initial E_3 state. If all the cascades from E_2 and E_1 are subtracted from the E_3-originating cascades, the primary γ-rays in these cascades could be extracted.

This simple procedure forms the core of the first-generation method. The unfolded spectra $U(i)$ contain all possible γ-transitions from the excited states E_i within the excitation energy

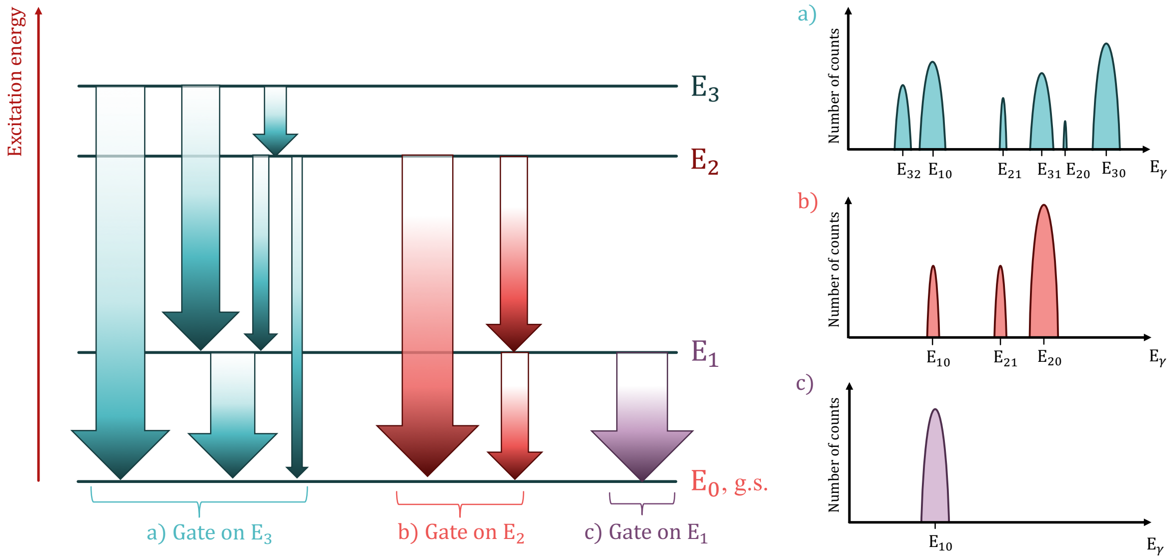

Figure 5.2: Schematic representation of various cascades, originating from three excited states, and the corresponding spectra, obtained by gating on each state.

bin i to the lower-lying excited states and the ground state. The spectrum with $U(i-1)$ contains the same γ-transitions, except for the primary transitions of $U(i)$. The primary γ-ray spectrum $H(i)$ is, thus, formed in a subtraction of the weighted spectra $U(j)$ for $j < i$ denoted by $G(i)$ from the given unfolded spectrum $U(i)$ [138]:

$$H(i) = U(i) - G(i) = U(i) - \sum_{j<i} n_j w_j U(j), \tag{5.13}$$

here, n_j are the correction factors taking into account the difference in cross-sections for the excited states within the energy bins i and j to be populated. The additional weighting coefficients w_j take into account the γ-energy dependent branching ratios for each excitation energy bin. In other words, they represent the probability of a decay from the states within the i-th bin to the states in lower-lying bins, or the distribution of branching ratios for a given bin i over the considered range of γ-energies.

The n_j correction coefficients are primarily defined to have the following property: the area under the spectrum $U(j)$ multiplied by n_j matches the same number of cascades [138]. These coefficients could be experimentally determined via two different procedures:

1. Singles normalization. The singles spectrum obtained with the particle telescopes represent the number of counts per an excitation energy bin E_i, *i.e.* the number of events in which the excited states in this bin were populated. This value is denoted by $S(i)$; it is proportional to both the cross-section of this energy bin to be populated and the number of decay cascades originating from it. Therefore, the n_j coefficients are calculated as:

$$n_j = \frac{S(i)}{S(j)}, \tag{5.14}$$

   where $S(i)$ and $S(j)$ are experimentally the measured cross-sections, which might be expressed in terms of the numbers of counts for the excitation energy bins i and j.

2. Multiplicity normalization [140]. This method exploits the average γ-ray multiplicity $\langle M_i \rangle$ for each excitation energy bin i. If an excited state E_i is populated N times during an experiment, this would eventually result in N γ-cascades towards the ground state. The average γ-energy in these cascades could be written as $\langle E_\gamma^i \rangle$ and should be related to the total energy carried by photons NE_i and multiplicities for all the cascades M_i^l in the following way:

$$\langle E_\gamma^i \rangle = \frac{NE_i}{\sum_l^N M_i^l}, \tag{5.15}$$

hence, the average multiplicity for each bin i is given by:

$$\langle M_i \rangle = \frac{1}{N} \sum_l^N M_i^l = \frac{E_i}{\langle E_\gamma^i \rangle}. \tag{5.16}$$

The singles-particle cross-section fraction for two energy bins i and j could be easily found: each cross-section is proportional to the total number of counts in the corresponding spectrum divided by the average γ-multiplicity $U(i)/\langle M_i \rangle$. In turn, the total number of counts is proportional to the area of the corresponding spectrum, which we would denoted by $A(U(i))$. Given all the proportionalities, the correction coefficients n_j will be defined as:

$$n_j = \frac{A(U(i))/\langle M_i \rangle}{A(U(j))/\langle M_j \rangle} = \frac{A(U(i))\langle M_j \rangle}{A(U(j))\langle M_i \rangle}. \tag{5.17}$$

Both the singles and multiplicity normalization methods give similar results within the experimental error bars as shown in [139]. However, the presence of long lived isomeric states could distort the final result, obtained with the singles normalization method. The γ-rays, stemming from the isomeric states, are emitted within the larger time scales than the narrow primary time gate, and they will not be detected in a coincidence with a corresponding particle. On the other hand, the unfolded matrix allows to obtain easily all the variables needed for the multiplicity normalization method; for the sake of simplicity, it was decided to exploit the latter method in the present analysis.

Another set of parameters to be determined is the w_j factors, normalized as $\sum_j w_j = 1$. These factors contain information on the branching ratios within a certain energy bin and correspond directly to the primary spectrum $H(i)$. As shown in [138], the choice of a trial function, describing these factors, does not affect dramatically the shape of the primary spectra, but could result in significantly different spectrum areas for different coefficients chosen.

In the ideal case, the w_j factors are chosen properly, and the total area of the primary spectrum $A(H(i))$ should be equal to the difference between $A(U(i))$ and $A(G(i))$. Practically, deviations might occur due to imperfections in a choice of the w_j factors. It is often convenient to introduce an additional area correction procedure. A correction factor α_i is introduced in order to adjust the difference between two areas so that:

$$A(H(i)) = A(U(i)) - \alpha_i A(G(i)). \tag{5.18}$$

On the other hand, the unfolded spectrum $U(i)$ contains on average $\langle M_i \rangle$ decay cascades and, thus, first generation transitions, and the area of $H(i)$ could be expressed as:

$$A(H(i)) = \frac{A(U(i))}{\langle M_i \rangle}. \tag{5.19}$$

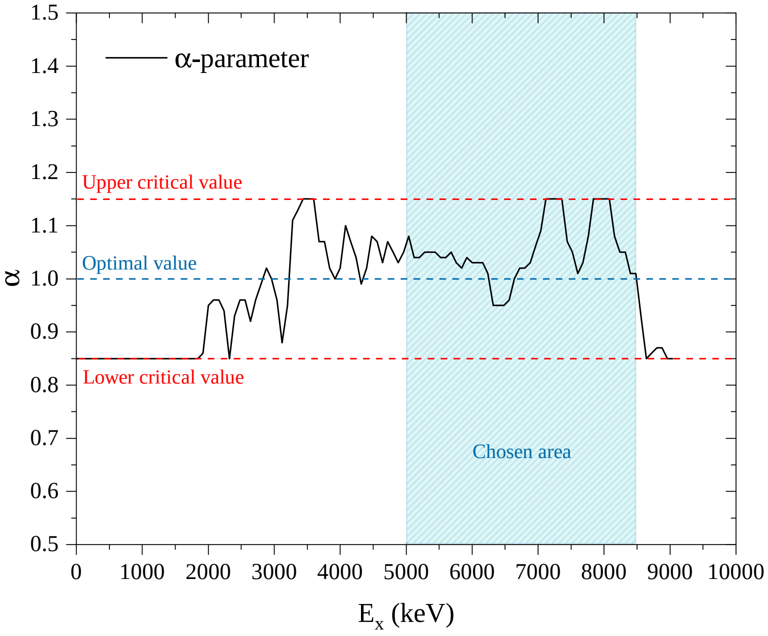

Figure 5.3: The α-correction factor, plotted as a function of excitation energy for ^{124}Sn. The optimal and critical values are marked with the blue and red dashed lines correspondingly.

This could be used to extract the correction factor α, given by:

$$\alpha_i = \left(1 - \frac{1}{\langle M_i \rangle}\right) \frac{A(U(i))}{A(G(i))}. \tag{5.20}$$

This correction is assumed to be reasonable if lying within the range of $0.85 < \alpha < 1.15$. Otherwise, the choice of the weighting factors w_j is inappropriate and should be modified. The correct factors could be found in the iterative routine implemented in the Oslo method software package. Due to direct the relation of w_j and the primary spectrum $H(i)$, the iterative procedure is presented by the following steps:

1. The trial function for w_j is chosen: the unfolded spectrum $U(i)$, a theoretical estimate or a simple constant function could be used.

2. The first primary spectrum $H(i)$ is deduced by implementing these coefficients in the Equation 5.13.

3. The new w_j^{new} is extracted by normalizing the area of H_i to 1 and applying the same energy calibration to $H(i)$ as for w_j.

4. The new w_j^{new} is compared with the trial function w_j: if an approximate equality is reached for $w_j^{new} \approx w_j$, the new function is kept; otherwise the steps 2-4 are repeated.

This iterative procedure was shown to be converging fast: for an arbitrary choice of the w_j (*e.g.* constant function of γ-energy), three iterations were sufficient to reach a good agreement with the correct spectrum within the experimental errors [138]. In general, 10-20 iterations are recommended [139]. The area check is performed in each iteration step, and the result of the procedure is reliable as long as the correction coefficient α lies in the vicinity of $\alpha = 1$ for a

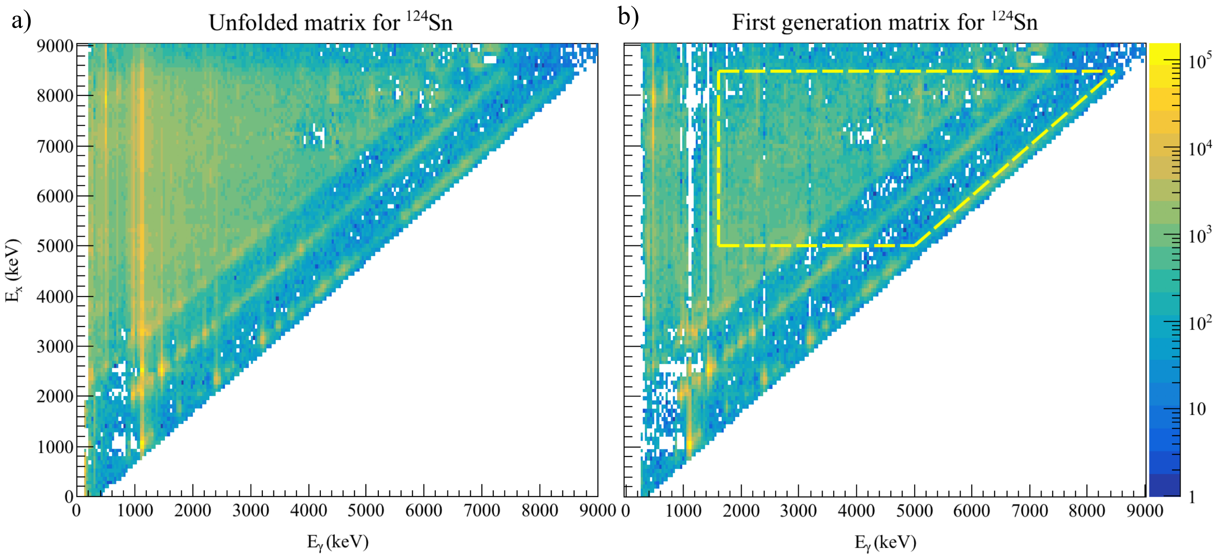

Figure 5.4: a) The unfolded coincidence matrix for ^{124}Sn(p, p' γ)^{124}Sn reaction, obtained after the folding iteration method and the Compton subtraction method. **b)** The first-generation matrix, obtained in the first-generation method for the unfolded coincidence matrix. Yellow dashed lines confine the region chosen for extraction of nuclear level density and γ-ray strength function.

large range of excitation energies, which can be subsequently used for the level density and γ -ray strength function extraction.

A study of the area correction parameter was carried out to define the lower limit of the excitation energy range for the present analysis. The dependence of α on the excitation energy after 20 iterations is shown in Figure 5.3. This dependence does not change significantly for a larger number of iterations. It is shown, that the first-generation method fails for excitation energies lower than $\approx$3000 keV and remains close to the optimal value above 5000 keV. In addition, the transitions between the states at sufficiently low excitation energies could not be treated within the statistical approach and should be excluded.The value of 5000 keV was chosen to be the lower excitation energy limit E_x^{min} for the further analysis. It could also be noticed that certain problems with the method for the 7120-7360 keV and 7840-8080 keV ranges occur. This might be related to artificial fluctuations remaining after eliminating impurities. However, in the mentioned energy gaps α does not exceed 20%, and the iterations are performed without any significant failures. The upper excitation energy limit is set to the neutron separation energy $E_x^{max} = S_n(^{124}\text{Sn})$=8489 keV. Despite the small excitation energy ranges affected by impurities, the rest of the range selected is characterized by the α parameter, lying well within the acceptable limits.

Figure 5.4 represents the unfolded and the first generation matrices obtained from the raw p-γ coincidence matrix with all the procedures described above. In addition to the lower and upper limits of excitation energies, one has to set a lower limit for γ-ray energies. Since the chosen area should not contain any secondary transitions, but should still have sufficient statistics, the lower limit was set to be $E_\gamma^{min} = 1600$ keV. For the excitation energies within the chosen range, the first-generation matrix lacks γ transitions below 1600 keV (empty vertical stripes) due to an over-subtraction of strongly populated states in the unfolded matrix (yellow vertical lines). The energy ranges E_x^{max}, E_x^{min}, and E_γ^{min} ensure an exclusion of these low-statistics areas. The area selected for the extraction of both the level density and γ-ray strength is shown in Figure 5.4.

5.3 Extraction of the γ-strength function and level density

The application of the procedure described in the previous section results in the distribution of first generation γ-rays for a wide range of excitation energies grouped together as the matrix $\mathscr{P}(E_x, E_\gamma)$. It contains essential information on both the γ-strength function and level density which present the final aim of the whole analysis. The extraction method discussed below is primarily based on Fermi's Golden Rule as the pivotal relation [141, 142]:

$$\lambda_{i\to f} = \frac{2\pi}{\hbar}|\langle f|\hat{H}_{tr}|i\rangle|^2\rho_f. \tag{5.21}$$

The transition, or decay, rate $\lambda_{i\to f}$ (probability of a decay per unit time) is determined by the transition matrix element between the initial i and final states f and the density of final states ρ_f. The major assumption here is that the perturbation due to the transition operator $\hat{H}_{tr}$ is small, which holds true for many nuclear physics applications. This relation will now allow us to consider the following proportionality [143]:

$$\mathscr{P}(E_x, E_\gamma) \propto \mathscr{T}_{i\to f}\rho_f. \tag{5.22}$$

Indeed, the first generation matrix $\mathscr{P}(E_x, E_\gamma)$ is directly proportional to the decay probability, hence, the decay rate $\lambda_{i\to f}$ as well. Here, the transmission coefficient $\mathscr{T}$ would be a function of both initial and final excited states, as the level density ρ_f should be referred to the final excitation energy, also defined as $E_f = E_i - E_\gamma = E_x - E_\gamma$. These functions can be extracted simultaneously, if is no dependence of the transmission coefficient on the initial and final excitation energies. Here, one of the major assumptions in the analysis, the Brink-Axel hypothesis [112, 114], is introduced. According to this hypothesis, the γ-ray strength function is essentially independent on the properties of the initial and final states. As it was mentioned in Section 3.3, it was initially formulated for the IVGDR, which should have the same energy behavior if built on a ground state or one of the excited states. In principle, it has a limited application range. However, it is still widely used as an underlying assumption in the OCL experiment analyses, where it is assumed to hold below the neutron separation energy and the discrete E_x region. This hypothesis eliminates the dependence on E_i and E_f in the transmission coefficient, so that it is transformed into a function of E_γ only:

$$\mathscr{P}(E_x, E_\gamma) \propto \mathscr{T}(E_\gamma)\rho(E_f) = \mathscr{T}(E_\gamma)\rho(E_x - E_\gamma). \tag{5.23}$$

This is the core relation for the extraction procedure, first described by L. Henden in [144]. As was emphasized in [144], such a factorization implies the following for the excitation mechanism to be valid: full thermalization of a nucleus should take place before γ-emission. In other words, Equation 5.23 would hold for the compound state decay, *i.e.* a nucleus is first formed in a compound, or thermalized, state, where energy is redistributed among nucleons, and then decays via the final channel decoupled from the initial formation channel. For relatively high excitation energies, as in the case of the present analysis, it is expected to be the case. Despite the fact, that the states studied are excited in the direct reaction, characterized by the time scale of $\sim 10^{-22}$ s, the following γ-decay takes place within the time gate of 10^{-15} s. The latter provides a considerably larger time scale, as compared to the excitation process, and the excited nucleus could be assumed thermalized prior to the γ-decay.

If the decomposition, given by Equation 5.23, is justified, one could apply the iterative extraction procedure, described in details in [145]; it is based on a χ^2 minimization written as:

$$\chi^2 = \frac{1}{N_{free}} \sum_{E_x=E_x^{min}}^{E_x^{max}} \sum_{E_\gamma=E_\gamma^{min}}^{E_x} \left(\frac{\mathscr{P}_{theor}(E_x, E_\gamma) - \mathscr{P}(E_x, E_\gamma)}{\Delta \mathscr{P}(E_x, E_\gamma)} \right)^2 , \qquad (5.24)$$

here N_{free} indicates the number of degrees of freedom (number of data points in the primary matrix minus data points in the transmission coefficient and level density functions), $\mathscr{P}$ (E_x, E_γ) is the experimentally obtained first-generation matrix with the corresponding uncertainty $\Delta\mathscr{P}(E_x, E_\gamma)$, $\mathscr{P}_{theor}(E_x, E_\gamma)$ is the theoretical estimate calculated with the transmission coefficient $\mathscr{T}(E_\gamma)$ and level density $\rho(E_x - E_\gamma)$. The latter is introduced by the following approximation:

$$\mathscr{P}_{theor}(E_x, E_\gamma) = \frac{\rho(E_x - E_\gamma)\mathscr{T}(E_\gamma)}{\sum_{E_\gamma=E_\gamma^{min}}^{E_x} \rho(E_x - E_\gamma)\mathscr{T}(E_\gamma)}. \qquad (5.25)$$

Before Equation 5.24 is used, the experimental first-generation matrix $\mathscr{P}(E_x, E_\gamma)$ has to be normalized so that the sum over γ-ray energies, running from a certain minimum limit E_γ^{min} up to the maximum energy E_x for a given excitation bin, is equal to 1 [145]:

$$\sum_{E_\gamma=E_\gamma^{min}}^{E_x} \mathscr{P}(E_x, E_\gamma) = 1. \qquad (5.26)$$

After these preparatory steps are performed, one could proceed with the iterative procedure to extract the level density and the transmission coefficient. First, the zeroth-order estimate is calculated by assuming the first trial function for the level density to be $\rho^0 = 1$ and applying it to Equation 5.25. Summing the latter over the excitation energies from E_x^{min} to E_x^{max} and taking into account that $E_\gamma \leq E_x$, one could obtain the zeroth estimate for the transmission coefficient:

$$\mathscr{T}^0(E_\gamma) = \sum_{E_x=max(E_x^{min}, E_\gamma)}^{E_x^{max}} \mathscr{P}(E_x, E_\gamma). \qquad (5.27)$$

These zeroth-order estimates are then used to express the theoretical first-generation matrix $\mathscr{P}^0(E_x, E_\gamma)$ and the corresponding $(\chi^2)_0$, which should be minimized with respect to both variables as:

$$\frac{\partial \chi^2}{\partial \mathscr{T}(E_\gamma)} = 0 \ , \ \frac{\partial \chi^2}{\partial \rho(E_x - E_\gamma)} = 0. \qquad (5.28)$$

This would result in the next order estimates $\mathscr{T}^1(E_\gamma)$ and $\rho^1(E_x - E_\gamma)$, which are used again to calculate $(\chi^2)_1$; the procedure is performed til the $(\chi^2)_n$ reaches its minimum for the certain values of $\mathscr{T}^n(E_\gamma)$ and $\rho^n(E_x - E_\gamma)$.

It has been shown that this iterative procedure is usually converging fast, but in some cases it might yield failure due to a very shallow χ^2 minimum [145]. This implies that an additional limit on the maximum change of $\mathscr{T}^n(E_\gamma)$ and $\rho^n(E_x - E_\gamma)$ in one iteration could be put to improve minimization. This limit depends on the values obtained in the previous iteration, and affects only a few data points in the high energy region. The minimization procedure in the present analysis did not require this limitation, but it might be quite useful for other cases (*e.g.* strongly oscillating data points in the primary matrix).

This fitting procedure, however, does not yield unique solutions for the nuclear level density and the transmission coefficient. As the χ^2 is minimized and the corresponding solutions are found, one could construct an infinite number of different solutions [145], related to the found values of $\mathscr{T}(E_\gamma)$ and $\rho(E_x - E_\gamma)$ as:

$$\begin{aligned} \tilde{\rho}(E_x - E_\gamma) &= Ae^{\alpha(E_x - E_\gamma)}\rho(E_x - E_\gamma), \\ \tilde{\mathscr{T}}(E_\gamma) &= Be^{\alpha E_\gamma}\mathscr{T}(E_\gamma). \end{aligned} \tag{5.29}$$

Both generalized solutions share the same slope parameter α and have individual scaling factors A and B. Therefore, the iterative procedure yields the functional forms of the level density and the transmission coefficient as functions of $E_x - E_\gamma$ and E_γ correspondingly, but their absolute values, giving unique physical solutions in the χ^2 minimization procedure, are still to be constrained by additional theoretically and experimentally estimated parameters.

5.4 Normalization procedure for the level density and γ-ray strength function

As the set of general solutions, given by Equation 5.29, is obtained for the χ^2 minimization, the physical solution should be fixed by determining the unique slope α and scaling parameters A and B. Firstly, the normalization of the level density would allow to determine the parameters α and A. As the slope the same for both the transmission coefficient and level density, the only parameter to be determined is B.

As the first step, known discrete levels measured at low excitation energy and the level density at the neutron separation energy should be used for the level density normalization. The discrete levels measured in various experiments and collected in, *e.g.* [90], could be considered complete only up to a certain excitation energy. Further up, the levels become more densely spaced and the experimental resolution would be insufficient to resolve them. This maximal energy U_{max} corresponds to 2.878 MeV for the particular case of ^{124}Sn [91], therefore, the fitting procedure in the low energy range, exploiting these known states, is valid up to U_{max} only. Since the data points for the level density are measured up to the comparatively higher energy $S_n - E_\gamma^{min}$, another reference point for the normalization is the level density at the neutron separation energy is required. It could be determined on the base of experimental values of average neutron resonance spacing for s-wave neutrons and p-wave neutrons [146], D_0 and D_1 correspondingly. The available experimental information on s-wave neutrons is used for the normalization procedure in the present work.

The average resonance spacing D_0 is directly related to the level density at the neutron separation energy S_n as [139]:

$$\frac{1}{D_0} = \frac{1}{2}\left(\rho(S_n, J = I_t + 1/2) + \rho(S_n, J = I_t - 1/2)\right). \tag{5.30}$$

This expression contains the partial level densities for both spins populated, $J = I_t \pm 1/2$, for a given spin I_t for the target in neutron-capture experiments.The positive and negative parities are assumed to contribute equally to the level density. In order to extract $\rho(S_n)$ from this relation, the general form of the back-shifted Fermi gas formula (see [82]) was adopted:

$$\rho(U, J) = g(J) \cdot \rho(U) = \frac{\sqrt{\pi}}{12}\frac{e^{2\sqrt{aU}}}{\sqrt{2\pi}\sigma a^{1/4}U^{5/4}} \cdot \frac{(2J+1)e^{-\frac{(J+1/2)^2}{2\sigma^2}}}{2\sigma^2}, \tag{5.31}$$

here $U = E - E_1$, a and E_1 are the level density and excitation energy back-shift parameters, and σ is the spin-cutoff parameter. The latter factor is generalized for the energy dependence of the spin-cutoff parameter and considered to be the energy dependent spin distribution formula, implemented in the Oslo method software (determined in both [83, 147]):

$$g(E_x, J) = \frac{2J+1}{2\sigma^2(E_x)} e^{-\frac{(J+1/2)^2}{2\sigma^2(E_x)}}. \tag{5.32}$$

Given the BSFG level density in Equation 5.31 and assuming equal contribution from both parities, one could easily deduce the level density at the separation energy:

$$\rho(S_n) = \frac{2\sigma^2}{D_0} \frac{1}{(I_t+1)e^{-(I_t+1)^2/2\sigma^2} + I_t e^{-I_t^2/2\sigma^2}}. \tag{5.33}$$

The problem is now reduced to estimating the D_0 and the spin-cutoff parameter σ. In addition, proper extrapolation of the level density towards the neutron separation energy is required. Here, the constant temperature approach and temperature dependent form of the spin-cutoff are usually used. As already mentioned, there are certain indications from recent level density systematics that the temperature could be considered approximately constant in the energy range between the $E_x \approx 2\Delta$ and the neutron separation energy S_n [75, 148], up to which the pair breaking process takes place. As it was emphasized in the latter work, the constant temperature formula could still be applicable for higher energies as well. Nevertheless, the excitation energy range of interest in the present work is limited by the neutron separation energy. The constant temperature behavior of the level density up to the neutron separation energy, combined with the BSFG spin distribution at the separation energy, serves as the framework in the present study. In order to extract the spin-cutoff parameter $\sigma(E)$, the linear dependence of σ^2 on the nuclear temperature parameter T could be used as described in [83]:

$$\sigma^2 = \Theta T. \tag{5.34}$$

In general, the temperature is excitation-energy dependent. Since the temperature is considered to be constant in the studied range, its value would be fixed. The moment of inertia Θ is model dependent, and several theoretical approaches were tested in the present work. Firstly, there are certain arguments in favor of treating a nucleus as a rigid sphere of radius $R = 1.25A^{1/3}$ [149]. Therefore, the rigid body moment of inertia $\Theta_{rbm} = 0.0146A^{5/3}$ (MeV^{-1}) could be used to calculate the spin-cutoff as proposed in [81]:

$$\sigma^2_{RMI} = \Theta_{RMI} T_{RMI} = 0.0146A^{5/3}\frac{1+\sqrt{1+4aU}}{2a}, \tag{5.35}$$

where a is given by the global fit from [81] and U is given by $S_n - E_1$ at the neutron separation energy. The rigid body approach is, however, able to give solely a crude estimate of the moment of inertia. The level density obtained in this approach would correspond to the upper limit, as the rigid body value represents the maximum value for the moment of inertia.

An alternative model tested in the present work exploits the moment of inertia proposed by A. Gilbert and A. G. W. Cameron [82]:

$$\sigma^2_{G\&C} = \Theta_{G\&C} T_{G\&C} = 0.0888aA^{2/3}\sqrt{\frac{U}{a}}, \tag{5.36}$$

where a is again taken from [81] and $U = S_n - E_1$. The spin-cutoff parameter estimated with this approach is noticeably smaller than the estimate for the rigid body model. Both approaches were applied for previous OCL experiments, and were chosen to set the lower and upper limits

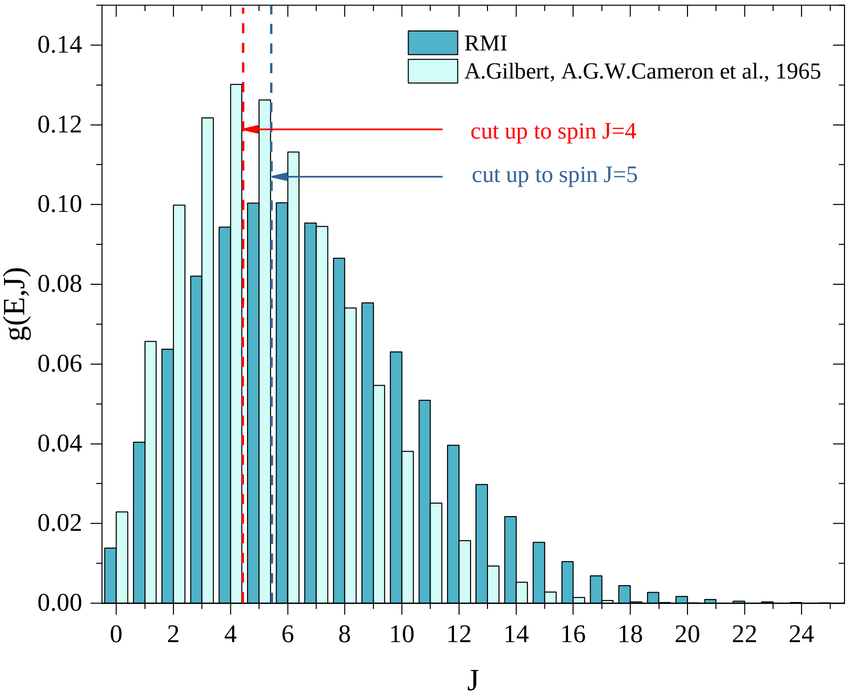

Figure 5.5: Theoretical spin distribution for the rigid body spin-cutoff parameter (RMI) and the spin-cutoff parameter obtained with the Gilbert and Cameron approach. Two spin cuts are depicted by the red and blue dashed lines.

for the level density in the present work.

To sum up all the steps required for the level density normalization, the discrete level scheme for the low energy region, the $\rho(S_n)$ value and the constant temperature level density approach for interpolation between the data points and $\rho(S_n)$ are combined to estimate the slope α and factor A for the level density. The model dependent spin-cutoff σ^2 is calculated to serve as the input for Equation 5.33. The latter provides an estimate for the $\rho(S_n)$ for a given target spin and experimentally constrained resonance spacing D_0 from neutron capture experiments.

An additional nuance should be taken into account while estimating the level density at the neutron separation energy. The beam type and energy selected for the experiment were found to yield only a limited range of spins for the excited states. Previous experiments for similar proton beam energies (from 6 to 24 MeV) have revealed that the highest spin observed is $J = 4$ (see [90] for a list of references). Higher spins are characterized by an uncertain spin and parity attribution. Therefore, for the present work it was assumed two separate approaches for the spins populated: the first approach implies a maximum spin populated to be $J_{max} = 4$, the second would correspond to $J_{max} = 5$. A semi-classical estimate confirms the value of maximum spin between these two values for 16 MeV proton beam for 126°-140°, fixed by the SiRi telescope.

The limited range of spins populated in the (p,p$'\gamma$) reaction dramatically affects the slope of the level density. In order to account for this limitation, the spin distributions in the form of Equation 5.32 were considered for σ^2_{RMI} and $\sigma^2_{G\&C}$. Due to the different moments of inertia and temperature formulas, these spin-cutoff parameters yield different spin distributions (see Figure 5.5). Given these distributions, one might estimate the relative probability for spins up to $J_{max} = 4, 5$ to be populated by considering the theoretical fraction:

$$\eta = \frac{\int_{J=0}^{J_{max}=4(5)} g(S_n, J)dJ}{\int_{J=0}^{\infty} g(S_n, J)dJ}, \tag{5.37}$$

which is practically reduced to summation of $g(E, J)$ over the given range. This fraction is subsequently used to estimate the reduced level density at the neutron separation energy:

$$\rho(S_n)^{red} = \eta\rho(S_n)^{tot}. \tag{5.38}$$

The normalization of the level density would automatically yield the slope parameter α for the transmission coefficient. However, an absolute value B is still to be determined to fix the scaling for both the transmission coefficient and the γ-ray strength function. The scaling parameter B could be directly obtained from a known (or estimated) average, total radiative width $\langle\Gamma_\gamma\rangle$ from s-wave neutron capture experiments. In general, it is an excitation energy, spin and parity dependent quantity $\langle\Gamma_\gamma(E_x, J, \pi)\rangle$. In the general form it is written as [100]:

$$\langle\Gamma_\gamma(E_x, J, \pi)\rangle = \frac{1}{2\pi\rho(E_x, J, \pi)} \sum_{XL} \sum_{J_f,\pi_f} \int_{E_\gamma=0}^{E_x} dE_\gamma \mathscr{T}(E_\gamma)\rho(E_x - E_\gamma, J_f, \pi_f). \tag{5.39}$$

The scope of the present work exploits the average total radiative width at the neutron separation energy $\langle\Gamma_\gamma(S_n, I_f, \pi_f)\rangle$ for the s-wave capture resonances with the accessible spins $I_f = I_t \pm 1/2$ (see *e.g.* [91]). Assuming that both parities contribute equally to the level density under the integral sign and the spin distribution, given by Equation 5.32, one could eliminate dependence on the final spin and parity. The remaining level density at the neutron separation energy in the denominator could be directly calculated with experimental values of D_0 as $\rho(S_n, I_t \pm 1/2, \pi) = 1/D_0$. Finally, the summation over all multipolarities could be reduced to $XL = E1 + M1$, since dipole modes would yield the major contribution to both the transmission coefficient and strength in the studied energy range. The modified expression for the radiative width could be expressed as [150]:

$$\begin{aligned} \langle\Gamma_\gamma(S_n, I_t \pm 1/2, \pi_f)\rangle = \frac{D_0}{4\pi} \int_0^{S_n} & dE_\gamma \mathscr{T}(E_\gamma)\rho(S_n - E_\gamma)\times \\ & \times \sum_{J=-1}^{1} g(S_n - E_\gamma, I_t \pm 1/2 + J). \end{aligned} \tag{5.40}$$

This expression is partially experimentally constrained and partially model dependent (mainly due to the form of the spin distribution and its components).

So far, all necessary relations required for the normalization procedure, have been established and discussed. The experimental values for D_0 and $\langle\Gamma_\gamma\rangle$, if available for a given nucleus, constrain the physical solutions for the level density and γ-ray strength function with accumulated errors due to the statistics, unfolding and the first-generation method procedures and experimental uncertainties for D_0 and $\langle\Gamma_\gamma\rangle$. However, there are no available s- or p-wave neutron capture experimental data on ^{124}Sn as the target nucleus ^{123}Sn is unstable ($T_{1/2}$ = 129.2 d). All the values required for ^{124}Sn have to be obtained from available systematics for other Sn isotopes. This procedure is described in details in the next chapter together with the results, obtained with all estimated input parameters.

5.5 Test of the Brink-Axel hypothesis

In the scope of the Oslo method, described in the previous sections, the qualitative test of the γ-ray strength function dependency on initial and final excitation energies could be carried out. The relevant procedure was outlined in detail in [115]. The starting point of this study refers back to the proportionality established in Equation 5.22. The assumption on the transmission coefficient being dependent on the γ-energy only is still kept, and Equation 5.41 could be rewritten as:

$$N(E_i)\mathscr{P}(E_i, E_\gamma) = \mathscr{T}(E_\gamma)\rho(E_i - E_\gamma), \tag{5.41}$$

where $N(E_i)$ is the normalization factor solely depending on the γ-ray energy. Integration with respect to all E_γ yields the following form of the normalization $N(E_i)$:

$$N(E_i) = \frac{\int_0^{E_i} \mathscr{T}(E_\gamma)\rho(E_i - E_\gamma)dE_\gamma}{\int_0^{E_i} \mathscr{P}(E_i, E_\gamma)dE_\gamma}. \tag{5.42}$$

Here, $\rho(E_i - E_\gamma)$ is the level density obtained with the standard Oslo method. This implies that the transmission coefficient, as well as the γ-ray strength function, could be studied for each excitation energy bin E_i as a function of E_γ energy:

$$\mathscr{T}(E_i, E_\gamma) = \frac{N(E_i)\mathscr{P}(E_i, E_\gamma)}{\rho(E_i - E_\gamma)}. \tag{5.43}$$

This form provides an explicit study of the transmission coefficient for different initial energies transitions take place from. By analogy with Equation 5.43, the transmission coefficient could be rewritten as:

$$\mathscr{T}(E_f, E_\gamma) = \frac{N(E_f + E_\gamma)\mathscr{P}(E_f + E_\gamma, E_\gamma)}{\rho(E_f)}. \tag{5.44}$$

Application of this relation results in a set of transmission coefficients, involving transitions to a chosen final state E_f. The transitions to the ground state and the first excited state in ^{124}Sn are of particular interest for the comparison with external experimental strengths in the present thesis. This type of study is still model dependent due to assumption on the transmission coefficients $\mathscr{T}(E_i, E_\gamma)$ and $\mathscr{T}(E_f, E_\gamma)$, fluctuating with respect to the standard Oslo method transmission coefficients. In addition, the normalization factor might yield slightly different absolute values of the γ-ray strength functions as compared to the standard one. Nevertheless, this approach was shown to provide a qualitatively good study on the validity of the Brink-Axel hypothesis (see *e.g* [115]).

Chapter 6

Experimental results

The previous chapter was mainly devoted to the description of all procedures, leading from the raw p-γ coincidence matrix, obtained in (p,p$'\gamma$) experiment on the ^{124}Sn target, up to the final results on the nuclear level density and γ-ray strength function. The study of the latter is the primary goal of the present work: it allows us to trace the presence of the PDR in a response of the ^{124}Sn isotope and extract all bulk characteristics of this resonance mode. Together with the characteristics of lighter Sn isotopes, previously measured at the OCL, an extended systematic study of the PDR will be provided. The following Section 6.1 is devoted to the procedure of collecting the parameters, required for the normalization of both the nuclear level density and γ-strength function (called from now on γRSF for short).The inherited uncertainty for both values due uncertainties in the parameter estimation will be discussed together with the final results in Section 6.2 and Section 6.3. The parameters of all observed features in the nuclear response from $E_\gamma = 0 - 18$ MeV are presented and discussed in Section 6.4.

6.1 Extraction of parameters for the normalization procedure

As it was mentioned in the previous chapter, one of the final steps of the Oslo method implies extraction of the nuclear level density and γRSF parameters, partially constrained with the different model approaches, partially extracted in neutron resonance experiments. Unfortunately, the experimental values of the level spacing parameter, required to define the level density at the neutron separation energy (see Eqiation 5.33), is not available for even-even Sn isotopes, heavier than ^{120}Sn. Therefore, an additional extrapolation towards ^{124}Sn should be performed.

Figire 6.1 shows the systematics for the level density at the neutron separation energy for even-even Sn isotopes with $A = 114, 116, 118$ and 120 and even-odd Sn isotopes with $A = 113, 115, ..., 125$. Fortunately, there is sufficient information on experimental level spacing parameters D_0 to reveal two trends for even-even and odd-even isotopes separately. The level densities $\rho(S_n)$ were calculated with the experimental values of D_0 and spin-cutoff parameters, defined in the rigid body (marked as RMI for short, Equation 5.35) and Gilbert and Cameron (G&C, Equation 5.36) approaches. As it was mentioned in Section 5.4, the former approach would correspond to the upper limit of both the spin-cutoff and level density at the neutron separation energy. In contrary, the latter would yield the corresponding lower limits. The experimental values of D_0 were taken from the updated version of the atlas of neutron resonances [151] (data points for $\rho(S_n)$, denoted by Mughabghab) as well as the RIPL-3 library [91] (RIPL-3 black data points). It was found that the values coincide in majority of cases, but the latter library is less complete. Therefore, it was decided to focus on the level densities, obtained with the D_0 values from Mughabghab library. Alongside these semi-experimental values, purely theoretical predictions in the framework of the BSFG model are presented in Figure 6.1.

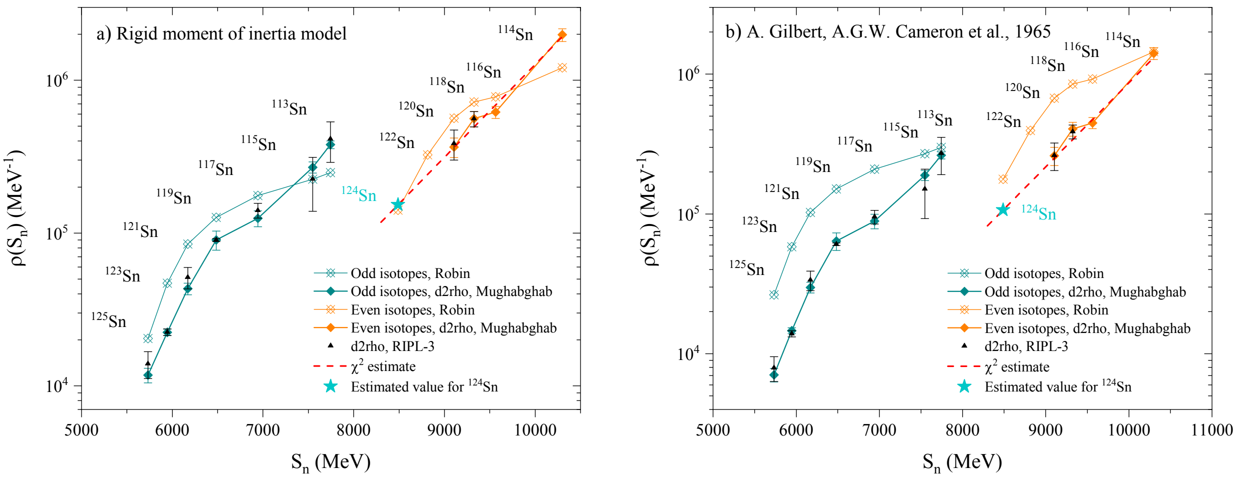

Figure 6.1: a) Experimental systematics for the level density at the neutron separation energy S_n for even-odd and even-even Sn isotopes, plotted together with the theoretical predictions with the rigid body approach. **b)** The same systematics, based on the Gilbert and Cameron approach. The values theoretically predicted with the BSFG model are denoted as "Robin" values. The level densities, obtained with the experimental values of level spacing parameters D_0a and corresponding theoretically predicted spin-cutoff parameters are denoted by d2rho.

Table 6.1: The parameters fixed for all further calculations: the level density parameter a and the energy back-shift E_1 are taken from the interpolations in [81], temperature parameter is estimated with the corresponding T formulas in [81] and [82].

Model	a (MeV^{-1})	E_1 (MeV)	T (MeV)
RMI	12.922	1.031	0.799
G&C	12.922	1.031	0.759

These values were obtained with the ROBIN code in the Oslo method software and marked as "Robin"[134]. In overall, they are able to reproduce similar trends, but deviate significantly in the absolute value, especially in the Gilbert and Cameron approach. The estimate of the level density in ^{124}Sn could be performed with the linear regression for available even-even Sn isotopes and subsequent extrapolation towards $A = 124$. Unfortunately, even though the experimental errors are small for even-even isotopes, such an extrapolation yields unreasonably large errors for $\rho(S_n)$ in ^{124}Sn. Attempts to find a scaling parameter for the theoretical Robin values in the χ^2 minimization procedure yielded the errors of the same order of magnitude, as in the previous approach. Therefore, the linear fit of all available $\rho(S_n)$ values was performed. The trend for even-odd isotopes is decoupled from that for even-even isotopes. Therefore, the values of binding energies for $^{113,115,\ldots,125}$Sn were corrected for the corresponding Δ_n gap parameters [152] to unite both trends. This procedure allowed to extract the $\rho(S_n)$ for the ^{124}Sn isotope with large, but more reasonable uncertainties. These uncertainties do not deteriorate the final extracted level density, since the latter is fitted to both the known levels and the constant temperature predictions throughout the whole energy range the data are available for. In this sense, the level density is partially fixed, and if the $\rho(S_n)$ value deviates from the estimated one towards the upper or the lower limits set by the error bars, the significant deviation from the set temperature behavior will be observed. The data points, obtained in the interpolation, together with the interpolation, drawn for the even-even isotope energy range, are marked with light blue stars and red dashed lines in Figure 6.1.

Table 6.2: The calculated estimates for the spin-cutoff parameter σ, resonance level spacing D_0 and the level density $\rho(S_n)$ for the RMI, average and G&C approaches. The reduced level densities are provided for two different spin distribution limits $J_{max} = 4$ and J_{max}=5.

Model	$\sigma(S_n)$	D_0 (eV)	$\rho(S_n)^{tot} \cdot 10^4$ (MeV^{-1})	η_4	$\rho(S_n)^{red}_4 \cdot 10^4$ (MeV^{-1})	η_5	$\rho(S_n)^{red}_5 \cdot 10^4$ (MeV^{-1})
RMI	5.99	65.75	15.16(1114)	0.29	4.46(327)	0.39	5.98(439)
Average	5.36	72.10	12.54(681)	–	4.33(233)	–	5.70(233)
G&C	4.67	84.25	9.92(784)	0.42	4.19(331)	0.55	5.42(428)

Table 6.1 shows the parameters (level density parameter a, energy back-shift E_1, and temperature T, applied for two theoretical frameworks: the RMI and G&C. The first two values were used to estimate the temperature and the spin-cutoff parameter. Since the RMI presents the extreme case of a nucleus treated as the rigid body, the G&C yields a significantly smaller moment of inertia, and it is reasonable to introduce a certain in-between approach to the nuclear level density. The principal aim of this step was to obtain more moderate values of the level density, limited by the RMI and G&C approaches, as well as other "averaged"quantities, used in the Oslo method software. The level density at the separation energy for this averaged approach was estimated as:

$$\rho_{avg}(S_n) = \frac{1}{2}[\rho_{RMI}(S_n) + \rho_{G\&C}(S_n)]. \tag{6.1}$$

For the estimation of the spin-cutoff parameter for the averaged value, an additional reduction factor $\alpha = 0.8$ was introduced to reduce the rigid body moment of inertia to some extent as compared to the RMI. This moment of inertia corresponds approximately to the averaged value between the RMI and G&C. The same temperature formula as for the RMI was used to estimate T_{avg}= 0,799 MeV. As the level densities at the neutron separation energy and the spin-cutoff parameters are known for all three approaches, one could also estimate the level spacing parameter D_0 for a neutron capture on unstable ^{123}Sn with $I_t = 5.5$, exploiting Equation 5.33. All parameters used in the present work are presented in Table 6.2. Here, the reduction factors η were taken into account to obtain the reduced level densities for RMI and G&C for two cases of maximum spin populated: $J = 4$ with η_4 and $J = 5$ with η_5 (see Equation 5.37 and 5.38). The reduction of initially different total level densities for RMI and G&C with the corresponding factors leads to quite close values of $\rho(S_n)^{red}$. It is important to emphasize, that the average estimations correspond to the averaged moments of inertia, approximately the averaged spin-cutoff parameters, and the level densities at the separation energy. The large errors for the RMI and G&C approaches yield $\approx 50\%$ final errors for the averaged level densities $\rho(S_n)$ for both spin distribution cuts. This is an appropriate order of error, often used in the analyses of OCL experiments (see *e.g* [153]). Estimation of an averaged and two limit level densities allows us to include an additional systematic uncertainty due to the spread of $\rho(S_n)$ values. This component of the total error will be discussed in the following section.

The discrete levels and estimated values of the level densities at the neutron separation energies for all approaches were used to set the absolute values A and slopes α, shared by the solutions of the χ^2 minimization procedure described in Section 5.3. The only unknown left is the scaling parameter B for the transmission coefficient. According to Equation 5.40, it could be estimated by dividing the known average total radiative width by the value, determined by the integrated product of the unscaled transmission coefficient, level density and spin distribution as well as the resonance spacing D_0. For the case of ^{124}Sn, the experimental value of $\langle\Gamma_\gamma(S_n, I_t \pm 1/2, \pi_f)\rangle$ ($\Gamma_\gamma(S_n)$ for short) is missing and should be estimated anew from systematics.

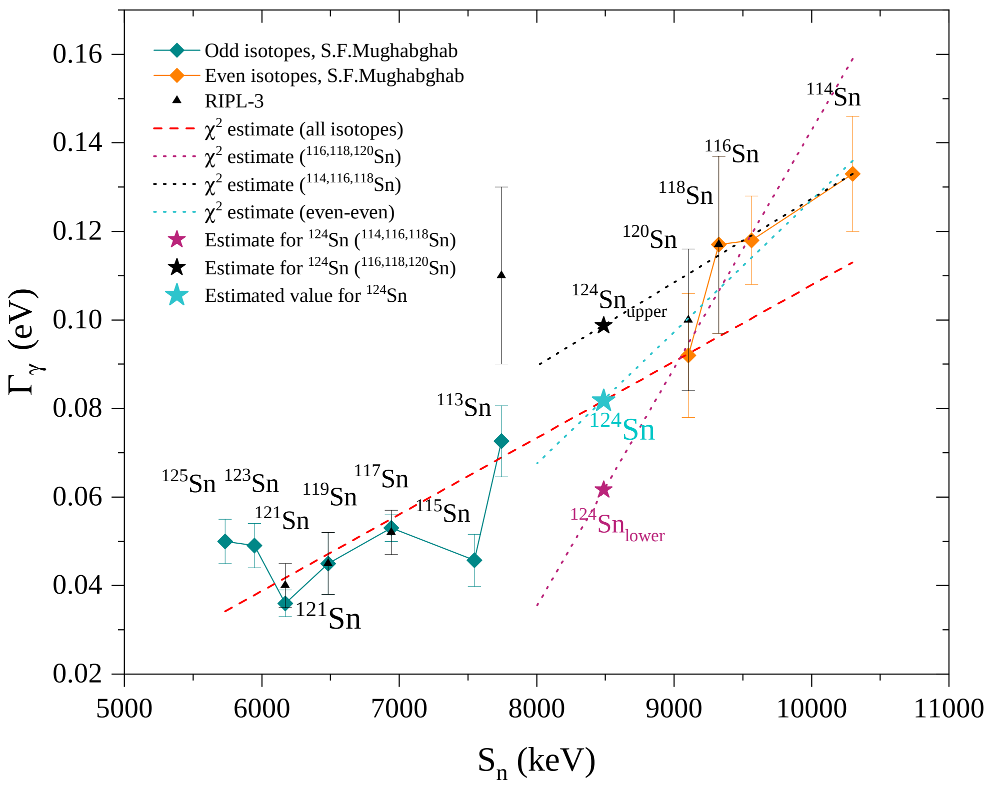

Figure 6.2: The experimental values of the average total radiative widths, [151] and RIPL-3 [91] (not included into analysis. The linear fits of even-even and all isotopes are denoted by the light blue and red dashed lines. Black and magenta dashed lines correspond to the linear fits yielding two extreme values of Γ_γ.

Table 6.3: The interpolated total radiative widths, recommended average, upper and lower limits are included.

Limit	$\Gamma_\gamma(S_n)$ (meV)
Upper	99.54
Average	81.69
Lower	62.11

Figure 6.2 represents the $\Gamma_\gamma(S_n)$ from the neutron resonance capture experiments, taken from the library [151]. There are a few alternative ways to estimate the corresponding value for ^{124}Sn. The first method implies a linear regression, involving $\Gamma_\gamma(S_n)$ for even-even isotopes only. Similarly, a linear regression could be carried out for all Sn isotopes, marked in Figure 6.2. Purely accidental coincidence between the obtained values was observed ($\Gamma_\gamma(S_n) = 81.69$ meV *vs.* $\Gamma_\gamma(S_n) = 82.17$ meV for the linear fit of all Sn isotopes and even-even isotopes correspondingly). For the present work the interpolated value for the fit of all Sn isotopes was chosen as the recommended value. It is important to notice, that the Oslo method based software, used for the analysis, does not include propagation of the error for $\Gamma_\gamma(S_n)$. The uncertainty of the γRSF due to the spread of $\Gamma_\gamma(S_n)$ values should be included explicitly by

estimating the upper and lower limits for this value. The clue for estimation of these limits could be given by the overall trend of $\Gamma_\gamma(S_n)$ for even-even isotopes. The utmost points deviate from the trend set by the rest three experimental points. Therefore, the largest $\Gamma_\gamma(S_n)$ could be obtained from the linear fit of the lightest ^{114,116,118}Sn isotopes, as the lower limit is provided by fitting ^{116,118,120}Sn. The whole procedure yields two almost symmetrical extremes for the recommended $\Gamma_\gamma(S_n)$ values, reported in Table 6.3.

6.2 The nuclear level density

The parameters, described in the previous section, were exploited to extract the set of nuclear level densities for all approaches mentioned and two different spin distribution cuts. The effect of different parameter sets from Table 6.2 is demonstrated by Figure 6.3 a), where three different level densities are plotted for the RMI, average, and G&C models for the corresponding spin distribution cut η_4. The overall trend is similar to that observed for η_5, therefore, only the lowest cut η_4 is shown. The level densities are plotted af the functions of $E_x - E_\gamma$, denoted as the excitation energy E_x from now on for the sake of consistency with the previously published OCL level densities. The lowest part of the level density is set to fit the known levels in the energy range, marked by the arrows in Figure 6.3; the upper arrow corresponds to the maximum energy, for which the level scheme is considered to be complete, $E_{max} = 2.879$ MeV [91]. The high energy part of the level density is set to fit the constant temperature trend of the level density with the slopes, provided in Table 6.2. The temperature parameter $T = 0.8$ MeV for the RMI and averaged model provides a very good fit of experimental data: the experimental points follow closely the CT slope. The picture is somewhat different for the G&C approach. The estimated temperature is slightly lower, and, therefore, the slope observed is slightly steeper that that for, *e.g* the RMI. This results to imperfections of the corresponding fit at ≈ 4.5 MeV. The effect of different spin distribution cuts on the average level density is demonstrated in Figuree 6.3 b). It could be seen that the two cuts η_4 and η_5 yield slightly diverging solutions, whereas the trend set by the total level density at the separation energy demonstrates the less satisfactory fit with the CT line. The effect of the different cuts for the spin distribution will be discussed in the following Chapter 7.

The most prominent discrepancies between three approaches could be observed for the discrete states (g.s. and the first excited state) and the hight energy tails, approaching $\rho(S_n)$. In the high energy region, the RMI indeed corresponds to the upper limit of the level density, whereas the G&C goes somewhat below the average value. This fact could be used to estimate the thickness of the asymmetric systematic error band. The combined errors for the proposed average value could be then represented as:

$$\Delta\rho_{avg} = \rho_{avg}\sqrt{\left(\frac{\Delta\rho_{avg,stat}}{\rho_{avg}}\right)^2 + \left(\frac{\Delta\rho_{avg,syst}}{\rho_{avg}}\right)^2}, \tag{6.2}$$

where $\Delta\rho_{avg,stat}$ are the statistical errors, propagating through the unfolding and first generation procedure together with the extraction of level density via χ^2 minimization, described in great detail in [139]. In principle, the parameters to be varied while estimating different combinations of level densities are σ, D_0, $\rho(S_n)$. All the parameters are tightly related, and one can not distinguish separate errors due to them. The way the systematic errors were included in the present work is based on the following equations:

$$\Delta\rho_{avg}^{upper} = \rho_{avg}\sqrt{\left(\frac{\Delta\rho_{avg,stat}}{\rho_{avg}}\right)^2 + \left(\frac{\rho_{RMI} - \rho_{avg}}{\rho_{avg}}\right)^2}, \tag{6.3}$$

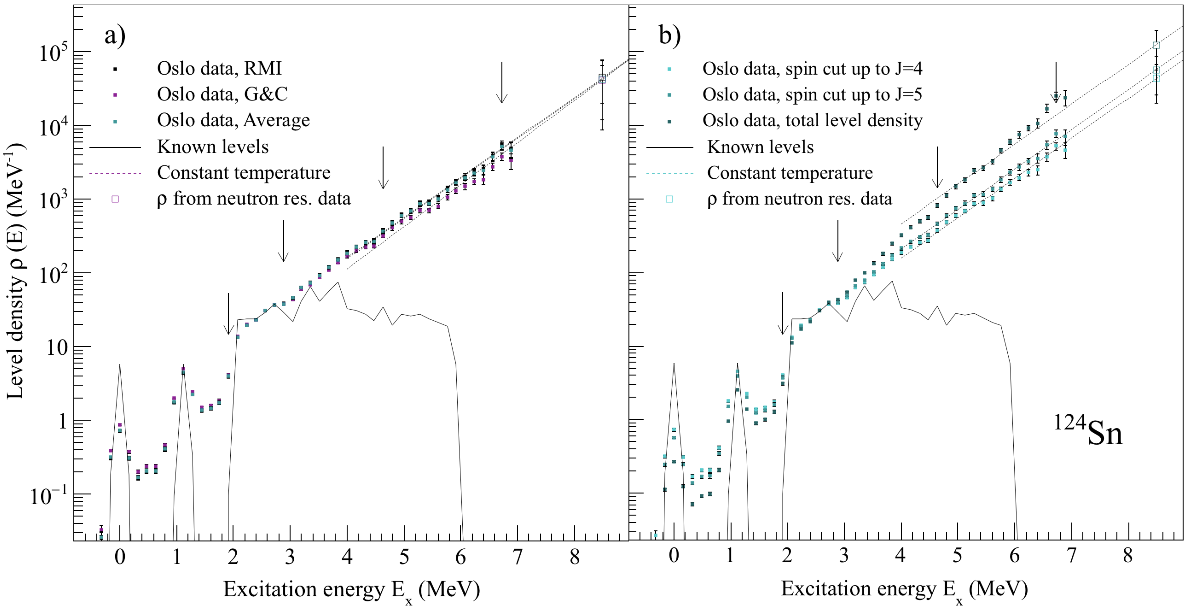

Figure 6.3: a) The calculated level densities obtained with the RMI, average, and G&C approaches. The interpolated values of $\rho(S_n)$ are plotted together with the CT trends with the temperatures fixed and presented in Table 6.2. **b)** The calculated average level densities obtained for the different spin distribution cuts η_4, η_5 and for the total level density $\rho(S_n)$.

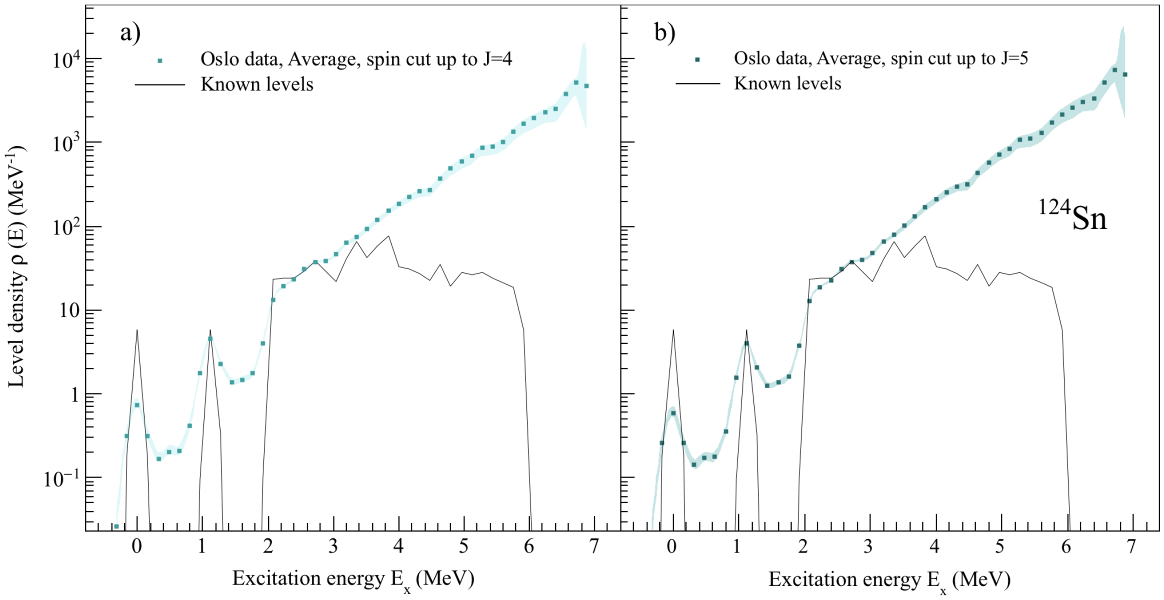

Figure 6.4: a) The calculated level density for η_4 with the total error band due to statistical and systematic errors. **b)** The calculated level density for η_5 with the total error band due to statistical and systematic errors.

$$\Delta\rho_{avg}^{lower} = \rho_{avg}\sqrt{\left(\frac{\Delta\rho_{avg,stat}}{\rho_{avg}}\right)^2 + \left(\frac{\rho_{G\&C}-\rho_{avg}}{\rho_{avg}}\right)^2}. \tag{6.4}$$

Therefore, the final resulting level density could be reported in the following form:

$$\rho_{res}(E_x - E_\gamma) = \rho_{avg}(E_x - E_\gamma)^{+\Delta\rho_{avg}^{upper}(E_x-E_\gamma)}_{+\Delta\rho_{avg}^{lower}(E_x-E_\gamma)}. \tag{6.5}$$

It is interesting to notice, that the RMI level density holds as the upper limit from ≈ 5.5 MeV due to the steeper slope set in this approach. Below this energy the upper limit is defined by the G&C approach, and this fact is taken into account while calculating the error band.

Figures 6.4 a) and b) represent the average level densities for two spin distribution cuts η_4 and η_5 with the corresponding accumulated total error bands. The maximum upper limit of the band (the last high energy data point) reflects ≈ 24% for η_4 and ≈ 29% for η_5, whereas the lower limit indicates ≈ 36% and ≈ 34% correspondingly. Indeed, the discrepancy between the G&C and the average approach is comparatively large, yielding the larger lower error of the level density. The rest of the range is accompanied by more moderate errors for both cases of η_4 and η_5.

6.3 The γ-ray strength function

As the nuclear level density is normalized, it could be used together with other parameters from Table 6.2 and 6.3 to obtain the correct absolute value of the transmission coefficient $\mathscr{T}(E_\gamma)$, sharing the same slope as the nuclear level density. For the further analysis, the transmission coefficient is converted into the γRSF according to:

$$\mathscr{T}(E_\gamma) = 2\pi E_\gamma^3 f(E_\gamma). \tag{6.6}$$

Different nuclear level densities at the neutron separation energy were found to have crucial effect on the slope of the final γRSF, similar to that for the level density. Figure 6.5 a) demonstrates this effect for the γRSF, calculated with the RMI, G&C, and average approaches for η_4. The RMI again corresponds to the upper limit of the γRSF for the energies E_γ above ≈ 5 MeV. For the lower energies the trend set by the RMI goes slightly lower than that for the average γRSF and significantly lower than the G&C strength.

The effect of different slopes due to the different reduced level densities at the neutron separation energy is shown in Figure 6.5 b): the slopes of the γRSF are obtained with $\rho(S_n)_4^{red}$, $\rho(S_n)_5^{red}$, and $\rho(S_n)^{tot}$. Two strengths, based on the reduced level densities, are plotted alongside the strength function for the level density, expected for all spins populated in (p,p$'\gamma$) reaction. As it will be shown in the next section, both reduced level densities lead to the reasonable slopes of the γRSF, giving a good agreement with other experimental data. This agreement is achieved not only within the total error band, but even within the statistical errors only. The total level density leads to the unrealistically steep slope of the strength, deviating greatly from experimental slopes of other strengths it is compared with. These facts imply that the assumption on maximum spin populated in the reaction $J_{max} = 4 - 5$ is quite reasonable.

Despite the spread of the γRSF due to different estimated slopes, the largest contribution to the systematic uncertainty is majorly due to uncertainty in the Γ_γ estimation, which has effect on the scaling of the γRSF. Figure 6.6 represents the example of the average γRSF for η_4 with two purely systematic error bands: a) shows the band due to uncertainty of $\rho(S_n)$, b) corresponds to the band due to the Γ_γ. The latter is more symmetric, as it would be expected from the symmetric Γ_γ limits (see Table 6.3). Here again the average estimate for the γRSF is chosen to be the reference strength function. The total error of the average strength function is estimated in the similar manner as for the level density as:

$$\Delta f_{avg} = f_{avg}\sqrt{\left(\frac{\Delta f_{avg,stat}}{f_{avg}}\right)^2 + \left(\frac{\Delta f_{avg,syst}}{f_{avg}}\right)^2}, \tag{6.7}$$

with the statistical error accumulated throughout the whole Oslo method analysis and the systematic error is now determined as the following combination:

$$\Delta f_{avg}^{upper} = f_{avg}\sqrt{\left(\frac{\Delta f_{avg,stat}}{f_{avg}}\right)^2 + \left(\frac{f_{RMI} - f_{avg}}{f_{avg}}\right)^2 + \left(\frac{f_{upper} - f_{avg}}{f_{avg}}\right)^2}, \tag{6.8}$$

$$\Delta f_{avg}^{lower} = f_{avg}\sqrt{\left(\frac{\Delta f_{avg,stat}}{f_{avg}}\right)^2 + \left(\frac{f_{G\&C} - f_{avg}}{f_{avg}}\right)^2 + \left(\frac{f_{lower} - f_{avg}}{f_{avg}}\right)^2}, \tag{6.9}$$

here f_{upper} indicates the average γRSF scaled with the upper value of Γ_γ, f_{lower} corresponds to the lower Γ_γ. The resulting γRSF could be then reported with the total upper and lower errors as:

$$f_{res}(E_\gamma) = f_{avg}(E_\gamma)^{+\Delta f_{avg}^{upper}(E_\gamma)}_{+\Delta f_{avg}^{lower}(E_\gamma)}. \tag{6.10}$$

Since the steep slope of the level density affects directly the slope of the γRSF, the RMI does not provide the upper limit as one approaches the low values of E_γ. The interchanging character of the RMI and G&C γRSF is taken into account in the error band. Up to this moment the assumption that the spins populated in the reaction do not exceed $J_{max} = 4$ and $J_{max} = 5$ results in two separated solutions for the γRSF with slightly deviating slopes. Both of them are presented together with the corresponding error bands in Figure 6.7. In order to

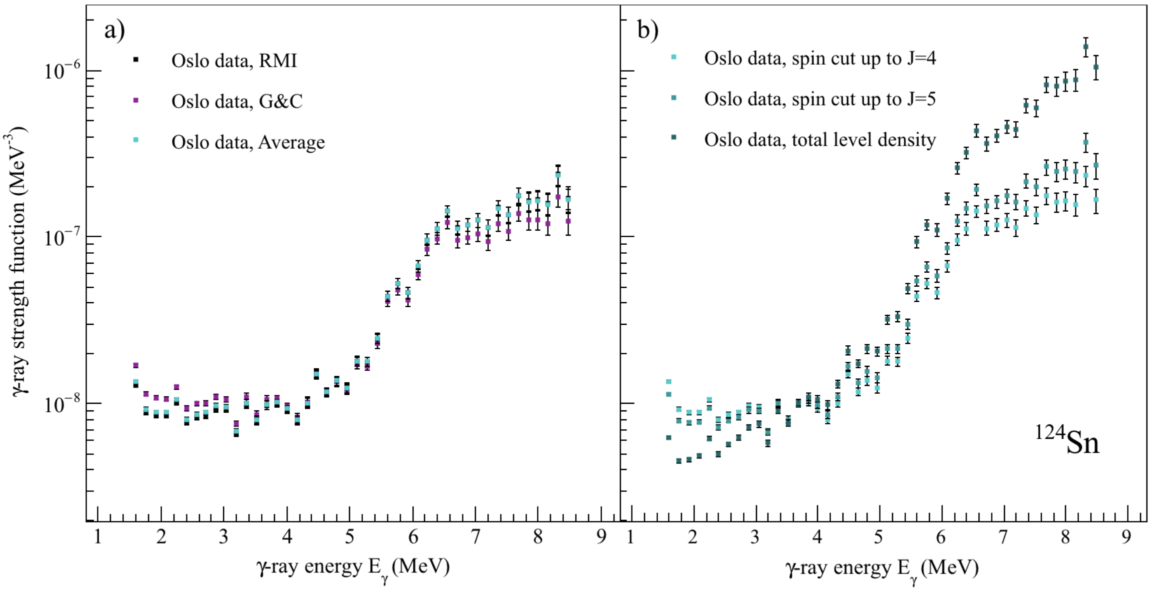

Figure 6.5: **a)** The calculated γRSF obtained with the RMI, average, and G&C approaches, Γ_γ recommended is fixed. **b)** The calculated average γRSF with the fixed recommended Γ_γ, three different spin distribution cuts are plotted.

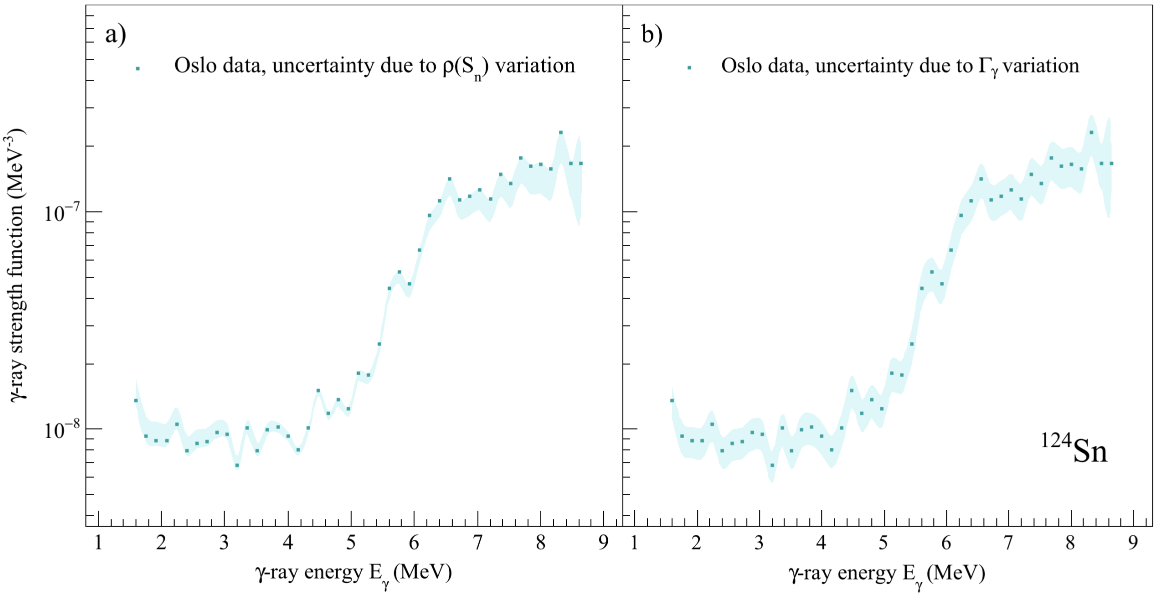

Figure 6.6: a) The extracted γRSF for η_4 with the systematic error band due to $\rho(S_n)$ uncertainty. **b)** The extracted γRSF for η_4 with the systematic error band due to Γ_γ uncertainty.

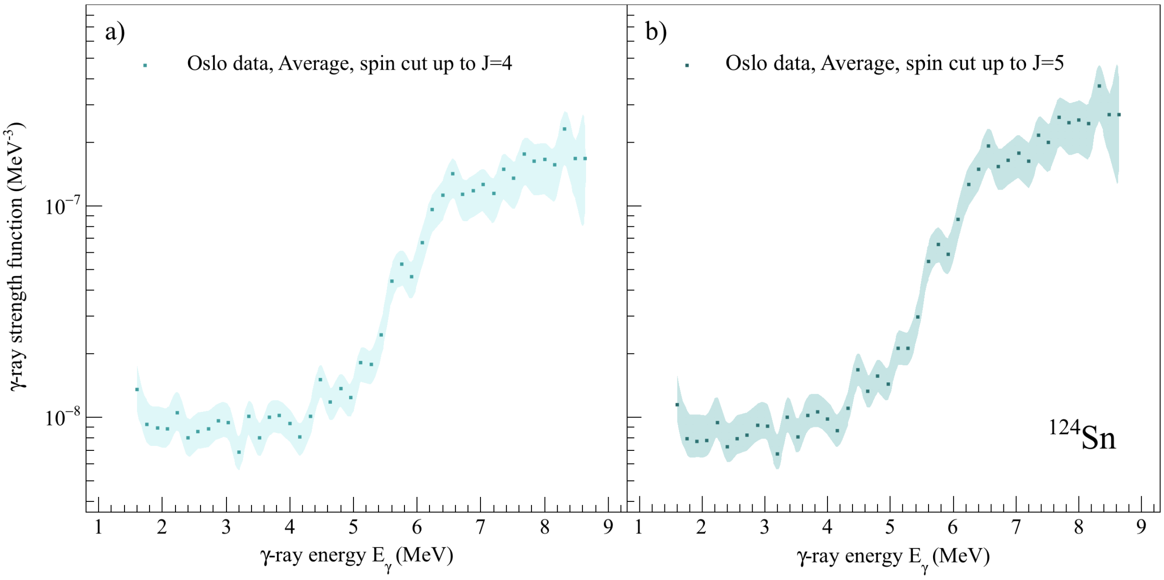

Figure 6.7: a) The final γRSF for η_4 with the total error band due to statistical and systematic errors. **b)** The final γRSF for η_5 with the total error band due to statistical and systematic errors.

give a preference to one of the solutions, both functions should be compared with the available experimental data in the same or adjacent region. This and other arguments for one of the functions will be discussed in the following sections.

6.4 The PDR and other resonances in ^{124}Sn

The γRSF extracted is solely a part of the dipole response of a nucleus, and it could provide valuable information on features of this response only if complemented with the previously measured experimental data for the same and higher-lying energy range. The dominating part of the strength for $E_\gamma > 8$ MeV will be presented by the IVGDR. Indeed, as it can be seen from the the series of the strength functions, extracted from the (γ,n) reactions ([154], [155], [156], [157] in Figures 6.8 and 6.9), the broad IVGDR peak is centered at $\approx$15 MeV. Fortunately, the recent results on the Coulomb excitation of ^{124}Sn in the (p,p$'$) reaction [73], also included in the analysis, cover the larger range from 6 MeV up to highest energies, including the IVGDR. These data overlap partially with the γRSF in the present work, and together with the (γ,n) data from H. Utsunomiya [154] the smooth transition between the PDR and the IVGDR could be observed. The both functions, extracted in the present work, form the very steep left flank of the total strength. In general, a good agreement with [154] and [73] functions could be observed within the estimated error bands for both cases of extracted γRSF. For the case with the spin distribution cut up to $J_{max} = 4$ (Figure 6.8) the γSF sets the slightly lower trend, than the one set by [73]. The opposite picture could be observed for $J_{max} = 5$ (Figure 6.9): the γRSF is slightly higher than the data from the RCNP (p,p$'$) experiment. But in both cases all data points compared are located well within the error band. The only exception is the peak-like structure at $\approx$ 6.5 MeV, which is best reproduced by the γRSF with η_5.

In order to obtain the relevant parametrization of the the PDR in ^{124}Sn one has to perform an accurate global fit of the nuclear response in the available energy range, where the response is expected to be dipole. The most prominent component of the strength function is the IVGDR, providing the baseline for the lower-lying PDR and spin-flip $M1$ resonances, added on top of it. The total γRSF could be represented as following:

$$f_{tot} = f_{IVGDR} + f_{PDR\ 1} + f_{PDR\ 2} + f_{SF} + f_{up}. \tag{6.11}$$

Here an additional component f_{up} is added to account for the flattening of the γRSF in the low-energy range below $E_\gamma \approx 4$ MeV.

Since for the semi-magic ^{124}Sn no double-humped structure of the IVGDR is expected [158], a single-peak function could be sufficient for its description. As it was shown for the lighter Sn isotopes in the OCL experiments (see [21]), the Standard Lorentzian model (SLO) allows to reproduce the IVGDR, but demonstrates a notably unsatisfying behavior of the strength below neutron separation energy. Similar picture was observed for ^{124}Sn, therefore, the Generalized Lorentzian function was chosen to approximate the IVGDR [99]:

$$f_{IVGDR} = f_{E1}^{GLO} = \frac{\sigma_{E1}\Gamma_{E1}}{3\pi^2\hbar^2c^2}\left(\frac{E_\gamma\Gamma_{KMF}(E_\gamma,T_f)}{(E_\gamma^2-E_{E1}^2)^2+E_\gamma^2\Gamma_{KMF}(E_\gamma,T_f)^2}+0.7\frac{\Gamma_{KMF}(E_\gamma=0,T_f)}{E_{E1}^3}\right), \tag{6.12}$$

where $E_{E1} = E_{IVGDR}$ is the resonance centroid (MeV), $\sigma_{E1} = \sigma_{IVGDR}$ defines the peak cross-section (mb), and the temperature dependent width $\Gamma_{KMF}(E_\gamma, T_f)$ is defined according to [98]:

$$\Gamma_{KMF}(E_\gamma,T_f) = \frac{\Gamma_{E1}}{E_{E1}^2}(E_\gamma^2+4\pi^2T_f^2). \tag{6.13}$$

From now on Γ_{E1} is denoted as Γ_{IVGDR}. The resonance centroid, peak cross-section and width were treated as free parameters during the fitting procedure. The temperature parameter T_f was observed to have a strong effect on the total fit (and IVGDR particularly) and its ability to reproduce the low-energy part of the strength. As the γRSF flattens rather than decreases as it approaches E_γ, the temperature has to be large enough to reproduce it. On the other hand,the relatively high temperatures from Table 6.1, while held constant, induce unrealistic overshooting of the strength at $E_\gamma < 6$ MeV. Therefore, the temperature was treated as a free parameter for the following fitting procedures as well.

For the parametrization of the spin-flip $M1$ resonance the $M1$ component of the γRSF from the same (p,p$'$) experiment was chosen [73] . The M1 strength distribution demonstrates two clearly separated peaks (see *e.g* Figure 6.8), and the separate fit of this strength with the composition of two SLO functions was carried out:

$$f_{SF}^{SLO}(E_\gamma) = \frac{1}{3\pi^2\hbar^2c^2}\frac{\sigma_{SF}\Gamma_{SF}^2 E_\gamma}{(E_\gamma^2 - E_{SF}^2)^2 + E_\gamma^2\Gamma_{SF}^2}. \tag{6.14}$$

The total $M1$ strength could be then represented as $f_{M1} = \left(f_{M1}^{SLO}\right)_1 + \left(f_{M1}^{SLO}\right)_2$ with the corresponding parameters attributed to the first and the second peaks. All fit parameters are collected in Table 6.4.

As it can be seen from Figure 6.8, the data points from the RCNP experiment [73] reveal some clear structure at ≈ 6.5 MeV neighboring a broader peak at $\approx$8 MeV. Both the γSFs, extracted in the present work, also contain the similar structure at the same energy of ≈ 6.5 MeV. This feature is less prominent, but it was found, that the better approximation could be obtained if two pygmy structures are included in the total fit. There are several alternative approaches on how the PDR could be fitted. Numerous works suggest the SLO model (see *e.g* [111]), but in the present case the SLO fails completely in simultaneous reproduction of the very steep left flank of the function and its low energy tail. The Gaussian function was applied instead for each PDR:

$$f_{PDR}^{Gauss}(E_\gamma) = C_{PDR}\frac{1}{\sqrt{2\pi}\sigma_{PDR}}e^{-\frac{(E_\gamma - E_{PDR})^2}{2\sigma_{PDR}^2}}. \tag{6.15}$$

The same approach was used in the analysis of $^{116-119,121,122}$Sn isotopes [21]. Finally, the low-energy tail of the γRSF was reproduced as:

$$f_{up}(E_\gamma) = C_{up}e^{-a_{up}E_\gamma}. \tag{6.16}$$

As all the functions of the nuclear response are defined, the total fit with the fixed $M1$ strength could be performed. The parameters for the fitted IVGDR and PRD for the cases of γRSF with the spin distribution cut up to $J_{max} = 4$ and $J_{max} = 5$ could be found in Tables 6.5-6.7. In addition, all the fits are plotted in Figures 6.8 and 6.9 together with the experimental data points. A few strongly deviating data points with the large error bars in [155] (below 10.5 MeV), [157] (below 10.5 MeV), and [156] (below 8.79 MeV) data sets were excluded in order to avoid distortion of the fits. Moreover, while being in a very good agreement in vicinity of the centroid, all (γ,n) data demonstrate divergence from the (p,p$'$) experimental points while approaching the neutron separation energy. The minimizing routine was found to be especially sensitive to this region, and it was decided to choose [154] and [73] to be the reference data in

Table 6.4: Extracted parameters for the $M1$ spin-flip resonance in ^{124}Sn, [73].

E_{SF}^1 (MeV)	Γ_{SF}^1 (MeV)	σ_{SF}^1 (mb)	E_{SF}^2 (MeV)	Γ_{SF}^2 (MeV)	σ_{SF}^2 (mb)
6.92(4)	0.33(10)	1.07(32)	9.66(13)	2.05(22)	2.69(23)

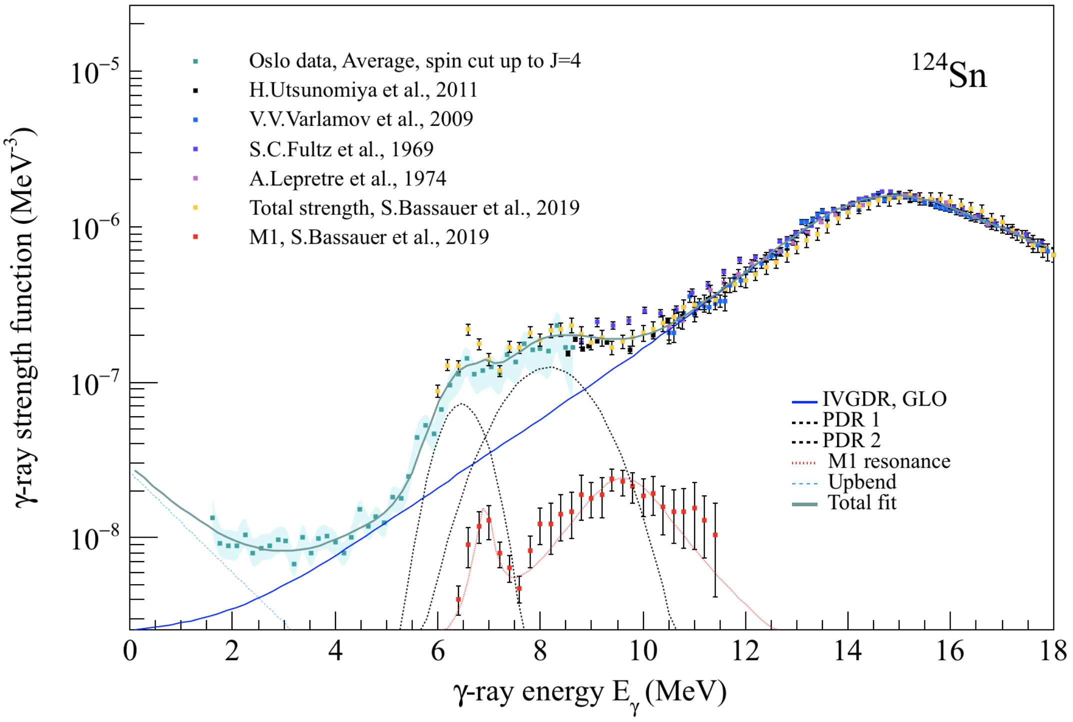

Figure 6.8: Average γRSF for ^{124}Sn with the spin distribution cut $J_{max} = 4$, comparison with the ^{124}Sn(p,p$'$) data from [73] and ^{124}Sn(γ,n) data from references [154], [155], [156], [157]. All fitted structures are marked by solid and dashed lines.

Table 6.5: Parameters for the IVGDR in ^{124}Sn.

Model	E_{IVGDR} (MeV)	Γ_{IVGDR} (MeV)	σ_{IVGDR} (mb)	T (MeV)
Spin distribution cut up to J=4				
Average+GLO	15.54^{+2}_{-2}	5.75^{+16}_{-15}	268.87^{+503}_{-445}	0.33^{+14}_{-12}
G&C+ GLO	15.54^{+2}_{-2}	5.78^{+18}_{-14}	267.80^{+397}_{-577}	0.29^{+14}_{-15}
Spin distribution cut up to J=5				
Average+GLO	15.53^{+2}_{-2}	5.67^{+18}_{-18}	271.47^{+516}_{-525}	0.41^{+16}_{-11}
G&C+ GLO	15.53^{+2}_{-3}	5.66^{+17}_{-19}	271.81^{+537}_{-517}	0.42^{+16}_{-11}

the region between 8.6 MeV (end of the present data) and 10.3 MeV (approximate transition region between the PDR and IVGDR). The main focus was made on achieving the best fit of the IVGDR and the PDR energy range. As it could be seen, a good fit was found for both cases of extracted γRSF, reproducing properly the right and the left flanks of the IVGDR. The steep slope at $\approx$5.5 MeV is also well reproduced. The upbend function, described by Equation 6.16, allowed us to reconstruct the low-energy tail of the strength. If not included, the resulting steeply decreasing strength function would contradict to the low-energy behavior of the experimental strength. As it is shown in Figures 6.8 and 6.9, the simple exponential function 6.16 gives a rather satisfactory fit.

In addition, the similar analysis was carried out for the γRSF corrected with η_4 and η_5 and based on the G&C approach. This corresponds exactly to the model applied to the lighter Sn

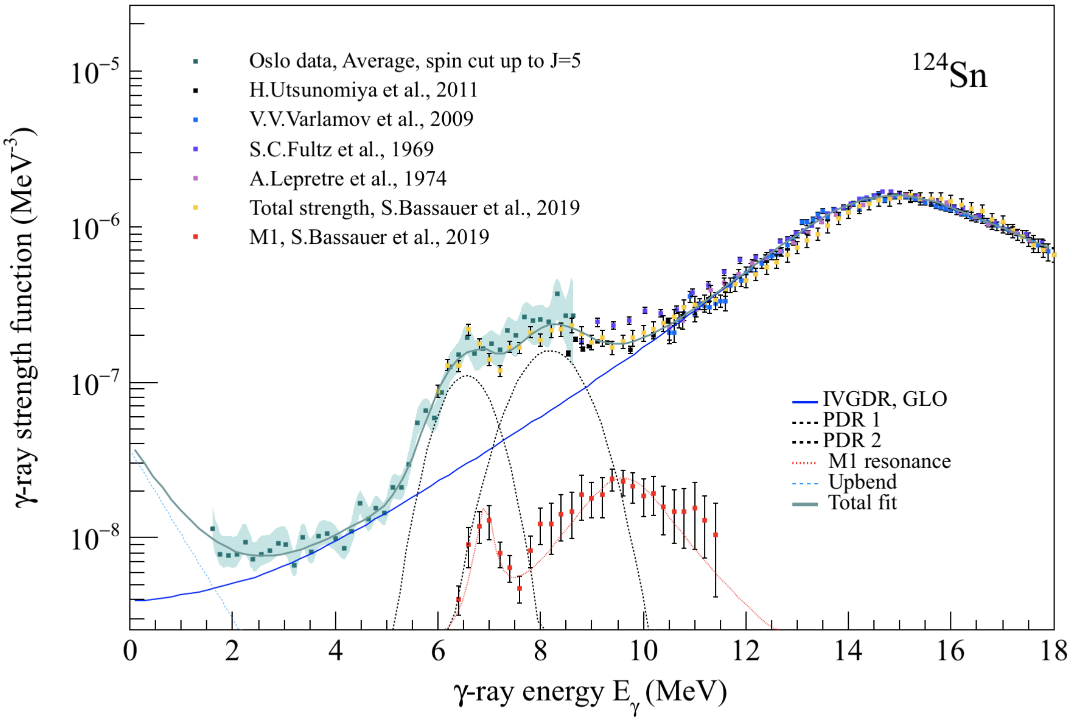

Figure 6.9: Average γRSF for ^{124}Sn with the spin distribution cut $J_{max} = 5$, comparison with the ^{124}Sn(p,p$'$) data from [73] and ^{124}Sn(γ,n) data from references [154], [155], [156], [157]. All fitted structures are marked by solid and dashed lines.

Table 6.6: Parameters for the low-lying component of the γRSF.

Model	$C_{up} \cdot 10^{-8}$ (MeV^3)	$a_u p$ (MeV)
Spin distribution cut up to J=4		
Average+GLO	2.6^{+9}_{-17}	0.1^{+3}_{-3}
G&C+GLO	3.2^{+13}_{-12}	0.6^{+2}_{-2}
Spin distribution cut up to J=5		
Average+GLO	3.66^{+24}_{-14}	1.2^{+7}_{-9}
G&C+GLO	3.6^{+20}_{-22}	0.9^{+3}_{-6}

isotopes [21] and allows a further joint analysis of the previously extracted systematics and the strength for ^{124}Sn in this work. The calculated strengths are presented in Figures 6.10 and 6.11. The γRSF for the spin distribution cut up to the higher spin was found to be in an exceptionally good agreement with the corresponding (p,p$'$) data throughout the whole range of overlapping. All the parameters could be found in the same Tables 6.5-6.7.

The estimated IVGDR parameters for the GLO model are in a good agreement for the G&C and average γRSF. All the deviations in the parameters will be mostly driven by the difference in the low-energy γRSF behavior. However, this difference is negligible within the estimated errors. Similar could be observed for the centroids of both PDRs: these centroids change negligibly as one compares all the models used. This holds true especially for the larger component of the

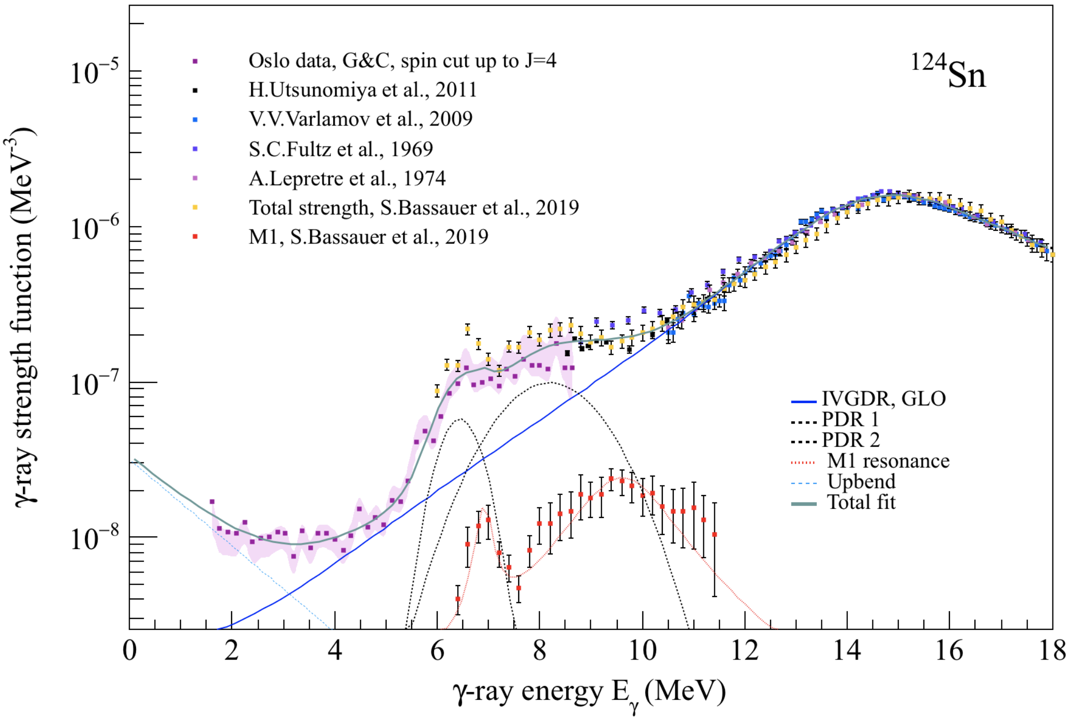

Figure 6.10: The G&C γRSF for ^{124}Sn with the spin distribution cut $J_{max} = 4$, comparison with the ^{124}Sn(p,p′) data from [73] and ^{124}Sn(γ,n) data from references [154], [155], [156], [157]. All fitted structures are marked by solid and dashed lines.

PDR. Despite the fact that the lighter resonance component is shifted slightly towards higher energies, the corresponding centroids coincide for all models, as the error bars are considered. On the other hand, the resonance absolute value normalization constants C and widths σ change more notably as one compares the γRSF with two different spin distribution cuts η_4 and η_5. The general trend for all modes is the increase of amplitudes for the smaller and the larger components, as the spins $J = 5$ are assumed to be populated. This is accompanied by the smaller resonance becoming wider and the larger resonance becoming narrower: the strength is redistributed between both resonances. These changes inevitably affect the total integrated strength for the PDR, estimated as:

$$S_{PDR}\ [\text{mb}\cdot\text{MeV}] = 3\pi^2\hbar^2c^2\ [\text{mb}\cdot\text{MeV}^2] \int_0^\infty dE_\gamma[\text{MeV}]\ E_\gamma[\text{MeV}]C[\text{MeV}^{-2}]\frac{1}{\sqrt{2\pi}\sigma[\text{MeV}]}e^{-\frac{(E_\gamma - E)^2}{2\sigma^2}}. \tag{6.17}$$

These strengths could be compared with the classic electric dipole TRK sum rule:

$$S_{E1} = 60\frac{NZ}{A}\ [\text{mb}\cdot\text{MeV}] = 1790.32\ [\text{mb}\cdot\text{MeV}]. \tag{6.18}$$

All the strengths mentioned are listed in Table 6.7. In addition to the total strengths, the corresponding fractions of the TRK sum rule were estimated. The errors included in all tables up to this moment were calculated for each parameter a as:

$$\Delta a^{upper} = a\sqrt{\Delta a_{fit}^2 + \left(\frac{a_{upper}^{\rho} - a}{a}\right)^2 + \left(\frac{a_{upper}^{\Gamma} - a}{a}\right)^2}, \tag{6.19}$$

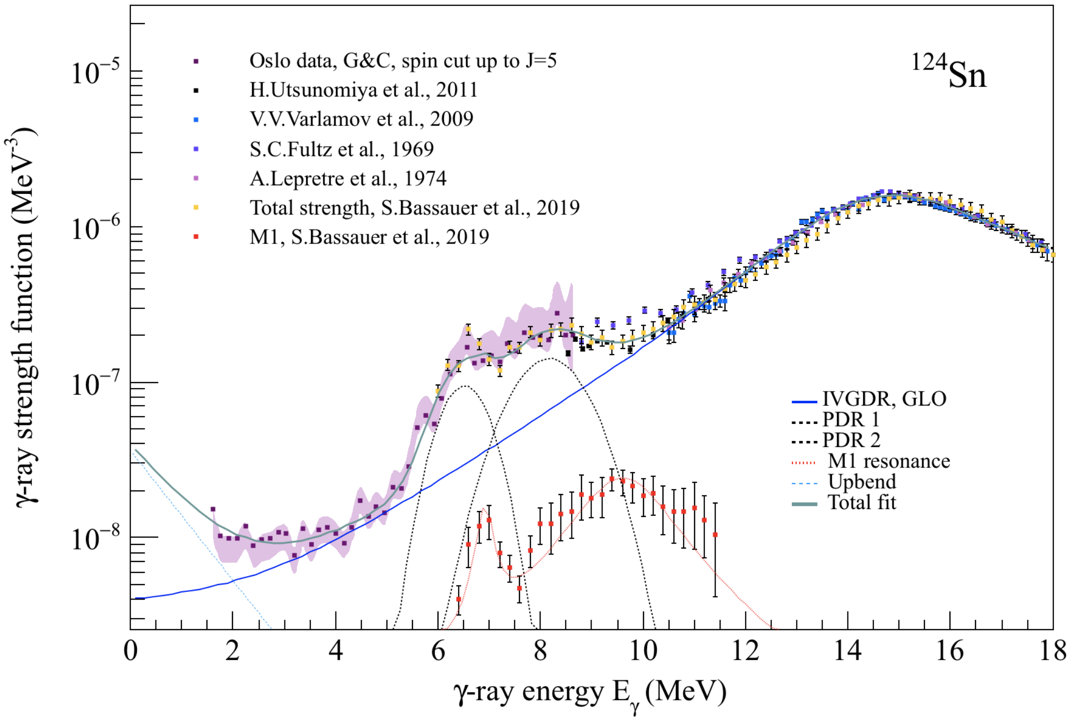

Figure 6.11: The G&C γRSF for ^{124}Sn with the spin distribution cut $J_{max} = 5$, comparison with the ^{124}Sn(p,p$'$) data from [73] and ^{124}Sn(γ,n) data from references [154], [155], [156], [157]. All fitted structures are marked by solid and dashed lines.

Table 6.7: Parameters for two components of the PDR in ^{124}Sn.

Model	$E_{PDR\ 1}$ (MeV)	$\sigma_{PDR\ 1}$ (MeV)	$C_{PDR\ 1} \cdot 10^{-7}$ (MeV^{-2})	$E_{PDR\ 2}$ (MeV)	$\sigma_{PDR\ 2}$ (MeV)	$C_{PDR\ 2} \cdot 10^{-7}$ (MeV^{-2})
			Spin distribution cut up to J=4			
Average+GLO	6.47^{+7}_{-5}	0.45^{+5}_{-7}	0.83^{+18}_{-20}	8.17^{+12}_{-6}	0.87^{+15}_{-13}	2.71^{+37}_{-38}
G&C+GLO	6.44^{+8}_{-3}	0.42^{+8}_{-3}	0.60^{+25}_{-11}	8.19^{+11}_{-9}	1.00^{+8}_{-10}	2.47^{+21}_{-20}
			Spin distribution cut up to J=5			
Average+GLO	6.56^{+5}_{-8}	0.52^{+4}_{-5}	1.43^{+26}_{-36}	8.19^{+5}_{-5}	0.67^{+12}_{-8}	2.67^{+25}_{-27}
G&C+GLO	6.52^{+7}_{-5}	0.49^{+6}_{-3}	1.16^{+24}_{-19}	8.17^{+6}_{-6}	0.73^{+11}_{-11}	2.58^{+32}_{-24}

$$\Delta a^{lower} = a\sqrt{\Delta a_{fit}^2 + \left(\frac{a_{lower}^{\rho} - a}{a}\right)^2 + \left(\frac{a_{lower}^{\Gamma} - a}{a}\right)^2}, \tag{6.20}$$

here Δa_{fit} is the fit-based error, other contributions are stemming from variations of this parameter due to variation of the level density $\rho(S_n)$ (a^{rho}) and Γ_γ (a^{Γ}).

All the variations in the models or the spin distribution cuts were found to affect the fraction of the TRK sum rule. The G&C+GLO for the γRSF with η_4 yields the lowest fraction of $\approx 1.5\%$. This could be expected from the model with the lowest-lying strength. The corresponding

Table 6.8: Total intergated strength and the TRK sum fraction for the pygmy dipole strength in ^{124}Sn.

Model	Total integrated strength (MeV·mb)	TRK fraction (%)
Spin distribution cut up to J=4		
Average+GLO	32^{+2}_{-6}	1.8^{+1}_{-3}
G&C+GLO	28^{+5}_{-1}	1.5^{+3}_{-1}
Spin distribution cut up to J=4		
Average+GLO	36^{+2}_{-4}	2.0^{+1}_{-2}
G&C+GLO	33^{+4}_{-2}	1.8^{+2}_{-1}

fractions increase up to $\approx 1.8\%$ as $J_{max} = 5$ is assumed. Finally, the largest fraction is observed for the averaged γRSFs with η_5 with the GLO parametrization of the IVGDR. It is important to notice that all variations of the γRSF due to the input parameters result in comparatively large errors for the TRK sum rule fractions, so that a realistic value could be well confined within the estimated limits.

Chapter 7

Discussion

The following chapter aims at collecting and revising all principal results obtained in the present work. Particularly, a specific focus will be made on the comparison of the final γ-ray strength functions, corresponding to three alternative normalizations, with the previously extracted γ-ray strength functions for the lighter Sn isotopes as well as the strength, obtained in the Coulomb excitation experiment (p,p$'$) on ^{124}Sn. Similar comparison will be presented for the nuclear level densities. An essential part of the analysis involves the test of the Brink-Axel hypothesis for several chosen excitation energy ranges. Finally, the extracted characteristics of the PDR in ^{124}Sn will be put into more general systematics, and all trends observed will be discussed from the perspective of the PDR evolution with the increasing number of neutrons.

7.1 Analysis of the nuclear level densities and γ-ray strength functions

The results of the Oslo method should be carefully constrained with external experimental values, such as the level density at the neutron separation energy, discrete low-lying levels, average radiative width. In some particular cases, as in the present case of ^{124}Sn, these values should be extracted from systematics. In both cases, the quality of the resulting fits and normalizations is directly related to the values used. Some particular effects of different input parameters as well as a certain trend with the increasing number of neutrons could be traced in a comparison of the level densities and γRSF for different isotopes. In case of the studied ^{124}Sn, the consistent comparison could be provided by the preceding OCL experiments on $^{116-119,121,122}$Sn, mentioned in Section 2.4. Despite that the experiments were performed at the same Oslo Cyclotron Laboratory and the resulting primary matrices were obtained with the same Oslo method, several instrumentational improvements have been performed before 2019. The CACTUS array with 28 collimated NaI:Tl detectors was exploited for the photon detection. The experiments on the lightest ^{117,119}Sn isotopes were also performed with the simplest Si telescope, comprising of 8 $E-\Delta E$ telescopes, grouped in a similar way as the E pads in SiRi. However, no segmentation of the ΔE detectors was implemented, leading to comparatively worse energy resolution of the system. In addition, the approaches to the normalization of the resulting strengths and level densities vary from experiment to experiment.

The first experiments on ^{116,117}Sn were performed with the 38 MeV beam of ^{3}He, and the corresponding γRSF and level densities were extracted from the (^{3}He,$\alpha\gamma$) and (^{3}He,^{3}Heγ) correspondingly [65]. The G&C approach was applied for the estimation of the spin-cutoff parameters, whilst the BSFG model was adopted for the interpolation between the experimental data and $\rho(S_n)$. In contrast to the present work, the level density parameter a and the energy back-shift E_1 were adopted from the older version of systematics from T. von Egidy *et al.* [159]. Moreover, the level spacings for s- and p-wave resonances D_0 and D_1 were extracted from the earlier version of the neutron resonance data compilation [160]. The important detail of this experiments is the additional study of the spin distribution, carried out for both reactions with an additional Ge detector. The spins up to $J \approx 6$ were populated. Similar approach and experimental conditions were reported for the analysis of ^{118,119}Sn in [67]. Finally, the latest experiments were performed with the updated particle telescope SiRi with the same beam parameters and the same approach to the parametrization of the BSFG, interpolating the experimental data and $\rho(S_n)$ [67].

The nuclear level densities for $^{116-119,121,122}$Sn and ^{124}Sn, extracted in the present work, are shown in Figure 7.1. Since the G&C approach was applied in the normalization procedure in [21, 65, 67], the total level density corresponding to the same model approach was chosen for the comparison. The choice of the level density at the neutron separation energy yields the overall behavior of the level density close to that for even-even isotopes ^{116,118,122}Sn. The trends demonstrated by these isotopes are in a particularly good agreement for energies above ≈ 3 MeV. Comparison with the even-odd Sn isotopes demonstrates a clear odd-even effect: the level densities of even-odd Sn isotopes are shifted up as compared to the even-even isotopes, as it is expected. The improved energy resolution for both the particle and photon detecting system results in observation of two distinct peaks at $E_x = 0$ MeV and $E = 1.131$ MeV, denoting the ground and the first excited states in ^{124}Sn. Somewhat similar could be also observed for ^{122}Sn, but not the lighter isotopes, where the level densities were extracted with the strongly smeared peaks at relatively low energies. As it was reported in [65] and [21, 67], step-like structures superimposed on the general level density trends were observed for all isotopes in the energy range from ≈ 2 MeV up to the neutron separation energies.

The clearest step-like behavior was reported for ^{119}Sn. The level density, extracted in the present work, was also found to demonstrate several steps above $\approx$2 MeV. It is interesting to notice, that the bump at ≈ 2.6 MeV is quite close to the bump at $\approx 2.2-2.6$ MeV, observed for ^{117,119}Sn and all even-even Sn isotopes. This corresponds directly to the doubled neutron gap

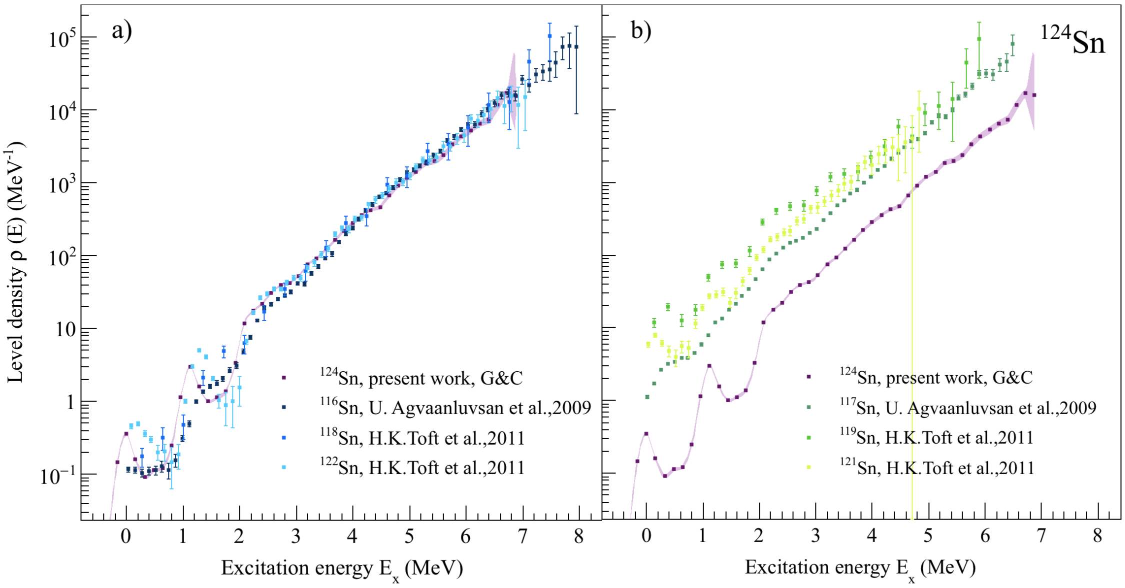

Figure 7.1: a) The level density for ^{124}Sn extracted with the G&C approach; comparison with the even-even Sn isotopes ^{116,118,122}Sn, reported in [21, 65, 67]. **b)** The extracted level density for ^{124}Sn, G&C approach; comparison with the even-odd Sn isotopes ^{117,119,121}Sn, reported in [21, 65, 67].

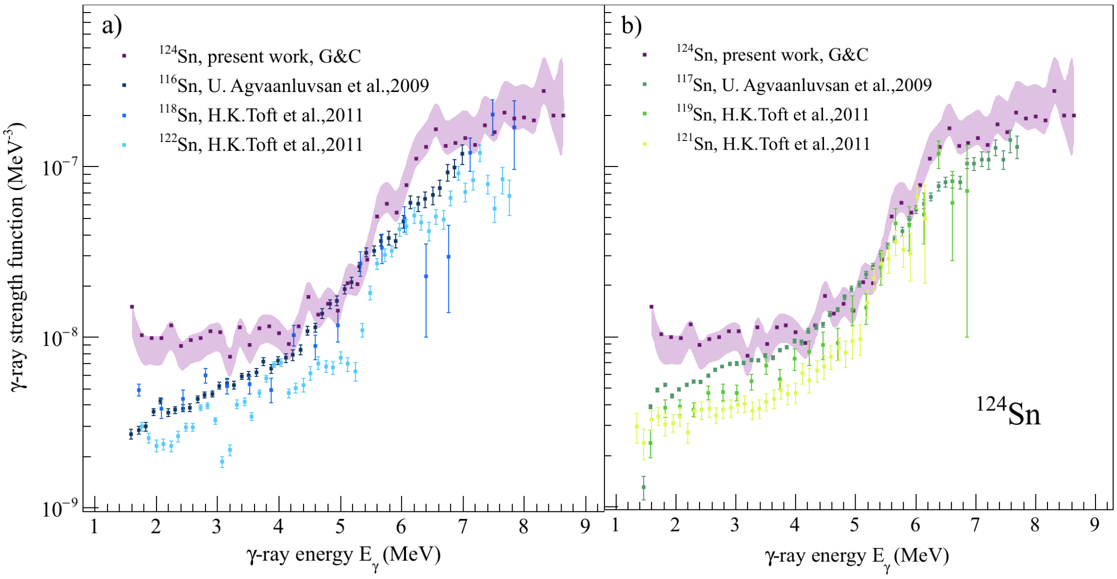

Figure 7.2: **a)** The extracted γRSF for ^{124}Sn, the G&C approach and the spin distribution cut up to $J = 5$ were used; comparison with the even-even Sn isotopes ^{116,118,122}Sn, reported in [21, 65, 67]. **b)** The extracted γRSF for ^{124}Sn, G&C approach and the spin distribution cut up to $J = 5$; comparison with the even-odd Sn isotopes ^{117,119,121}Sn, reported in [21, 65, 67].

energy $2\Delta_n \approx 2.6$ MeV for ^{124}Sn. Similar structures were earlier explained by the consecutive breaking of neutron Cooper pairs [161]. Every broken pair is followed by a slight increase of the level density, as it could be seen from Figure 7.1. The bump at ≈ 5 MeV could be then attributed to the second neutron pair breaking.

Similar comparison could be performed for the γRSF for the studied isotope ^{124}Sn and $^{116-119,121,122}$Sn (see Figure 7.2). Several new features could be distinguished in ^{124}Sn as compared to the lighter isotopes: the presence of a certain enhancement at ≈ 6 MeV and the flattening of the strength below ≈ 4 MeV. The γRSFs for the lighter isotopes do not demonstrate any prominent features; the ^{118}Sn data are suffering from scarce statistics so that it becomes impossible to judge on presence of any structures. This might be explained by the comparatively low energy resolution of both detecting systems - the CACTUS scintallator array (before 2018) and the Si particle telescope without segmentation into separate strips (before 2011). The improved resolution enables observation of separate structures of the strength, such as and additional enhancement at ≈ 6.5 MeV. A similar feature was observed in the data from the (p,p$'$) Coulomb excitation experiment at the RCNP [73] for all even-even isotopes ^{112,114,116,118,120,124}Sn. The low-lying tail of the γRSF for ^{124}Sn differs significantly from those in the lighter isotopes. The largest difference is observed for the neighboring isotopes ^{121,122}Sn and ^{124}Sn. In contrast to the trends, set by these isotopes, the γRSF for ^{124}Sn does not approach zero value for $E_\gamma \to 0$ MeV and could be rather observed reaching a flat plateau. Similar low-energy behavior, or upbend, has been observed in other OCL experiments as well. R. Schwengner *et al.* [162] performed the microscopic calculations, pointing at the $M1$ nature of this feature. Strong $M1$ transitions (and correspondingly large transition matrix elements) were predicted for ^{90}Zr and $^{94-96}$Mo for the transitions between the initial and final configurations with spins J_i and $J_f = J_i \pm 1$, formed by recoupling of spins of protons and neutrons from the decoupled pairs at high-j orbitals. Alternatively, the finite-temperature RPA calculations point at the electric dipole nature of the underlying transitions [163], while the angular distribution study for ^{56}Fe points at the mixture of $M1$ and $E1$ transitions, forming the low-energy tail of the strength [164]. An additional study of the angular distribution of emitted photons might be required to reveal whether the underlying transitions of $M1$ or $E1$ nature in ^{124}Sn.

7.2 Study of the γRSF as a function of excitation energy

The Brink-Axel hypothesis, discussed in Section 3.3, is one of the core assumptions in the present analysis. The reliability of this hypothesis reflects directly the reliability of the obtained results, and the study of the γRSF as a function of initial excitation energies, involved in the observed transitions, and final excitation energies, fed by these transitions, was performed. The procedure, described in Section 5.5 was applied. For the first case, series of γRSF $f(E_i, E_\gamma)$ were extracted for each excitation energy bin E_i with the known level density, corresponding to the spin distribution cut up to $J_{max} = 5$; these functions are built on the specific initial excitation energies included in a considered bin with no gating put on the final state. The binning was chosen to be $\Delta E_x = 160$ keV.

The strength functions extracted for each third bin in the energy range between 5.0-8.5 MeV are shown in Figure 7.3. In addition, the γRSF averaged over this range is compared to each

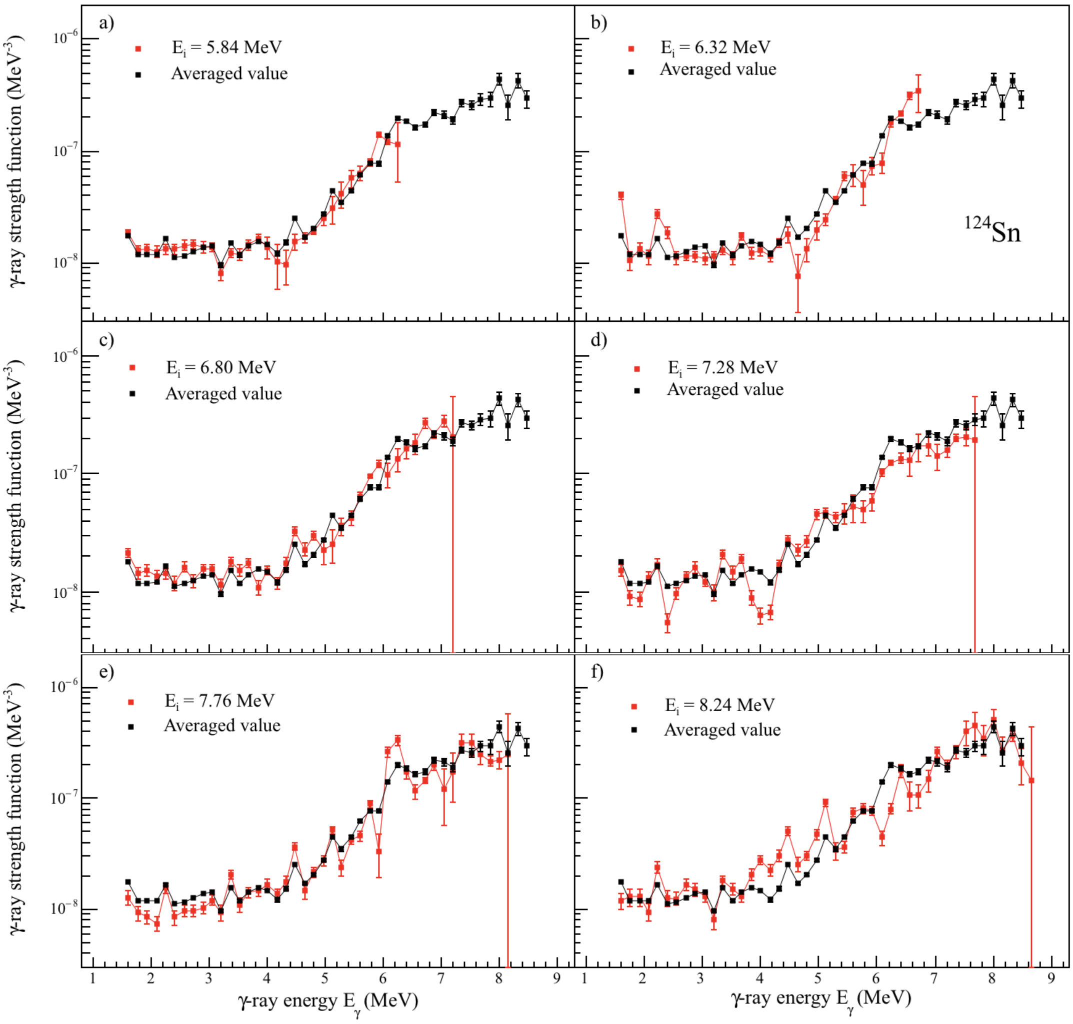

Figure 7.3: γRSF for several initial excitation energies for ^{124}Sn, the results are compared with the average γRSF. Binning with the width of 160 keV is applied to the initial excitation energies.

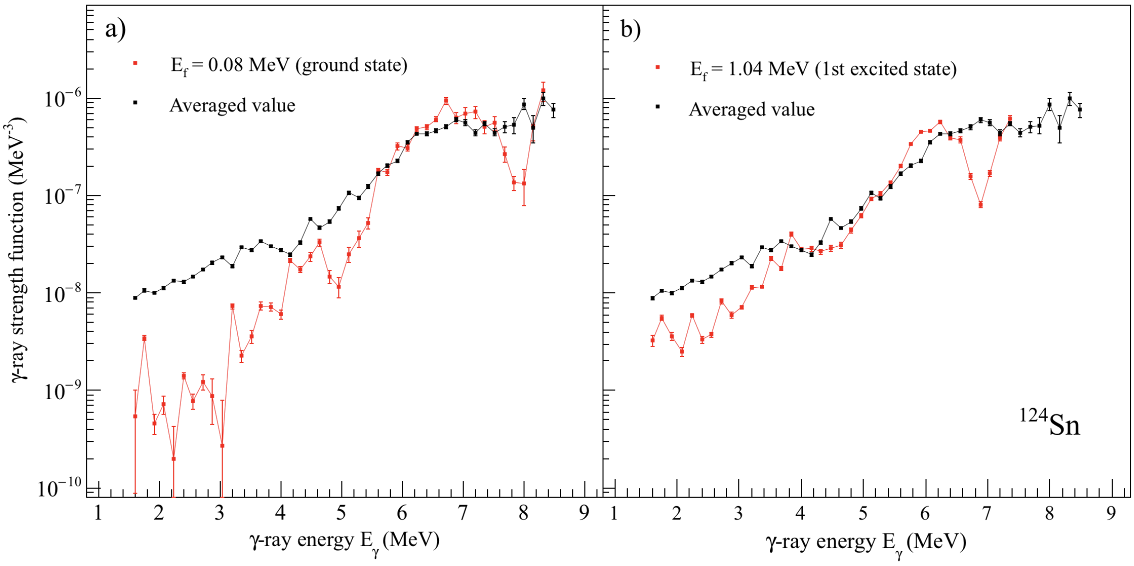

Figure 7.4: **a)** γRSF feeding the ground state in ^{124}Sn, energy marked corresponds to the center of the energy bin, including the ground state. **b)** γRSF feeding the first excited 2^+ state in ^{124}Sn, energy bin, including this state is plotted.

strength for the chosen initial energies. The width of the excitation energy gate coincides with that used in the standard Oslo method analysis (see Chapter 5), and this averaged strength would correspond to the average γRSF for the spin distribution cut up to $J_{max} = 5$ if corrected for the difference in the normalization due to the different normalization procedure. An overall agreement between all extracted strengths could be observed: for each initial excitation energy the strength is built on, it appears to be fluctuating with respect to the average strength. This behavior might be explained by the Porter-Thomas fluctuations due to the specific complexity of the chosen initial states. Nevertheless, the fluctuations do not exceed the statistical errors in the majority of cases. The assumption of the γRSF being independent of the initial excitation energies could be a fairly good assumption for the final extracted γRSFs, reported in the previous chapter. This result is somewhat similar to the conclusion drawn in the study of the lighter ^{64,65}Ni nuclei [117]. In all discussed cases, the Porter-Thomas fluctuations play a significant role due to the relatively low densities of accessible states (*e. g.* as compared to the case of ^{238}Np [115]). The averaging is performed over a relatively smaller amount of transitions for ^{64,65}Ni and ^{124}Sn, and variations in the individual transition widths are more apparent than for the case of ^{238}Np.

The fluctuations were predicted to increase with E_γ [117], and this might also explain some exceptionally strong fluctuations for the high energy parts of the strengths in Figure 7.3. On the other hand, the fluctuations of the γRSF in the present work become stronger as one approaches the neutron separation energy. The case of ^{64,65}Ni demonstrated the opposite tendency, *i.e.* a decrease of the role fluctuations play for the highest initial excitation energies. It does not explain relatively large fluctuations for the highest excitation energy bins (see Figure 7.3 e) and f)). The reason for it might be related to the remaining weak aluminum contaminants in the vicinity of the neutron separation energy in the first generation matrix. They generate especially strong additional structures in the spectra, used for extraction of γRSFs, denoted by e) and f) in Figure 7.3. This gives an additional complication for the check of the Brink-Axel hypothesis for the excitation energy bins close to S_n.

By analogy with the study of the γRSFs for different initial excitation energies, the γRSFs, feeding different final states, could be investigated. The first generation matrix, discussed in Chapter 5, contains well-distinguishable transitions to the ground state and the first excited state (2^+ state at $\approx$ 1.1 MeV), strongly populated in the deexcitation from above-lying excited states, which makes them a good subject of the study. The procedure, described in Section 5.5, was exploited to extract series of the γRSF, feeding different final states, as well as the reference strength, averaged over the same width of the excitation energy range, as the average γRSF, stemming from the different initial states. The γRSF feeding the ground state and the first excited state are shown in Figure 7.4. For the ground state γRSF the fluctuations observed are significantly stronger, than for the previously discussed cases. Moreover, the strong deviation from the reference γRSF below $E_\gamma \approx 5.5$ MeV could be observed. Since the final state is fixed, for each E_γ the initial state could be unambiguously defined as $E_i = E_f + E_\gamma$. The least deviations are observed for $E_\gamma >$5 MeV, covering the same range of excitation energies as the one chosen for the standard Oslo method analysis (Chapter 5), confirming the reasonable choice of the excitation energy range for the previously discussed strengths. Strong discrepancy between the ground state and the average strengths might arise from several reasons. Firstly, it might be driven by the strong Porter-Thomas fluctuations. Indeed, relatively few transitions populating the ground state are involved in the averaging procedure yielding the reference γRSF (black line in Figure 7.4). This does not accord with the statistical picture, assumed by the standard Oslo method procedure. Another factor contributing to the deviation is the large amount of electric quadrupole γ-transitions below $E_x \approx 3$ MeV. The encoded γRSF extraction procedure assumes all transitions to be of the dipole nature, implying that the $E2$ transitions will be found shifted by the factor of $E_\gamma^{2\cdot 2+1}/E_\gamma^{2\cdot 1+1} = E_\gamma^2$. The additional strong deep in the ground state γRSF at $\approx$ 8 MeV correlates with the deep in the ground state diagonal in Figure 5.4 b). The suppressed amount of 1^+ and 1^- states populated in this energy range and the absence of the corresponding transitions reflects directly the drop of the γRSF. Similar deep at $E_\gamma \approx 7$ MeV could be observed for the γRSF for the transitions landing on the first excited state (see Figure 7.4 b). In contrast to the ground state γRSF, the overall agreement with the average strength function is better due to the partial reduction of fluctuations below 5 MeV. As compared to the study of the γRSF as a function of initial energy, the two γRSFs, corresponding to two specified final excited states, demonstrate larger local deviations from the average strength. Since these deviations could be explained by numerous reasons, the check of the Brink-Axel hypothesis validity is obscured. For the higher-lying energy bins above the first excited state the overall agreement with the average strength becomes more clear as compared to the ground state and the first excited state γRSFs. The low-energy tails would still contain a considerable fraction of $E2$ transitions, which question reliability of the low-energy trends set by the γRSF. However, this problem was avoided in the final results on the γRSFs from the standard Oslo method by limiting the low part of range for E_γ by 1.6 MeV (see discussion of the chosen region in Section 5.2).

In addition, the downward γRSF, extracted in the present work, was used to estimate the $B\downarrow(E1)$ strength distribution and compare it with the upward strength $B\uparrow(E1)$, obtained in the RCNP (p,p$'$) experiment. In order to perform the comparison on the same footing, it was taken into account that the normalization used for the extraction of the ground state γRSF requires an adjustment. The ground state strength was, therefore, scaled to correspond to the RCNP strength at the 6.4 MeV peak (lower-lying pygmy component). In principle, such scaling includes an additional relation between the strengths, which should be also taken into account for the transitions between $E_i < E_f$ with spins $J_i = 0$ and $J_f = 1$ (see Equation 2.1):

$$\frac{B\uparrow}{B\downarrow} = \frac{B(i \to f)}{B(f \to i)} = \frac{2J_f + 1}{2J_i + 1} = 3. \tag{7.1}$$

The comparison of the strengths is shown in Figure 7.5. Both distributions are in a very good

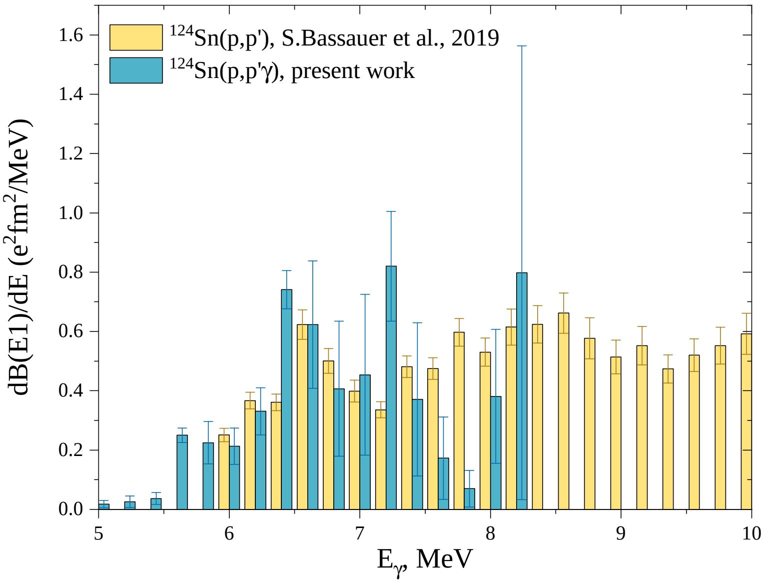

Figure 7.5: $B(E1)$ strength distribution for ^{124}Sn, extracted in the present work and the RCNP (p,p′) experiment [73].

agreement for energies up to $E_\gamma = 7$ MeV, *i.e.* all the features observed in the RCNP strength are well reproduced in the present experiment. However, strong deviations are observed for the energies above 7 MeV up to the neutron separation energy. The present strength demonstrates two strong peaks at ≈ 7.2 MeV and 8.2 MeV with the dropping strength in between. I general, these features correlate with the distribution of counts in the high-energy tail of the ground state diagonal in the primary matrix, but the origin of these two strong peaks and significant deviation from the RCNP strength distribution requires an additional and more thorough study. In contrast to the ground state strength, corresponding to the transitions from the states with spin and parity $J = 1^{\pm}$ and the ground state $J_{g.s.} = 0^{+}$, the average strength, discussed in the previous chapter involves the dipole transitions from the states, populated in the reaction, which would, on average, have the non-zero spins larger than $J = 1$. Let us assume that the average spin populated is $J_f = 4$. The allowed dipole transitions to $J_i = 3, 4, 5$ could lead to the crude simplification of $J_f = 4 \rightarrow J_i = 4$, implying that the upward and the downward strengths satisfy an approximate equality $B\uparrow \approx B\downarrow$. Thus, the corresponding γRSFs yield $f\uparrow \approx f\downarrow$. To a certain extent, this simplification makes the joint analysis of the strengths, discussed in Chapter 6 possible.

7.3 Evolution of the PDR in $^{116-119,121,122,124}$Sn isotopes.

The γRSFs, extracted and discussed in the previous chapter, were combined with the strengths from the (γ,n) and (p,p′) experiments in order to complete the response of a nucleus to an external excitation (by photons and protons). The more complete response allows us to estimate several bulk parameters, characterizing the PDR in ^{124}Sn, such as the energy centroid, integrated strength and the fraction it exhausts in the TRK sum. All relevant parameters were provided in Chapter 6, and Figures 6.8-6.11 show four alternative approaches, stemming from the different approaches to the normalization procedure. The reliability of the normalization could be verified by the comparison with other experimental strengths. In case of ^{124}Sn the maximum overlap in E_γ was provided by the Coulomb excitation (p,p′) experiment from [73]. As it could be inferred

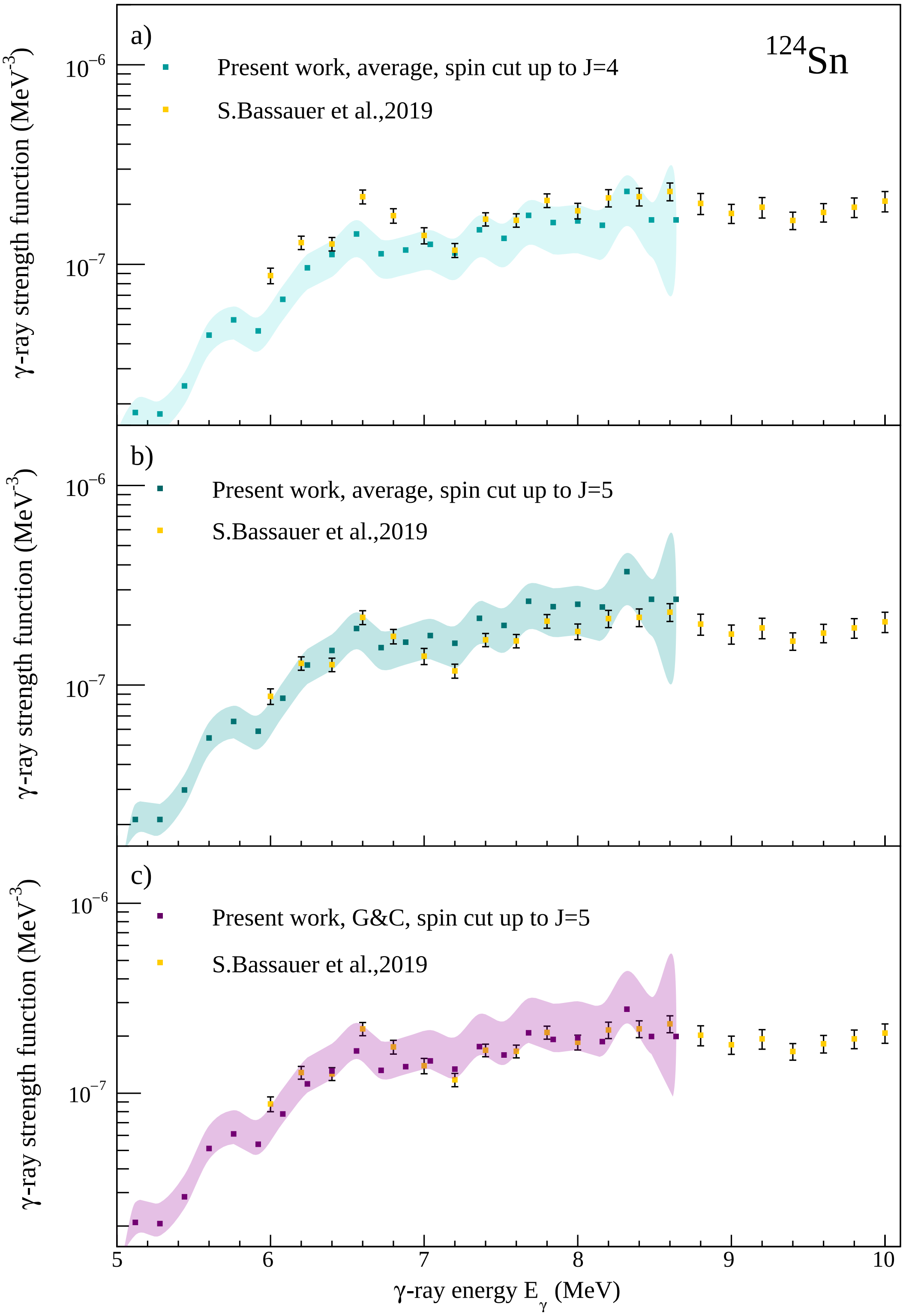

Figure 7.6: Comparison of the RCNP (p,p′) experiment with the extracted γRSF: **a)** average strength for $J_{max} = 4$, **b)** average strength for $J_{max} = 5$, **c)** G&C strength for $J_{max} = 5$.

from Figure 6.10, the G&C γRSF with the spin cut up to $J = 4$ demonstrates unrealistically low absolute value and deviates dramatically from the another (p,p′) and (γ,n) experiments. This strength could be safely excluded from the consideration. On the other hand, two average

γRSF for $J_{max} = 4, 5$ and the G&C γRSF for $J_{max} = 5$ demonstrate fairly good agreement with the RCNP (p,p$'$) experiment (see Figure 7.6). Close examination of the primary matrix reveals several low-E_γ transitions, stemming from the populated excited states with the spin $J = 5$. This fact argues for the validity of the γRSF, obtained for the spin distribution cut up to $J = 5$. The corresponding average γRSF could be proposed as the recommended value for the present thesis (Figure 7.6 b)). On the other hand, the *G&C* strength would be proposed for the consistent comparison with the extracted PDR parameters in the lighter PDR isotopes. Another question to be raised is the actual form of the spin distribution, exploited in the present work. The fact that the γRSF for $J_{max} = 4$ is also in a fairly good agreement with the RCNP γRSF might also imply that other forms of the spin distribution might be tested in an additional study. Even though the average γRSF for $J_{max} = 5$ is proposed as the recommended value for a present stage of the analysis, the γRSF for $J_{max} = 4$ should not be completely disregarded; all PDR characteristics will be provided for this solution as well.

The estimated fraction of the TRK sum,exhausted by the PDR in ^{124}Sn is shown in Figure 7.7. It is interesting to notice, that the value, extracted for the G&C γRSF, *i.e.* with the similar approach as the one applied for the lighter Sn isotopes, indeed confirms the conclusion in Ref. [21]: both the integrated strength and the TRK sum fraction do not change significantly with the increasing neutron number N. Both the value for the average strength for $J_{max} = 4$ and G&C strength for $J_{max} = 5$ for ^{124}Sn isotope proceed the trend, set by the lighter isotopes.

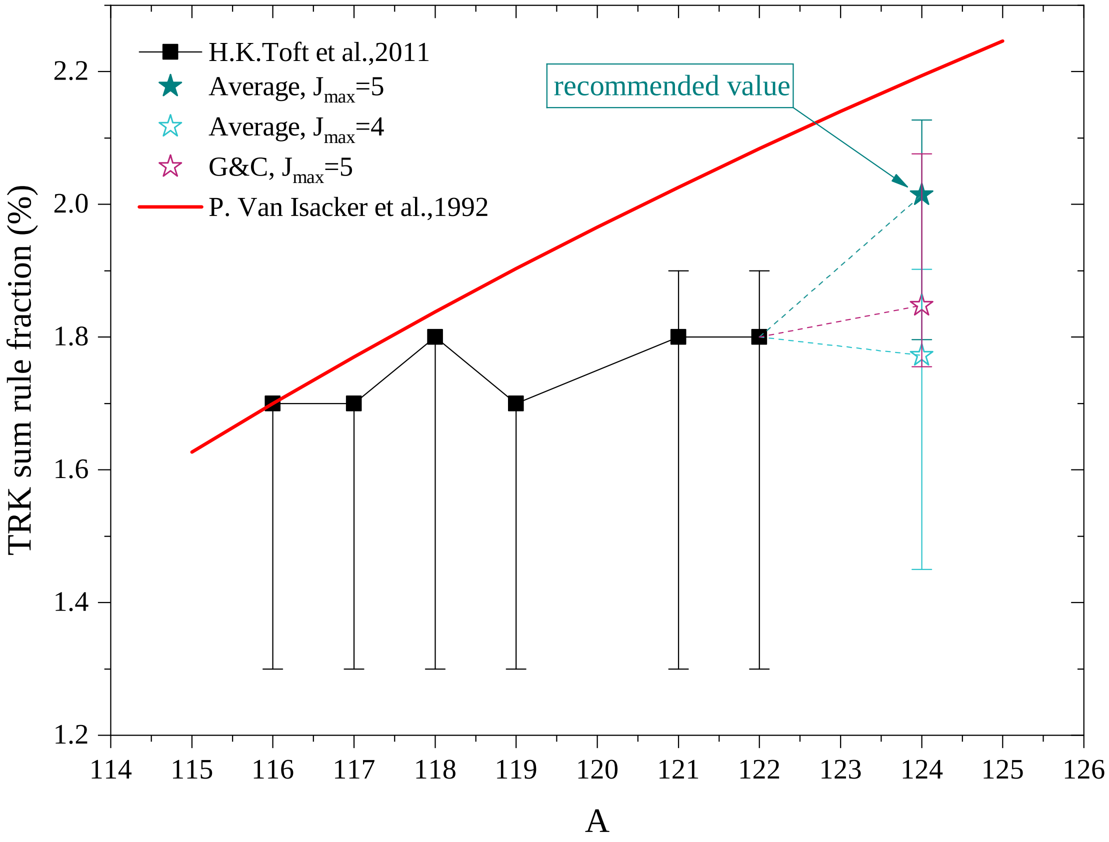

Figure 7.7: The estimated TRK fraction, exhausted by the PDR in $^{116-119,121,122}$Sn isotopes [21], plotted together with the values, estimated on the base of the average γRSF for $J_{max} = 4, 5$ and G&C γRSF for $J_{max} = 5$. Comparison with the theoretical prediction [68] (red line, normalized to the ^{116}Sn isotope).

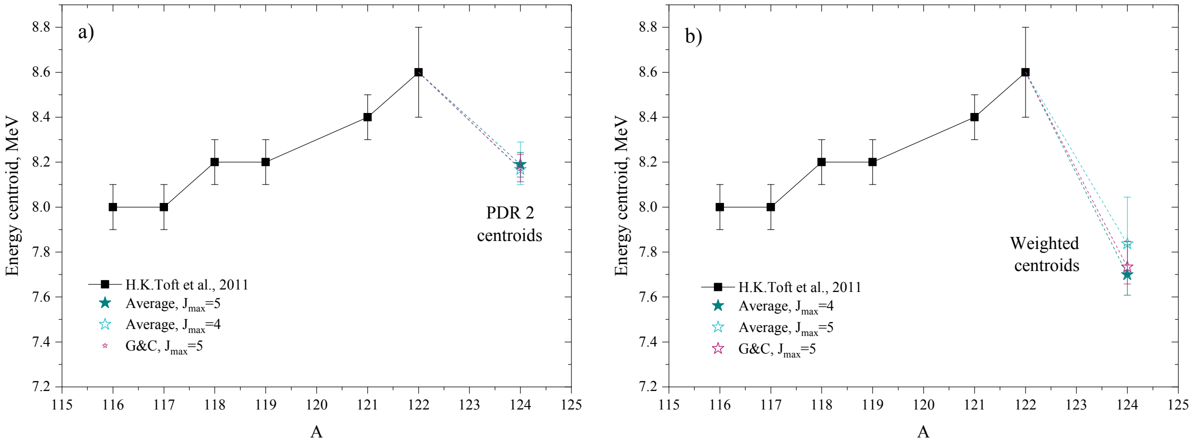

Figure 7.8: **a)** Energy centroids for the PDR in $^{116-119,121,122}$Sn, for the ^{124}Sn the centroid of the higher-lying PDR component is used.**b)** Energy energy centroids for the PDR in $^{116-119,121,122}$Sn, the weighted centroid for two PDR components is used for the ^{124}Sn.

This is in a contradiction with the macroscopic predictions of P. Van Isacker [68] (marked with the red line in Figure 7.7) and microscopic predictions, mentioned in Section 2.4. However, this might be well in accordance with the constant trend, predicted by I. Daoutidis for the mass range $A = 120 - 126$ (see [21] and references therein). In contrary, the value obtained with the γRSF, recommended in this work, could be found at $\approx 2\%$ ot the TRK sum rule, which is by $\approx 0.2\%$ larger, than for the lighter Sn isotopes. Thus, the recommended value sets some trend towards the increasing TRK sum fraction, exhausted by the PDR. The systematic errors, however, are too large and the separate variations in the strength from isotope to isotope are to small to draw any solid conclusions on the increase of the strength of the PDR with the neutron number N. It is also important to mention, that the correct identification of the spin-flip $M1$ resonance, included in the total fit of the strength, might affect the PDR strength. The present work exploits the most resent data on this excitation mode from the RCNP experiment, in contrast to the previous studies, involving the $M1$ parameters, based on the systematics for the neighboring nuclei. In some cases, these systematics might underestimate the strength, attributed to the spin-flip mode, thus, overestimating the strength, attributed to the PDR. This might lead to a more clear trend in the evolution of the integrated strength for the PDR and the TRK sum rule fraction exhausted.

As compared to the ^{116,124}Sn(γ, γ') experiment, reported in [43], the TRK sum fraction for the PDR was estimated to be $\approx 0.4 - 0.6\%$ [21], which is considerably lower, that the proposed estimate for the ^{124}Sn isotope. This discrepancy might be due to the presence of unresolved strength in the (γ, γ') experiment, which was excluded from the calculation. This strength might contribute to the significant increase of the estimated fraction, making it comparable with the corresponding value for ^{124}Sn. Another estimate for the TRK sum fraction for ^{124}Sn was proposed on the base of the strength,extracted in the $(\alpha, \alpha'\gamma)$ experiment [72]. The percentage isoscalar EWSR was estimated to be $\approx 1.5(2)\%$, which is comparable with the recommended value in the present work. However, the latter did not involve separation into the isoscalar and isovector components of the total observed strength, and it would be more reasonable to compare it with $\approx 2.2(3)\%$, extracted from the total measured strength in the discrete peaks. This value does not include the unresolved strength, but is in a very good agreement within the errors with the recommended value in the present work.

Another bulk property to be examined is the energy centroid of the observed PDR. Since the γRSFs were fitted with the two Gaussian functions, this could be either associated with the centroid if the largest higher-lying component (see Figure 7.8 a)) or the centroid, weighted as:

$$E_C = \frac{E_{PDR\ 1}S_{PDR\ 1} + E_{PDR\ 2}S_{PDR\ 2}}{S_{PDR\ 1} + S_{PDR\ 2}}, \tag{7.2}$$

where S denotes the integrated strength for each component. This value is shown in Figure 7.8 b) together with the energy centroids of the lighter isotopes. In both cases, the considerable shift towards low energies is observed for ^{124}Sn. This deviates strongly from the trend towards higher energies, set by the lighter Sn isotopes in the previous works, contradicting to, *e.g* the RHB + RQRPA predictions in [10]. In this case again the revision of the $M1$ resonances might also affect the positions of the PDR significantly. Nevertheless, the absolute value of the centroid for the largest PDR component is in a relatively good agreement with the ≈ 8.4 MeV, predicted in [10].

As it was shown in this work, the final parameters, describing the PDR are quite sensitive to the detals of the noralization procedure of the γRSF. The preliminary reevaluation of the integrated strengths and centroids for the PDR with the RCNP data chosen for the description of the IVGDR and $M1$ component of the dipole nuclear response for several lighter Sn isotopes indicated that the centroids of the resonances would change insignificantly, whereas the integrated strengths might drop or increase significantly for some cases (*e.g.* in ^{116}Sn). It implies that the deviations from the almost constant TRK sum rule fraction might be expected. However, for the present stage of the analysis, the G&C γRSF confirms the constant trend of the TRK sum fraction, observed for the lighter Sn isotopes, and points to the deviation from the further shift of the pygmy dipole strength towards higher γ-energies.

Chapter 8

Summary and outlook

8.1 Summary

This thesis was majorly motivated by numerous theoretical predictions and questions on how the PDR evolves with neutron number for nuclei approaching the edge of the valley of stability and the need for a systematic experimental approach to these questions. The work is devoted to the experimental study of the PDR in ^{124}Sn using the (p,p$'\gamma$) reaction. The γ-ray strength function and the level density were extracted from the p-γ coincidence data by means of the Oslo method, and constrained with parameters estimated from systematics on neutron-resonance experiments for the neighboring Sn isotopes. The uncertainties of these parameters were used to estimate the systematic uncertainties of the γRSF and level density. They were subsequently combined with the errors propagated in the Oslo method to estimate the total uncertainties for both extracted quantities.

The level density in ^{124}Sn revealed several clear peaks corresponding to the low-lying discrete levels and several step-like structures in the quasi-continuum region which might be attributed to breaking of neutron pairs. In overall, the level density demonstrates an exponential increase with excitation energy and could be well described by the constant temperature approach. Three different normalizations were tested for the γRSF. The average strength, lying within the limits set by the rigid body approach and the approach proposed by Gilbert and Cameron [82], was chosen to represent one of the normalization cases. The range of the spins populated in the reaction was found to be limited. Therefore, two probable maximum spins $J_{max} = 4$ and $J_{max} = 5$ were assumed, and the γRSFs were corrected for the spin distribution cut up to these spins. This correction yielded two slightly deviating strength functions considered in this work. The third γRSF was obtained with the approach of Gilbert and Cameron for $J_{max} = 5$. All three γRSFs were found to flatten strongly in the low γ-energy range below ≈ 4 MeV. At ≈ 6.5 MeV, a peak-like structure was observed. Within the estimated uncertainties, all three strengths, especially the strength based on the Gilbert and Cameron approach, are in good agreement with the external (p,p$'$) and (γ,n) experimental data.

The integrated strength, the TRK sum fraction, and energy centroid were estimated by fitting the extracted strengths together with the external data covering the range of the IVGDR. The strength with the spin distribution cut up to $J_{max} = 5$ was found to yield the strongest PDR among the Sn nuclei studied at the Oslo Cyclotron Laboratory (2% of the TRK sum rule), indicating an increase of the integrated strength with neutron number. However, the strength obtained with the Gilbert and Cameron approach does not demonstrate an enhanced PDR as compared to the lighter Sn isotopes: the TRK sum fraction exhausted by the PDR remains almost unchanged as one moves from the lightest studied ^{116}Sn to the heaviest ^{124}Sn. Such a behavior deviates from the one predicted by several macroscopic and microscopic approaches.

In all studied cases for ^{124}Sn, the PDR was found to be shifted towards lower γ-energies as compared to other Sn isotopes, which is opposite to an overall shift of the PDR towards higher γ-energies with the increasing neutron number as shown for $^{116-119,121,122}$Sn.

An additional study was carried out to test the applicability of the generalized Brink-Axel hypothesis for the case of ^{124}Sn. The γ-ray strength was shown to fluctuate with respect to the average value as different initial excitation states were considered, confirming an approximate independence of the strength from the initial excitation energy. The γ-ray strength feeding the ground state and the first excited state demonstrate more significant deviations from the average strength. Since there are several physical reasons for these deviations to occur, the Brink-Axel is not expected to hold in these cases. However, the ground state strength function corrected for initial and final spins populated is in a very good agreement with the upward strength distribution from the RCNP experiment [73] in the energy range from $E_\gamma \approx 6$ to 7 MeV.

8.2 Outlook

One of the major concerns remaining in the present work is the uncertainty in the estimate of the spins populated in the reaction for a given spin distribution. Both the choice of the spin range and the form of the corresponding spin distribution adopted for the analysis in the present work might be questioned. These factors might strongly affect the normalization of the obtained γRSF. Some of these effects were demonstrated in the present work. The solution of this problem could involve an alternative technique for a model-independent extraction of the γRSF from the primary matrix. Such a technique was proposed by M. Wiedeking *et al.* in 2012 [165]. It allows to relate the intensities of observed dipole transitions and cross-sections for different excited states to be populated with the γRSF. This method does not involve any assumptions on the spin distribution, does not require the preceding extraction of the level density, and results in a direct extraction of the slope for the γRSF.

An additional study to be performed involves reevaluation of the normalizations for the γRSF in the lighter Sn isotopes as well as the fit parameters of the PDR. As discussed in Chapter 6, a correctly constrained fit for the PDR requires knowledge on both the strength in the IVGDR energy range and the distribution of the $M1$ strength in the energy region of the PDR. The present work exploits the $E1$ and $M1$ strengths obtained recently in the (p,p$'$) RCNP experiment, whereas the analyses on the lighter Sn isotopes included the $M1$ strength constrained by systematics. In cases of some nuclei this $M1$ strength might be under- or overestimated, and the resulting integrated PDR strength would be over- or underestimated. A preliminary analysis for ^{116}Sn demonstrated that the resulting TRK sum fraction might increase by several tenths of percent if the RCNP data are used in the fit.

Finally, the γRSF and nuclear level density presented in this work might be subsequently used for estimating the radiative neutron capture cross-section in the ^{123}Sn(n,γ)^{124}Sn reaction with the nuclear reaction simulation code TALYS. An impact of the PDR on this cross-section could be studied directly in comparison with theoretical predictions disregarding the PDR as an additional component of the electric dipole response of ^{124}Sn. The cross-section constrained with the experimental nuclear input could be subsequently implemented in s-process reaction network calculations for estimating abundances of elements produced in this process. Despite that the impact of the PDR on the neutron capture cross-section for the branching point nucleus ^{123}Sn might be relatively small, it could still affect the abundances of elements produced in the s-process in this mass region.

Appendix A

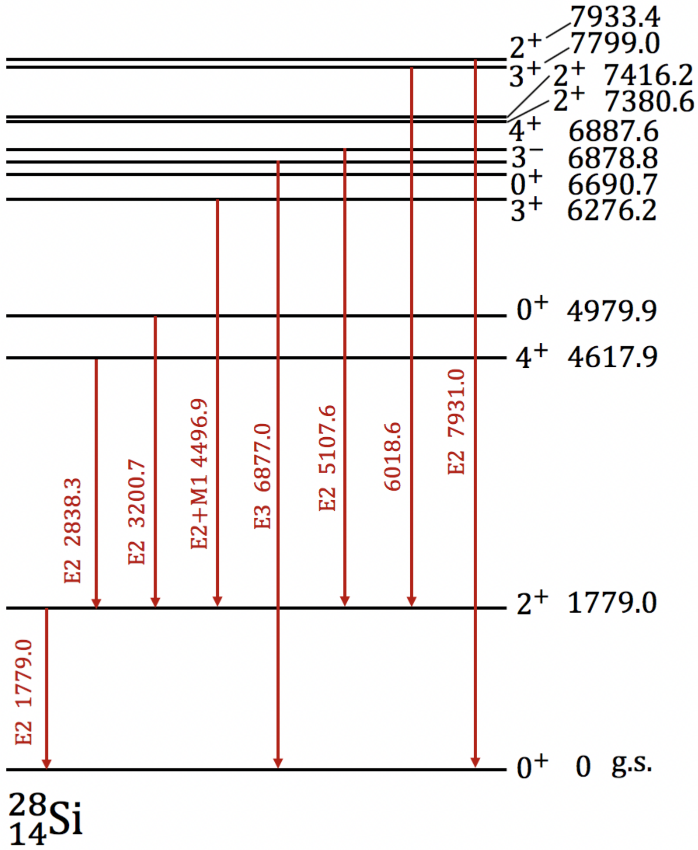

Figure A.1: The level scheme of ^{28}Si including all γ-transitions used for LaBr$_3$:Ce calibration, [90].

Bibliography

[1] M. N. Harakeh, A. van der Woude, *Giant Resonances: Fundamental High-Frequency Modes of Nuclear Excitation*, Clarendon Press, Oxford (2001). SBN-13: 978-0198517337.

[2] J. Piekarewicz, B. K. Agrawal, G. Colò W. Nazarewicz, N. Paar, P.-G. Reinhard, X. Roca-Maza, and D. Vretenar, *Phys. Rev. C* **85** (2012) 041302(R). DOI: https://doi.org/10.1103/PhysRevC.85.041302.

[3] W. Bothe, W. Gentner, *Z. Phys.* **71** (1937) 236 . DOI: https://doi.org/10.1007/BF01340320.

[4] N. Bohr, *Nature* **141** (1938) 326. DOI: https:// 10.1038/1411096b0

[5] A. B. Migdal, *J. Phys.*(USSR) **8** (1944) 331.

[6] M. Goldhaber, E. Teller, *Phys. Rev.*, **74** (1948) 1046. DOI: https://10.1103/Phys Rev.74.1046.

[7] G. C. Baldwin, G.S. Klaiber, *Phys. Rev.* **71** (1947) 3. DOI: https://10.1103/Phys Rev.71.3

[8] G. C. Baldwin and G. S. Klaiber, *Phys. Rev.* **73** (1948) 1156. DOI: 10.1103 /PhysRev.73.1156.

[9] D. H. Wilkinson, *Physica* **22** (1956) 1039. DOI: 10.1016S0031-8914(56)90061-1.

[10] N. Paar, D. Vretenar, E. Khan, G. Colò, *Rep. Progr. Phys.* **70** (2007) 691. DOI: 10.1088/0034-4885/70/5/R02.

[11] B. S. Ishkhanov, N. P. Yudin, *Physics of Elementary Particles and Atomic Nuclei* **31** (2000) 2. http://www1.jinr.ru/Archive/Pepan/v-31-2/v-31-2-2.pdf.

[12] R. Pitthan, Th. Walcher, *Phys. Lett. B* **36** (1971) 563. DOI: 10.1016/0370-2693(71)90090-6.

[13] M.N. Harakeh, K. van der Borg, T. Ishimatsu, H.P. Morsch, A. van der Woude, F.E. Bertrand, *Phys. Rev. Lett.* **38** (1977) 676. DOI: .1103/PhysRevLett.38.676.

[14] A. Klimkiewicz, N. Paar, P. Adrich, M. Fallot, K. Boretzky, T. Aumann, D. Cortina-Gil, U. Datta Pramanik, Th. W. Elze, H. Emling, H. Geissel, M. Hellström, K. L. Jones, J. V. Kratz, R. Kulessa, C. Nociforo, R. Palit, H. Simon, G. Surówka, K. Sömmerer, D. Vretenar, and W. Waluś (LAND Collaboration), *Phys. Rev. C* **76** (2007) 051603(R). DOI: 10.1103/PhysRevC.76.051603.

[15] G.A. Bartholomew, *Annu. Rev. Nucl. Sci.* **11** (1961) 259. DOI: 10.1146/annurev.ns.11.120161.001355.

[16] J.S. Brzosko, E. Gierlik, A. Soltan, Z. Wilhelmi, *Can. J. Phys.* **47** (1969) 2849. DOI: 10.1139/p69-348.

[17] A.Ozawa, T. Suzuki, I.Tanihata, *Nucl. Phys. A* **693** (2001) 32. DOI: 10.1016/S0375-9474(01)01152-6.

[18] D. L. Canham, H.-W. Hammer, *Eur. Phys. J. A* **37** (2008) 367. DOI: 10.1140/epja/i2008-10632-4.

[19] N. Paar, D. Vretenar,P. Ring, *Phys. Rev. Lett.* **94** (2005) 182501. DOI: 10.1103/PhysRevLett.94.182501.

[20] R. Diehl, D. H. Hartmann, N. Prantzos, *Astrophysics with Radioactive Isotopes*, Astrophysics and Space Science Library (2018).

[21] H. K. Toft, A. C. Larsen, A. Bürger, M. Guttormsen, A. Görgen, H. T. Nyhus, T. Renstrøm, S. Siem, G. M. Tveten, A. Voinov, *Phys. Rev. C* **83** (2011) 044320. DOI: 10.1103/PhysRevC.83.044320.

[22] S. Nakayama, E. Matsumoto, R. Hayami, K. Fushimi, H. Kawasuso, K. Yasuda, T. Yamagata, H. Akimune, H. Ikemizu, M. Fujiwara, M. Yosoi, K. Nakanishi, K. Kawase, H. Hashimoto, T. Oota, K. Sagara, T. Kudoh, S. Asaji, T. Ishida, M. Tanaka, M. B. Greenfield, *Phys. Rev. C* **76** (2007) 021305(R). DOI: 10.1103/PhysRevC.76.021305.

[23] J.T. Caldwell, E.J. Dowdy, B.L. Berman, R.A. Alvarez, P. Meyer, *Phys.Rev. C* **21** (1980) 1215. DOI: 10.1103/PhysRevC.21.1215.

[24] A. Bohr, B. R. Mottelson, *Nuclear Structure*, Vol.1, WorldScientific, London (1998). ISBN-13: 978-9810231972

[25] D. Savran,T. Aumannc, A. Zilges, *Progress in Particle and Nuclear Physics* **70** (2013) 210. DOI: 10.1016/j.ppnp.2013.02.003.

[26] F. Reiche, W. Thomas, *Z. Phys.* **34** (1925) 331. DOI: 10.1007/BF01328494.

[27] W. Kuhn, *Z. Phys.* **33** (1925) 408. DOI: 10.1007/BF01328322.

[28] O. Wieland, A. Bracco, F. Camera *et al.*, *Phys. Rev. Lett.* **102** (2009) 092502. DOI: 10.1103/PhysRevLett.102.092502.

[29] R. Mohan, M. Danos, L.C. Biedenharn, *Phys. Rev. C* **3** (1971) 1740. DOI: 10.1103/PhysRevC.3.1740.

[30] H. Steinwedel and J. H. D. Jensen, *Z. Naturforsch.* **5** (1950) 413. DOI: 10.1515/zna-1950-0801.

[31] H. Steinwedel, M. Danos, *Phys. Rev.* **79** (1950) 1019. DOI: 10.1103/PhysRev.79.1019.2.

[32] M.A.Lone, E.D.Earle, G.A.Bartholomew, *Nuclear Physics A* **243** (1975) 413-439. DOI: 10.1016/0375-9474(75)90287-0.

[33] R.M. Laszewski, P. Axel, *Phys. Rev. C* **19** (1979) 342. DOI: 10.1103/PhysRevC.19.342.

[34] I. Tanihata, T. Kobayashi, O. Yamakawa, S. Shimoura, K. Ekuni, K. Sugimoto, N. Takahashi, T. Shimoda, H. Satol, *Phys. Lett. B* **160** (1985) 380. DOI: 10.1016/0370-2693(88)90702-2.

[35] T.Kobayashi, S.Shimoura, I. Tanihata, K. Katori, K. Matsuta, T. Minamisono, K. Sugimoto, W. Müller, D.L.Olson,T. J. M. Symons, H.,Wieman, *Phys. Lett. B* **232** (1989) 51. DOI: 10.1016/0370-2693(89)90557-1.

[36] V. Baran, B. Frecus, M. Colonna, M. Di Toro, *Phys. Rev. C* **85** (2012) 051601. DOI: 0.1103/PhysRevC.85.051601.

[37] T. Aumann, A. Leistenschneider, K. Boretzky, D. Cortinaa, J. Cub, W. Dostal, B. Eberlein, Th. W. Elze, H. Emling, H. Geissel, A. Grünschloß, M. Hellström, J. Holeczek, R. Holzmann, S. Ilievski, N. Iwasa, M. Kaspar, A. Kleinböhl, J. V. Kratz, R. Kulessa, Y. Leifels, E. Lubkiewicz, G. Münzenberg, P. Reiter, M. Rejmund, C. Scheidenberger, Ch. Schlegel, H. Simon, J. Stroth, K. Sümmerer, E. Wajda, W. Walus, S. Wana, *Nucl. Phys. A* **649** (1999) 297. DOI: 10.1016/S0375-9474(99)00075-5.

[38] A. Leistenschneider,T. Aumann, K. Boretzky *et al.*, *Phys. Rev. Lett.* **86** (2001) 5442. DOI: 10.1103/PhysRevLett.86.5442.

[39] N. Paar, P. Ring, T. Nikšic, D. Vretenar, *Phys. Rev. C* **67** (2003) 034312. DOI: 10.1103/PhysRevC.69.054303.

[40] E. Litvinova, P. Ring, V. Tselyaev, K. Langanke, *Phys. Rev. C* **79** (2009) 054312. DOI: 10.1103/PhysRevC.79.054312.

[41] G. A. Lalazissis, T. Nikšic, D. Vretenar, P. Ring, *Phys. Rev. C* **71** (2005) 024312. DOI: 10.1103/PhysRevC.71.024312.

[42] N. Paar, *J. Phys. G: Nucl. Part. Phys.* **37** (2010) 064014. DOI: 10.1088/0954-3899/37/6/064014.

[43] K. Govaert, F. Bauwens, J. Bryssinck, D. De Frenne, E. Jacobs, W. Mondelaers, L. Govor, and V. Yu. Ponomarev, *Phys. Rev. C* **57** (1998) 2229. DOI: 10.1103/PhysRevC.57.2229.

[44] P. Axel, K. K. Min, D. Sutton, *Phys. Rev. C* **2** (1970) 689. DOI: 10.1103/PhysRevC.2.689.

[45] P. Adrich, A. Klimkiewicz, M. Fallot, K. Boretzky, T. Aumann, D. Cortina-Gil, U. Datta Pramanik, Th. W. Elze, H. Emling, H. Geissel, M. Hellstrm, K. L. Jones, J. V. Kratz, R. Kulessa, Y. Leifels, C. Nociforo, R. Palit, H. Simon, G. Surwka, K. Smmerer, and W. Walu (LAND-FRS Collaboration), *Phys. Rev. Lett.* **95** (2005) 132501. DOI: 10.1103/PhysRevLett.95.132501.

[46] D. Savran, V. Derya, S. Bagchic, J. Endres, M. N. Harakeh, J. Isaak, N. Kalantar-Nayestanaki, E. G. Lanza, B.Löher, A. Najafi, S. Pascub, S. G. Pickstone, N. Pietralla, V. Yu. Ponomarev, C. Rigollet, C. Romig, M. Spieker, A. Vitturig, A.Zilgesb, *Phys. Lett. B* **786** (2018) 16. DOI: 10.1016/j.physletb.2018.09.025.

[47] G. Có, V. De Donno, C. Maieron, M. Anguiano, A. M. Lallena, *Phys. Rev. C* **80** (2009) 014308. DOI: 10.1103/PhysRevC.80.014308.

[48] C.J. Horowitz and J. Piekarewicz, *Phys. Rev. Lett.* **86** 5647 (2001). DOI: 10.1103/PhysRevLett.86.5647.

[49] S. Abrahamyan, Z. Ahmed,H. Albataineh *et al.*, *Phys. Rev. Lett.* **108** (2012) 112502. DOI: 10.1103/PhysRevLett.108.112502.

[50] J. Piekarewicz, *Phys. Rev. C* **73** (2006) 044325. DOI: 10.1103/PhysRevC.73.044325.

[51] P.-G. Reinhard, W. Nazarewicz, *Phys. Rev. C* **81** (2010) 051303(R). DOI: 10.1103/PhysRevC.81.051303.

[52] M. Thiel, C. Sfienti, J. Piekarewicz, C. J. Horowitz, M. Vanderhaeghen, *J. Phys. G: Nucl. Part. Phys.* **46** (2019) 093003. DOI: 10.1088/1361-6471/ab2c6d.

[53] V. Baran, M. Colonna, M. Di Toro, A. Croitoru,D. Dumitru, *Phys. Rev. C* **88** (2013) 044610. DOI: 10.1103/PhysRevC.88.044610.

[54] J. Piekarewicz, *Phys. Rev. C* **83** (2011) 034319. DOI: 10.1103/PhysRevC.83.034319.

[55] C. J. Horowitz, J. Piekarewicz, *Phys. Rev. C* **64** (2001) 062802. DOI: 10.1103/PhysRevC.64.062802.

[56] R. J. Furnstahl, *Nucl. Phys. A* **706** (2002) 85. DOI: 10.1016/S0375-9474(02)00867-9.

[57] W. Greiner, H.Stöcker, *The Nuclear Equation of State, Part A: Discovery of Nuclear Shock Waves and the EOS*, Vol. 216A, Nato Science Series B: Physics (1989).

[58] C. J. Horowitz and J. Piekarewicz, *Phys. Rev. C* **66** (2002) 055803. DOI: 10.1103/PhysRevC.66.055803.

[59] S. Goriely, *Phys. Lett. B* **436** (1998) 10. DOI: 10.1016/S0370-2693(98)00907-1.

[60] E. Litvinova, H.P. Loens, K. Langanke, G. Martinez-Pinedo, T. Rauscher, P. Ring, F.-K. Thielemann, V. Tselyaev, *Nuclear Phys.* **823** (2009) 26. DOI: 10.1016/j.nuclphysa.2009.03.009.

[61] A.Frebel, *Annu. Rev. Nucl. Part. Sci.* **68** (2018) 237. DOI: 10.1146/annurev-nucl-101917-021141.

[62] F. Giacoppo, F. L. Bello Garrote, T. K. Eriksen, A. Görgen, M. Guttormsen, T. W. Hagen, A. C. Larsen, B. V. Kheswa, M. Klintefjord, P. E. Koehler, H.T. Nyhus, T. Renstrøm, E. Sahin, S. Siem, T.G. Tornyi, *Phys. Rev. Lett.*, submitted Feb. 2014. arXiv:1402.2451[nucl-ex](2014).

[63] J.A. Holmes, S.E. Woosley, W.A. Fowler, B.A. Zimmerman, *At. Data Nucl. Data Tables* **18** (1976) 305. DOI: 10.1016/0092-640X(76)90011-5.

[64] A. Koning, S. Hilaire, M. Duijvestijn, TALYS: Nuclear Reaction Simulator. URL: https://tendl.web.psi.ch/tendl_2019/talys.html. Accessed: 2020-01-9.

[65] U. Agvaanluvsan, A. C. Larsen, M. Guttormsen, R. Chankova, G. E. Mitchell, A. Schiller, S. Siem, and A. Voinov, *Phys. Rev. C* **79** (2009) 014320. DOI: 10.1103/PhysRevC.79.014320.

[66] U. Agvaanluvsan, A. C. Larsen, R. Chankova, M. Guttormsen, G. E. Mitchell, A. Schiller, S. Siem, and A. Voinov, Phys. Rev. Lett. 102, 162504 (2009). DOI: 10.1103/PhysRevLett.102.162504.

[67] H. K. Toft, A. C. Larsen, U. Agvaanluvsan, A. Bürger, M. Guttormsen, G. E. Mitchell, H. T. Nyhus, A. Schiller, S. Siem, N. U. H. Syed, A. Voinov, *Phys. Rev. C* **81** (2010) 064311. DOI: 10.1103/PhysRevC.81.064311.

[68] P. Van Isacker, M. A. Nagarajan, D. D. Warner, *Phys. Rev. C* **45** (1992) R13. DOI: 10.1103/PhysRevC.45.R13.

[69] N. Tsoneva, H. Lenske, *Phys. Rev. C* **77** (2008) 024321. DOI: 10.1103/PhysRevC.77.024321.

[70] J. Endres, D. Savran, P. A. Butler, M. N. Harakeh, S. Harissopulos, R.-D. Herzberg, R. Krücken, A. Lagoyannis, E. Litvinova, N. Pietralla, V.Yu. Ponomarev, L. Popescu, P. Ring, M. Scheck, F. Schlter, K. Sonnabend, V. I. Stoica, H. J. Wrtche, and A. Zilges, *Phys. Rev. C* **85** (2012) 064331. DOI: 10.1103/PhysRevC.85.064331.

[71] J. Endres, D. Savran, A. M. van den Berg, P. Dendooven, M. Fritzsche, M. N. Harakeh, J. Hasper, H. J. Wörtche, A. Zilges, *Phys. Rev. C* **80** (2009) 034302. DOI: 10.1103/PhysRevC.84.024326.

[72] L.Pellegri, A.Bracco, F.C.L.Crespi *et al.*, *Phys. Lett. B* **738** (2014) 519. DOI: 10.1016/j.physletb.2014.08.029.

[73] S. Bassauer, Ph.D. Thesis *"Systematics of the Electric Dipole Response in Stable Tin Isotopes."*, Darmstadt, Technische Universitt, (2019).

[74] S. M. Grimes, *Journal of Nuclear Science and Technology* **39**:sup2 (2002) 709-713. DOI: 10.1080/00223131.2002.10875197.

[75] M. Guttormsen, M. Aiche, F. L. Bello Garrote, L. A. Bernstein, D. L. Bleuel, Y. Byun, Q. Ducasse, T. K. Eriksen, F. Giacoppo, A. Görgen, F. Gunsing, T. W. Hagen, B. Jurado2, M. Klintefjord, A. C. Larsen, L. Lebois, B. Leniau, H. T. Nyhus, T. Renstrøm, S. J. Rose, E. Sahin, S. Siem, T. G. Tornyi, G. M. Tveten, A. Voinov, M. Wiedeking, J. Wilson, *Eur. Phys. J. A* **51** (2015)170. DOI: 10.1140/epja/i2015-15170-4.

[76] H. A. Bethe, *Phys. Rev.* **50** (1936) 332. DOI: 10.1103/PhysRev.50.332.

[77] J. Bardeen, L.N. Cooper, J.R. Schrieffer, *Phys. Rev.* **108** (1957) 1175. DOI: 10.1103/PhysRev.108.1175.

[78] T.-D. Newton, *Can.J.Phys* **34** (1956) 804 .DOI: 10.1139/p56-090 .

[79] A. G. W. Cameron, *Can. J Phys.* **36** (1958) 1040. DOI: 10.1139/p58-112.

[80] E. Gadioli,L. Zetta, *Phys. Rev.* **167** (1968) 1016. DOI: 10.1103/PhysRev.167.1016.

[81] T. von Egidy, D. Bucurescu, *Phys. Rev. C* **72** (2005) 044311;**73** (2006) 049901(E). DOI: 10.1103/PhysRevC.72.044311.

[82] A. Gilbert, A. G. W. Cameron, *Can. J. Phys.* **43** (1965) 1446. DOI: 10.1139/p65-139.

[83] T. Ericson, *Nucl. Phys. A* **11** (1959) 481. DOI: 10.1016/0029-5582(59)90291-3.

[84] A. V. Ignatyuk, K. K. Istekov, G. N. Smirenkin, *Sov. J. Nucl. Phys.* **29**(4) (1979) 450.

[85] T. Belgya *et al.*, *Handbook for Calculations of Nuclear Reaction Data*, RIPL-2. IAEA-TECDOC-1506, IAEA, Vienna, (2006).

[86] P. Demetriou, S. Goriely, *Nucl. Phys. A* 695 (2001) 95. DOI: 10.1016/S0375-9474(01)01095-8.

[87] S. Hilaire, J.P. Delaroche, M. Girod, *Eur. Phys. J. A* 12 (2001) 169. DOI: 10.1007/s100500170025.

[88] S. Hilaire , S. Goriely, *Nuclear Physics A* 779 (2006) 63. DOI: 10.1016/j.nuclphysa.2006.08.014.

[89] Y. Alhassid, S. Liu, H. Nakada, *Phys. Rev. Lett.* 99 (2007) 162504. DOI: 10.1103/PhysRevLett.99.162504.

[90] National Nuclear Data Center web page. URL: https://www.nndc.bnl.gov/ensdf/. Accessed: 2020-02-27.

[91] R. Capote, M. Herman, P. Obložinsky, P. G. Young, S. Goriely, T. Belgya, A. V. Ignatyuk, A. J. Koning, S. Hilaire, V. A. Plujko, M. Avrigeanu, O. Bersillon, M. B. Chadwick, T. Fukahori, Zhigang Ge, Yinlu Han, S. Kailas, J. Kopecky, V. M. Maslov, G. Reffo, M. Sin, E. Sh Soukhovitskii, P. Talou, *Nuclear Data Sheets* **110**,2, (2009) 3107. Updated version, August 2015. DOI: 10.1016/j.nds.2009.10.004.

[92] D.R. Chakrabarty, V.M. Datas, S. Kuman, E.T. Migule, H.H. Oza and U.K. Pal, *Phys. Rev. C* **51** (1995) 2942. DOI: 10.1103/PhysRevC.51.2942.

[93] Y. Kalmykov, C. Özen, K. Langanke, G. Martnez-Pinedo, P. von Neumann-Cosel, A. Richter, *Phys. Rev. Lett.* **99** (2007) 202502. DOI: 10.1103/PhysRevLett.99.202502.

[94] B. J. Allen, I. Bergqvist, R. E. Chrien, *Neutron Radiative Capture: Neutron Physics and Nuclear Data in Science and Technology*, Pergamon Press, Great Britain, Wiltshire, (1984). ISBN-13: 978-1483120010.

[95] J.M. Blatt and V.F. Weisskopf, *Theoretical Nuclear Physics*, Wiley, New York, (1952). DOI: 10.1007/978-1-4612-9959-2.

[96] G. A. Bartholomew, E. D. Earle, A. J. Ferguson, J. W. Knowles, M. A. Lone, *Gamma-Ray Strength Functions*, Springer US, Boston (1973). DOI: 10.1007/978-1-4615-9044-6_4. URL http://dx.doi.org/10.1007/978-1-4615-9044-6_4.

[97] W. Hauser, H. Feshbach, *Phys. Rev.* **87** (1952) 366. DOI: 10.1103/PhysRev.87.366.

[98] S.G. Kadmenskij, V.P. Markushev, V.I. Furman, *Yad. Fiz.* **37** (1938) 277; *Sov. J. Nucl. Phys.* **37** (1983) 165.

[99] J. Kopecky, R. E. Chrien, *Nucl. Phys. A* **468** (1987) 285. DOI: 10.1016/0375-9474(87)90518-5.

[100] J.Kopecky, M. Uhl, *Phys Rev. C* **41** (1990) 1941. DOI: 10.1103/PhysRevC.41.1941.

[101] V. M. Kolomietz, V. A. Plujko, S. Shlomo, *Phys. Rev. C* **54** (1996) 3014. DOI: 10.1103/PhysRevC.54.3014.

[102] V.A.Plujko, *Acta Phys. Pol. B* **31** (2000) 435. DOI: 10.1016/S0375-9474(99)00063-9.

[103] S.F.Mughaghab, C.L.Dunford, *Phys. Lett. B* **487** (2000) 155. DOI: 10.1016/S0370-2693(00)00792-9.

[104] S. Goriely, E. Khan, *Nucl. Phys. A* **706** (2002) 217. DOI: 10.1016/S0375-9474(02)00860-6

[105] S. Goriely, S. Hilaire, M. Girod, S. Péru , *Phys. Rev. Lett.* **102** (2009) 242501. DOI: 10.1103/PhysRevLett.102.242501.

[106] M. Zaman, G. Kim, H. Naik, K. Kim, *Journal of Radioanalytical and Nuclear Chemistry* **299** (2014) 1739. DOI: 10.1007/s10967-013-2914-z.

[107] S. S.Dietrich, B. L.Berman, *Atomic Data and Nuclear Data Tables* **38**,2, (1988) 199. DOI: 10.1016/0092-640X(88)90033-2.

[108] H. Utsunomiya, H. Akimune, S. Goko, M. Ohta, H. Ueda, T. Yamagata, K. Yamasaki, H. Ohgaki, H. Toyokawa, Y.-W. Lui, T. Hayakawa, T. Shizuma, E. Khan, and S. Goriely, *Phys. Rev. C* **67** (2003) 015807. DOI: 10.1103/PhysRevC.67.015807.

[109] U. Kneissl, H. H. Pitz, A. Zilges, *Progress in Particle and Nuclear Physics* **37** (1996) 349. DOI: 10.1016/0146-6410(96)00055-5.

[110] W.V. Prestwich, M.A. Islam,T.J. Kennett, *Z. Phys.* **315** (1984) 103. DOI: 10.1007/BF01436215.

[111] A. Voinov, S. M. Grimes, C. R. Brune, M. Guttormsen, A. C. Larsen, T. N. Massey, A. Schiller, S. Siem, *Phys. Rev. C* **81** (2010) 024319. DOI: 10.1103/PhysRevC.81.024319.

[112] D. M. Brink, Ph.D. Thesis, *"Some Aspects of the Interaction of Fields with Matter"*, Oxford University (1955).

[113] P.F. Bortignon, A. Bracco, R.A. Broglia, *Giant Resonances: Nuclear Structure at Finite Temperature*, Harwood Academic, Amsterdam (1998). ISSN 0272-2488.

[114] P. Axel, *Phys. Rev.* **126** (1962) 671. DOI: 10.1103/PhysRev.126.671.

[115] M. Guttormsen, A.C. Larsen, A. Görgen, T. Renstrøm, S. Siem, T.G. Tornyi, G.M. Tveten, *Phys. Rev. Lett.* **116** (2016) 012502. DOI: 10.1103/PhysRevLett.116.012502.

[116] M. Guttormsen, A. C. Larsen, A. Görgen, T. Renstrøm, S. Siem, T. G. Tornyi, G. M. Tveten, *Proceedings of Science* (2016)1-8. URL: arXiv:1701.07317v1 [nucl-ex] 25 Jan 2017

[117] L. Crespo Campo, M. Guttormsen, F. L. Bello Garrote, T. K. Eriksen, F. Giacoppo, A. Görgen, K. Hadynska-Klek, M. Klintefjord, A. C. Larsen, T. Renstrøm, E. Sahin, S. Siem, A. Springer, T. G. Tornyi, and G. M. Tveten, *Phys. Rev. C* **98** (2018) 054303. DOI: 10.1103/PhysRevC.98.054303.

[118] C. E. Porter, R. G. Thomas, *Phys. Rev.* **104** (1956) 483. DOI: 10.1103/PhysRev.104.483.

[119] J. Isaak, D. Savran, B. Loeher, T. Beck, M. Bhike, U. Gayer, Krishichayan, N. Pietralla, M. Scheck, W. Tornow, V. Werner, A. Zilges, M. Zweidinger, *Phys. Lett. B* **788** (2019) 225. DOI: 10.1016/j.physletb.2018.11.038.

[120] The homepage of the Oslo Cyclotron Laboratory (OCL).URL: https://www.mn.uio.no/fysikk/english/research/about/infrastructure/ocl/. Accessed: 2019-06-17.

[121] M. Guttormsen, A.Bürger, T.E.Hansen, N. Lietaer, *Nuclear Instruments and Methods in Physics Research A* **648** (2011) 168. DOI: 10.1016/j.nima.2011.05.055.

[122] W. R. Leo, *Techniques for Nuclear and Particle Physics Experiments*, Springer-Verlag (1994). ISBN 3540572805.

[123] H. Bethe, *Z. Phys.* **76** (1932) 293. DOI: 10.1007/BF01342532.

[124] F. Bloch, *Ann. Phys.* **16** (1933) 285. DOI: 10.1002/andp.19334080303.

[125] A. Giaz, L. Pellegri, S. Riboldi, F. Camera, N. Blasi, C. Boiano, A. Bracco, S. Brambilla, S. Ceruti, S. Coelli, F. C L Crespi, M. Csatlós, S. Frega, J. Gulys, A. Krasznahorkay, S. Lodetti, B. Million, A. Owens, F. Quarati, L. Stuhl, O. Wieland, *Nuclear Instruments and Methods in Physics Research A* **729** (2013) 910. DOI: 10.1016/j.nima.2013.07.084

[126] The AMITEK ORTEC home page.URL:https://www.ortec-online.com/products/radiation-detectors/scintillation-detectors/scintillation-detector-types/lanthanum-bromide-detectors. Accessed: 2019-07-01.

[127] L. Crespo Campo, F. L. Bello Garrote, T. K. Eriksen, A. Görgen, M. Guttormsen, K. Hadynska-Klek, M. Klintefjord, A. C. Larsen, T. Renstrøm, E. Sahin, S. Siem, A. Springer, T. G. Tornyi, and G. M. Tveten, *Phys. Rev. C* **94** (2016) 044321. DOI: 10.1103/PhysRevC.94.044321

[128] XIA, Pixie-16 User Manual, Version 3.06, 2019. URL: https://www.xia.com/dgf_pixie-16.html . Acessed: 2019-09-12.

[129] K. S. Krane, *Introductory Nuclear Physics*, John Wiley and Sons (1998). ISBN-13: 978-0471805533.

[130] V.W. Ingeberg, F. Zeiser, E. Lima,Qkinz kinematics calculator: oslocyclotronlab/Qkinz. DOI: 10.5281/ZENODO.1206099.

[131] R. Pani, M. N. Cinti, R. Pellegrini, P. Bennati, S. Ridolfi, R.Scafé, V. Orsolini Cencelli, F. De Notaristefani, A. Fabbri, F. L. Navarria, N. Lanconelli, G. Moschini, P. Boccaccio, *Nucl. Phys. B* (Proc. Suppl.) **215** (2011) 168172. DOI: 10.1016/j.nuclphysbps.2011.03.167.

[132] A. V'értes, S. Nagy, Z. Klencsár, R. G. Lovas, F.Rösch, *Handbook of Nuclear Chemistry*, Springer Science Business Media B.V. (2011). ISBN: 978-1-4419-0720-2

[133] The Geant4 home page: URL: https://geant4.web.cern.ch/. Acessed: 2019-20-10.

[134] The Oslo method software package. URL: https://zenodo.org/record/1153992#.XgeBZ5MzY_U. Acessed: 2019-17-11.

[135] M. Guttormsen, T.S. Tveter, L. Bergholt, F. Ingebretsen, J. B. Rekstad, *Nucl. Instr. and Meth. in Phys. Res. A* **374** (1996) 371. DOI: 10.1016/0168-9002(96)00197-0.

[136] Cs. Siükösd, B. Galster, I. Licot, M.P. Simonart, *Nucl.Instr. and Meth. A* **355** (1995) 552. DOI: 10.1016/0168-9002(94)01122-2.

[137] M. Guttormsen, L. A. Bernstein, A. Görgen, B. Jurado, S. Siem, M. Aiche, Q. Ducasse, F. Giacoppo, F. Gunsing, T. W. Hagen, A. C. Larsen, M. Lebois, B. Leniau, T. Renstrøm, S. J. Rose, T. G. Tornyi, G. M. Tveten, M. Wiedeking, J. N. Wilson, *Phys. Rev. C* **89** (2014) 014302. DOI: 10.1103/PhysRevC.89.014302.

[138] M.Guttormsen,T.Ramsöy, J.Rekstad, *Nucl. Instrum. Methods Phys. Res. A* **255** (1987) 518. DOI: 10.1016/0168-9002(87)91221-6.

[139] A. C. Larsen, M. Guttormsen, M. Krtička, E. Bětak, A. Brger, A. Görgen, H. T. Nyhus, J. Rekstad, A. Schiller, S. Siem, H. K. Toft, G. M. Tveten, A. V. Voinov, K. Wikan, *Phys. Rev. C* **83** (2011) 034315. DOI: 10.1103/PhysRevC.83.034315.

[140] J. Rekstad, A. Henriquez, F. Ingebretsen, G. Midttun, B. Skaali, R. Øyan, J. Wikne, T. Engeland, T. F. Thorsteinsen, E. Hammaren, E. Liukkonen, *Phys. Scr. T* **5** (1983) 45. DOI: 10.1088/0031-8949/1983/T5/007.

[141] P. A. M. Dirac, *Proc. R. Soc. London A* **114** (1927) 243. DOI: 10.1098/rspa.1927.0039.

[142] E. Fermi, *Nuclear Physics*, University of Chicago Press (1950). ISBN-13: 978-0226243658

[143] M. Guttormsen, A. C. Larsen, A. Bürger, A. Görgen, S. Harissopulos, M. Kmiecik, T. Konstantinopoulos, M. Krtička, A. Lagoyannis, T. Lnnroth, K. Mazurek, M. Norrby, H. T. Nyhus, G. Perdikakis, A. Schiller, S. Siem, A. Spyrou, N. U. H. Syed, H. K. Toft, G. M. Tveten, A. Voinov, *Phys. Rew. C* **83** (2011) 014312. DOI: 10.1103/PhysRevC.83.014312.

[144] L.,Henden, L. Bergholt, M. Guttormsen, J. Rekstad, T. S. Tveter, *Nucl. Phys. A* **589** (1995) 249. DOI: 10.1016/0375-9474(95)00133-L.

[145] A. Schiller, L. Bergholt, M. Guttormsen, E. Melby, J. Rekstad, S. Siem, *Nucl. Instrum. Methods Phys. Res. A* **447** (2000) 498. DOI: 10.1016/S0168-9002(99)01187-0.

[146] N. U. H. Syed, M. Guttormsen, F. Ingebretsen, A. C. Larsen, T. Lnnroth, J. Rekstad, A. Schiller, S. Siem, A. Voinov, *Phys. Rev. C* **79** (2009) 024316. DOI: 10.1103/PhysRevC.79.024316.

[147] T. Ericson, V. Strutinski, *Nuclear Physics* **8** (1958) 284. DOI: 10.1016/0029-5582(58)90156-1.

[148] L. G. Moretto, A. C. Larsen, F. Giacoppo, S. Siem, *J. Phys. Conf. Ser.* **580** (2015) 012048. DOI: 10.1088/1742-6596/580/1/012048.

[149] T. von Egidy, D. Bucurescu, *Phys. Rev. C* **80** (2009) 054310. DOI: 10.1103/PhysRevC.80.054310.

[150] A. Voinov, M. Guttormsen, E. Melby, J. Rekstad, A. Schiller, S. Siem, *Phys. Rev. C* **63** (2001) 044313. DOI: 10.1103/PhysRevC.63.044313.

[151] S.F. Mughabghab, *Atlas of Neutron Resonances, Volume 1: Resonance Properties and Thermal Cross Sections Z= 1-60*, Elsevier Science (2018). ISBN-13: 978-0444637697

[152] Dobaczewski, P. Magierski, W. Nazarewicz, W. Satula, and Z. Szymanski, *Phys. Rev. C* **63** (2001) 024308. DOI: 10.1103/PhysRevC.63.024308.

[153] A. C. Larsen, M. Guttormsen, R. Schwengner, D. L. Bleuel, S. Goriely, S. Harissopulos, F. L. Bello Garrote, Y. Byun, T. K. Eriksen, F. Giacoppo, A. Görgen, T. W. Hagen, M. Klintefjord, T. Renstrøm, S. J. Rose, E. Sahin, S. Siem, T. G. Tornyi, G. M. Tveten, A. V. Voinov, M. Wiedeking, *Phys. Rev. C* **93** (2016) 045810. DOI: 0.1103/PhysRevC.93.045810.

[154] H. Utsunomiya, S. Goriely, M. Kamata, H. Akimune, T. Kondo, O. Itoh, C. Iwamoto, T. Yamagata, H. Toyokawa, Y.-W. Lui, H. Harada, F. Kitatani, S. Goko, S. Hilaire, A. J. Koning, *Phys. Rev. C* **84** (2011) 055805. DOI: 10.1103/PhysRevC.84.055805.

[155] V. V. Varlamov, B. S. Ishkhanov, V. N. Orlin, V. A. Chetvertkova, *Bull. Rus. Acad. Sci.* **74** (2010) 833. DOI: 10.3103/S1062873810060225

[156] S. C. Fultz, B. L. Berman, J. T. Caldwell, R. L. Bramblett, M. A. Kelly, *Phys. Rev.* **186** (1969) 1255. DOI: 10.1103/PhysRev.186.1255.

[157] A. Leprêtre, H. Beil, R. Bergere, P. Carlos, A. D. Miniac, A. Veyssire, K. Kernbach, *Nucl. Phys. A* **219** (1974) 39. DOI: 10.1016/0375-9474(76)90011-7.

[158] B.L. Berman, S.C. Fultz, *Rev. Mod. Phys.* **47** (1975) 713. DOI: 10.1103/RevModPhys.47.713.

[159] T. von Egidy, H. H. Schmidt, A. N. Behkami, *Nucl. Phys. A* **481** (1988) 189. DOI: 10.1016/0375-9474(88)90491-5.

[160] S. F. Mughabghab, *Atlas of Neutron Resonances*, 5th ed. Elsevier Science, New York, (2006). ISBN: 9780080461069

[161] A. Schiller, E. Algin, L. A. Bernstein, P. E. Garrett, M. Guttormsen, M. Hjorth-Jensen, C. W. Johnson, G. E. Mitchell, J. Rekstad, S. Siem, A. Voinov, W. Younes, *Phys. Rev. C* **68** (2003) 054326. DOI: 10.1103/PhysRevC.68.054326.

[162] R. Schwengner, S. Frauendorf, A. C. Larsen, *Phys. Rev. Lett.* **111** (2013) 232504. DOI: 10.1103/PhysRevLett.111.232504.

[163] E. Litvinova N. Belov, *Phys. Rev. C* **88** (2013) 031302(R). DOI: 10.1103/PhysRevC.88.031302.

[164] M. D. Jones, A. O. Macchiavelli, M. Wiedeking et al.// *Phys. Rev. C* **97** (2018) 024327. DOI: 10.1103/PhysRevC.97.024327.

[165] M. Wiedeking, L. A. Bernstein, M. Krtička, D. L. Bleuel, J. M. Allmond, M. S. Basunia, J. T. Burke, P. Fallon, R. B. Firestone, B. L. Goldblum, R. Hatarik, P. T. Lake, I-Y. Lee, S. R. Lesher, S. Paschalis, M. Petri, L. Phair, and N. D. Scielzo, *Phys. Rev. Lett.* **108** (2012) 162503. DOI: 10.1103/PhysRevLett.108.162503.